Análise de métodos de volumes finitos miméticos para modelos de águas rasas clássicos e com umidade considerando malhas esféricas de Voronoi com refinamento local baseado em topografia

Analysis of mimetic finite volume schemes on classical and moist shallow water models considering topography based local refinement in spherical Voronoi grids

Luan da Fonseca Santos

Dissertação apresentada
ao
Instituto de Matemática e Estatística
da
Universidade de São Paulo
para
obtenção do título
de
Mestre em Ciências

Programa: Matemática Aplicada

Orientador: Prof. Dr. Pedro da Silva Peixoto

São Paulo, Março de 2020

Análise de métodos de volumes finitos miméticos para modelos de águas rasas clássicos e com umidade considerando malhas esféricas de Voronoi com refinamento local baseado em topografia

Esta é a versão original da dissertação elaborada pelo candidato Luan da Fonseca Santos, tal como submetida à Comissão Julgadora.

Comissão Julgadora:

- Prof. Dr. Saulo Rabello Maciel de Barros (Presidente) - IME-USP
- Prof. Dr. Pedro Leite da Silva Dias - IAG-USP
- Prof. Dr. Silvio Nilo Figueroa Rivero - CPTEC-INPE

Agradecimentos

Abstract

Santos, L. F. **Analysis of mimetic finite volume schemes on classical and moist shallow water models considering topography based local refinement in spherical Voronoi grids**. 2020. 74 f. Dissertation (Masters) - Instituto de Matemática e Estatística, Universidade de São Paulo, São Paulo, 2020.

The latitude-longitude grid has been used in global atmospheric models since the early 1960s until today. Nevertheless, the use of this grid creates drawbacks for scalability on massively parallel machines, mainly due to excessive data communication requirements near the poles. Thus, to achieve the required degree of parallelism for the efficient use of massively parallel architectures, the interest in quasi-uniform geodesic grids has increased. Much consideration has been given to icosahedral grids and its pentagonal/hexagonal dual grid. This grid might be optimized using centroidal Voronoi tesselation algorithms that allows us to build local refinements based on a density function. Grids with local refinements have been developed aiming to solve local phenomena without requiring the use of a uniform global grid which can be computationally prohibitive.

In this work, aiming to benefit weather forecasting in Brazil, we propose a grid that captures well the Andes mountains and the South American continent. This grid is built through a density function based on topography using centroidal Voronoi tesselation algorithms. The developed density function uses smoothing data techniques on the topography data and has a parameter that allows us to approximately define the ratio between the cell diameters in low and high-resolution regions. The grids developed have a smooth transition between low and high-resolution regions. Using the grids developed, we analyze the use of a mimetic finite volume method for the shallow water equations. Using standard, and more recent shallow water tests available in the literature, our results show that the refined region generates localized numerical noise in the solution. However, we show how a small amount of diffusion is already enough to mitigate this problem. Additionally, we also implemented a moist shallow water model, where physical precipitation processes are included in the classical shallow water model. This model is used to investigate the impact of the local refinement on the cloud and rain formation in the South American continent, with results indicating that the refinement greatly affects the model, generating more cloud and rain when compared to the uniform resolution model.

Keywords: geodesic grids, non structured grids, local refinement, finite volume, shallow water equations, moist shallow water model

iv

Resumo

Santos, L. F. **Análise de métodos de volumes finitos miméticos para modelos de águas rasas clássicos e com umidade considerando malhas esféricas de Voronoi com refinamento local baseado em topografia**. 2020. 74 f. Dissertação (Mestrado) - Instituto de Matemática e Estatística, Universidade de São Paulo, São Paulo, 2020.

Malhas do tipo latitude longitude são usadas em modelos atmosféricos globais desde o início dos anos 60. Porém, estas malhas apresentam problemas de escalabilidade em máquinas massivamente paralelas devido ao excesso de comunicação de dados dos pontos que se acumulam nos polos. Assim o interesse em malhas geodésicas quase uniformes tem aumentado visando atingir o grau de paralelismo necessário para o uso eficiente de máquinas paralelas. A malha icosaédrica e a sua malha dual pentagonal/hexagonal tem se destacado. Esta malha pode ser otimizada usando algoritmos de Diagramas centroidais de Voronoi que permitem construir refinamentos locais através de uma função de densidade. Malhas com refinamento local são desenvolvidas visando resolver fenômenos locais sem utilizar uma malha uniforme global que pode ser computacionalmente proibitiva.

Neste trabalho, visando beneficiar a previsão do tempo no Brasil, propomos desenvolver malhas que capturam bem a cordilheira dos Andes e o continente sul-americano. Esta malha é construída através de uma função de densidade que é baseada na topografia terrestre usando algoritmos de Diagramas centroidais de Voronoi. A função de densidade desenvolvida usa técnicas de suavização de dados e tem um parâmetro que permite definir a razão dos diâmetros entre células da região refinada e da região de malha grossa. A malha desenvolvida tem uma transição suave entre a região de malha fina e malha grossa. Utilizando as malhas desenvolvidas, nós analisamos um método de volumes finitos mimético para as equações de água rasa. Usando testes clássicos e mais recentes para o modelo de água rasa propostos na literatura, nossos resultados mostram que a região refinada gera ruído numérico local na solução. No entanto, mostramos que uma pequena quantidade de difusão é suficiente para resolver esse problema. Além disso, também implementamos um modelo de água rasa com umidade, onde os processos de precipitação física são incluídos no modelo clássico de água rasa. Este modelo é usado para analisarmos o impacto do refinamento local na formação de nuvens e chuvas no continente sul-americano, com resultados indicando que o refinamento afeta bastante o modelo, gerando mais nuvens e chuva quando comparado ao modelo de resolução uniforme.

Palavras-chave: malhas geodésicas, malhas não-estruturadas, refinamento local, volumes finitos, equações de água rasa, umidade.

Contents

Chapter 1

Introduction

1.1 Background

Weather prediction and climate simulation require the solution of partial differential equations that are defined on the sphere. These equations are the so-called primitive equations and represent mathematically the geophysical fluid dynamics and are derived from physical laws for state variables such as wind velocity, temperature and pressure (Haltiner e Williams, 1980; Holton, 2004). These problems are initial value problems, i.e., knowing these equations and given the initial state, our task is to find the time evolution of the state variables. However, these equations are too complex to be solved analytically and must be treated numerically. This motivates the construction of global atmospheric models.

A global atmospheric model consists of a dynamical core and physical parametrizations. The dynamical core solves the fluid motion equations, thermodynamics equations and also solves the transport of tracers that are resolved on grid-scale. On the other hand, sub-grid scale processes such as radiative processes and convective processes are represented in physical parametrizations, where these sub-grid processes are parameterized as functions of the grid-scale processes (Williamson, 2007).

In order to develop a global atmospheric model, it is helpful to start with a simpler model that is capable to retain important aspects of the complete system. The three-dimensional Euler equations can be simplified to the shallow water equations on the sphere. They describe the dynamics of a thin layer, rotating two-dimensional fluid. They are a stepping stone to design numerical schemes for the full three-dimensional weather prediction and climate models. The shallow water equations have the advantage of being two dimensional, therefore they reduce the computational cost to run in high resolutions. Furthermore, besides being an interesting geophysical model on their own, the shallow water equations represent key properties of the atmosphere, such as geostrophic adjustment, Coriolis effect, gravity waves and Rossby waves.

One important choice in order to develop a numerical method for an atmospheric model is to define a grid that covers the sphere. There are several ways to do this. One alternative is the regular latitude-longitude grid which perhaps is the most natural way do discretize the sphere. This grid has a nice rectangular structure and orthogonality properties. Atmospheric models used finite differences schemes on these grids in the early 1960s. However, the convergence of meridians at the poles makes the longitude intervals distance goes to zero. This causes the so-called "pole problem", where explicit finite difference and finite volume schemes must have a too short time step to satisfy the Courant-Fredrich-Levy (CFL) condition, which makes these schemes too expensive. Some attempts made finite difference schemes on a latitude-longitude grid cheaper such as applying filters near the poles (Williamson, 2007).

In the 1970s the spectral method, which uses a latitude-longitude grid, became the most popular and almost exclusive choice for atmospheric models until the emergence of massively parallel computing platforms. During this time, semi-Lagrangian schemes were also developed and have been adopted by some weather prediction centers. These semi-Lagrangian schemes allow longer time

steps and also use a latitude-longitude grid. Efforts were made to improve the physical properties of spectral and semi-Lagrangian schemes since the numerical solution should reflect the physical properties of the continuous equations. Although semi-Lagrangian schemes and spectral methods solve the pole problem mentioned before, they suffer from scalability bottleneck on massively parallel architectures due to global data communication as a result of spectral transform and also because of the grid points clustered in the poles (Staniforth e Thuburn, 2012). For these reasons, many development efforts have been made to investigate isotropic alternatives grids to the traditional latitude-longitude grid that allow good scaling efficiency on massively parallel machines.

Grids based on Platonic solids became popular and have been adopted in modern global atmospheric models. These grids are more homogeneous, isotropic and have desirable properties for atmospheric modelling on the sphere. An example of such grids is the cubed sphere, which is a geodesic grid obtained through a gnomonical projection of the cube edges onto the sphere. The resulting spherical squares are uniformly subdivided into new spherical squares, yielding a high-resolution grid.

Another popular grid-based on Platonic solid is the icosahedral grid and its pentagonal-hexagonal dual grid. The construction of the icosahedral grid starts with the icosahedron inscribed within a sphere that is gnomonically projected the sphere. This process results in a grid that is composed of 20 spherical triangles and 12 grid points. Each resulting spherical triangle is divide into 4 new spherical triangles, and we proceed in this manner until we reach the desired resolution. This process yields a Delaunay Triangulation on the sphere. Its dual grid can be obtained by taking the Voronoi Diagram of the icosahedral grid (Ju *et al.*, 2011).

It is usual to optimize the icosahedral grid by some grid optimization algorithm aiming to improve discrete operators' accuracy. In (Miura e Kimoto, 2005), the authors analyze grid quality properties and the converge of finite volume operators in optimized icosahedral grids using the optimization proposed by (Heikes e Randall, 1995), the spring dynamics optimization (Tomita *et al.*, 2002) and spherical centroidal Voronoi (SCVT) optimization (Du *et al.*, 1999; Ju *et al.*, 2011). These optimizations are needed to improve the operators' convergence.

Much consideration has been given on icosahedral grids for the next generation of global atmospheric models. In fact, the icosahedral grid has been used in global atmospheric models. For instance, the NICAM (nonhydrostatic icosahedral atmospheric model) (Satoh *et al.*, 2008) uses an icosahedral grid optimized with spring dynamics. The DYNAMICO (Dubos *et al.*, 2015) uses the dual grid optimized with SCVT optimization. The ICON-IAP (Icosahedral Nonhydrostatic model at the Institute for Atmospheric Physics), developed by Max Planck Institute for Meteorology (MPI-M) and Deutscher Wetterdienst (DWD), uses the dual grid with the spring dynamics optimization (Gassmann, 2013).

The centroidal Voronoi grids are also used in MPAS (Model for Prediction Across Scales), which is jointly developed by NCAR and Los Alamos Laboratory (Skamarock *et al.*, 2012). This model is designed for weather and climate modeling, regional climate, oceanographic modeling and seems to achieve good scalability on parallel computing machines. Besides that, MPAS explores grids with local refinement aiming to solve phenomena such as clouds in specific regions of the earth. Voronoi grids have the advantage of allowing local refinement. This can be done using Lloyds's method (Ju *et al.*, 2011). Using locally refined grids in a global model avoids artificial boundary conditions, as it is usual in regional atmospheric models. Global models with locally refined grids have been developed for other grids like the latitude-longitude grid. In Barros e Garcia (2004), they develop a semi-implicit semi-Lagrangian global shallow water model in a latitude-longitude grid with local refinement and smooth transitions to coarser regions. It is worth pointing out that being unstructured makes Voronoi grids able to have a much more flexible refinement than in structured grids like the latitude-longitude grid.

The MPAS model discretizes spatially the continuous equations using finite volume techniques on the centroidal Voronoi grid. The prognostic variables are distributed according to a C-staggering distribution. Their discretization is based on Thuburn *et al.* (2009) and Ringler *et al.* (2010). This method is known in the literature as TRSK and it is designed to solve the shallow water equations on

the sphere for a variety of grids. TRSK was first developed for the linear shallow water equations in Thuburn *et al.* (2009) on arbitrary structured C-grids that have an orthogonal dual grid. In Ringler *et al.* (2010), TRSK was extended to the non-linear shallow water equation for same type of grid as in Thuburn *et al.* (2009). Later, it was extended for grids with non-orthogonal dual (Thuburn e Cotter, 2012; Weller, 2014). The TRSK methodology became popular since it uses local operators and reflects many physical constraints that the continuous equations have. These properties are known as mimetic properties and are highly desirable for global atmospheric models.

1.2   Motivations and goals

In this work, we aim to study the TRSK scheme to solve the shallow water equations on centroidal Voronoi grids with local refinement based on topography. We shall apply Lloyd's method (Ju *et al.*, 2011) to build grids that capture well the Andean mountain and are smoothly transitioned to a regional grid in South America that is also smoothly transitioned to a coarser global grid. Thus, we are interested in developing grids with higher resolution on Andes mountain in order to allow studies about the effect of Andes on the weather and climate conditions over South America. For instance, in Walsh (1994) the author investigates the effect of Andes topography on the circulation of the Southern Hemisphere climate using a spectral global circulation model and concludes that the Andes has a dramatic impact only in South America climate. In Seluchi *et al.* (1998), the effect of the Andes in high and low-pressure systems is analyzed also using a global circulation model. Therefore, we believe that this kind of grid can benefit South America climate studies and weather forecasting.

We evaluate the behavior of TRSK on the grid with local refinement on the Andes applying standard shallow water test cases proposed in the literature (Galewsky *et al.*, 2004; Williamson *et al.*, 1992) and also the test case recently proposed by Shamir *et al.* (2019).

Although the shallow water equations represent many of dynamics of the full equations, they lack physics forcing that play a key role in the atmosphere. Global models usually include physical parametrization after the three-dimensional dynamical core is completely developed. In order to avoid a rework of numerical schemes when applied to a three-dimensional model, it is desirable to be able to evaluate a numerical scheme adding physical forces in the shallow water model before investing effort to develop a complete three-dimensional model. Therefore, we propose to investigate the convective moisture shallow water model proposed by Zerroukat e Allen (2015), discretize this model using TRSK and test it on locally refined grids.

We will the grid generator and shallow water model developed by Peixoto (2013) called iModel. We developed in iModel the capabilities of topography based local refinement, convective shallow water model and the test case proposed by Shamir *et al.* (2019).

1.3   Outline

In Chapter 2 introduce the concepts of spherical centroidal Voronoi tesselations and how this is an useful tool to build grids with local refinement based on topography. In Chapter 3 we present the shallow water equations and its vector invariant form. Then, we discretize the shallow water equations using TRSK.

In Chapter 4 we show results of standard shallow water tests proposed in the literature using TRSK in grids with local refinements based on topography. We also present in Chapter 5 a convective shallow water model and show how we can discretizate the equations using TRSK. Results for SCVT with local refinement are presented. At last, we show the conclusions of our analysis in Chapter 6.

Chapter 2

SCVT grids

This chapter aims to explain the sphere discretization adopted in this wok. We will introduce the icosahedral grid in Section 2.1 and SCVT optimization in Section 2.2. In Section 2.3 we shall see some examples of locally refined grid and also a way to build a grid with local refinement on the Andes mountain region by setting an appropriate density function based on topography and using Lloyd's method (Ju *et al.*, 2011).

2.1 Definitions

We start with basic definitions of Voronoi diagrams and Delaunay triangulations. Although those concepts can be defined for any d dimensional space or manifold, we will focus only on the case of the unit sphere $\mathcal{S}^2$.

Definition 2.1. (Voronoi Diagram) Let $\{x_i\}_{i=1}^n \subset \mathcal{S}^2$ a set of points on the sphere. The i-th Voronoi region Ω_i is defined by:

$$\Omega_i = \{x \in \mathcal{S}^2 : d(x_i, x) < d(x_j, x), \forall i \neq j\},$$

where $d(\cdot, \cdot)$ denotes the geodesic distance on the sphere:

$$d(x, y) = \arccos(x \cdot y), \forall x, y \in \mathcal{S}^2.$$

The sets $\{\Omega_i\}_{i=1}^n$ is called a Voronoi tesselation or a Voronoi diagram of the sphere and the points $\{x_i\}_{i=1}^n$ are called generators. From Definition 2.1 follows the properties:

- $\Omega_i \cap \Omega_j = \emptyset$ for all $i \neq j$;

- $\bigcup_{i=1}^n \overline{\Omega_i} = \mathcal{S}^2$, where $\overline{\Omega_i}$ denotes the closure of Ω_i;

- Each Ω_i is an open convex spherical polygonal.

Another important concept is the definition of Delaunay triangulation.

Definition 2.2. (Triangulation) Let $P = \{x_i\}_{i=1}^n \subset \mathcal{S}^2$ and $\Delta = \{T_1, \cdots, T_k\}$ a set of spherical triangles. We say that Δ is a triangulation of the sphere if:

- $\bigcup_{i=1}^k T_i = \mathcal{S}^2$;

- The triangles have disjoint interiors;

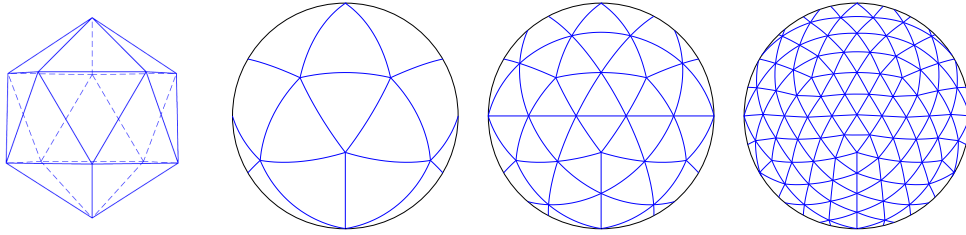- Each triangle contains only its own vertices;

- The set of all vertices is P.

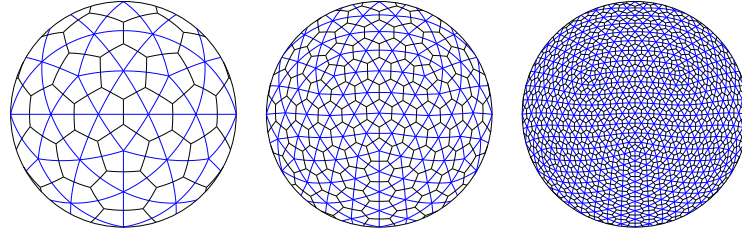**Figure 2.1:** *Icosahedral grid construction - 20, 42, 162 and 642 vertices.*

Figure 2.2: *Voronoi diagrams and the icosahedral grid: 162, 642 and 2562 cells.*

Definition 2.3. (Delaunay triangulation) A Delaunay triangulation is a triangulation where each spherical triangle is circumscribed in a circumference that does not contain any vertex.

The Delaunay triangulation is the dual grid of a Voronoi diagram in a graph theory sense. Given a Voronoi diagram, the dual relation can be seen by connecting the neighbor generators. This process yields a Delaunay triangulation. On the other hand, given a Delaunay triangulation, a Voronoi diagram may be constructed by connecting neighbor triangle circumcenters (Okabe *et al.*, 2000). Each Voronoi cell is related to one Delaunay vertex and each Delaunay triangle is related to one Voronoi vertex. Each Delaunay edge is related to one Voronoi edge and they are orthogonal. This property is desirable for numerical schemes. At last, we call the Delaunay triangulation the dual grid and the Voronoi diagram as the primal grid or Voronoi grid.

An important example of Voronoi diagram and Delaunay triangulation is the icosahedral grid and the pentagonal/hexagonal grid. The icosahedral construction begins with an icosahedron inscribed within a sphere. Its edges are projected gnomonically on the sphere surface. Each resulting spherical triangle is subdivided into 4 triangles by connecting the midpoints of the edges. The new triangles can be subdivided and we can proceed recursively. This process is illustrated in Figure 2.1. The grid constructed from the initial icosahedron has 12 vertices. Given a level of recursion l for the process described for refinement of the grid, it can be showed that the grid has $N_l = 10 \cdot 2^{2l} + 2$ vertices. Also, this construction yields a Delaunay triangulation. Therefore, a Voronoi diagram may be obtained by connecting the circumcenters of the spherical triangles (Miura e Kimoto, 2005). In Figure 2.2 we show examples of Voronoi diagrams on the sphere.

2.2   Spherical centroidal Voronoi tesselation

A Spherical centroidal Voronoi tesselation (SCVT) is a Voronoi diagram where the generators are the center of mass of each cell with respect to a density function. Formally, we have the following definitions.

Definition 2.4. (Center of mass) Let Ω be a spherical polygon and $\rho \in C(\mathcal{S}^2)$, $\rho : \mathcal{S}^2 \to]0, \infty[$, we define the center of mass with respect to ρ by

$$x^* = \frac{\int_\Omega x\rho(x)d\Omega(x)}{\int_\Omega \rho(x)d\Omega(x)}.$$

The function ρ if often called density function and the integral above is a surface integral.

This definition of center of mass does not guarantee that $x^* \in \mathcal{S}^2$. Therefore, we have the definition of spherical center of mass.

Definition 2.5. (Spherical center of mass) Let Ω be a spherical polygon and $\rho : \mathcal{S}^2 \to [0, \infty[$. We define the center of mass with respect to ρ as the minimizer of the following functional:

$$F(x) = \int_\Omega \rho(y)\|y - x\|^2 d\Omega(y), \quad x \in \Omega$$

This minimizer is denoted as x^c and the integral above is a surface integral.

In Du *et al.* (2003) the authors have shown that the minimizer always exists. However, it is not always unique. This work also shows that a minimizer may be obtained from the following expression:

$$x^c = \frac{x^*}{\|x^*\|}. \tag{2.1}$$

In other words, we just need to radially project the center of mass from Definition 2.4 on the sphere in order to obtain the spherical center of mass from Definition 2.5.

Definition 2.6. (SCVT) Given $\{x_i\}_{i=1}^n$ and a density function $\rho : \mathcal{S}^2 \to [0, \infty[$, consider the Voronoi regions Ω_i for each i. We say that the Voronoi tesselation $\{\Omega_i\}_{i=1}^n$ is a spherical centroidal Voronoi tesselation (SCVT) with respect to ρ if $x_i = x_i^c$, where x_i^c is the spherical center of mass of Ω_i.

Therefore, SCVT are Voronoi diagrams where the Voronoi generators are the local spherical center of mass with respect to ρ. A natural question is how we can build SCVT. This is possible using an iterative method called Lloyd's method (Du *et al.*, 2003; Ju *et al.*, 2011)

Algorithm 2.7. (Lloyd's method) Given a density function $\rho : \mathcal{S}^2 \to [0, \infty[$ and a number of generators n:

1. Choose n generators points $x_1, \cdots, x_n \in \mathcal{S}^2$;

2. Compute the Voronoi diagram Ω_i for each generator;

3. For each i, compute x_i^* and project onto the sphere using $x_i^c = \frac{x_i^*}{\|x_i^*\|}$;

4. Do $x_i = x_i^c$, $\forall\, i = 1, \cdots, n$;

5. If the new points satisfy some stopping criteria, the return $\{x_i\}_{i=1}^n$ and $\{\Omega_i\}_{i=1}^n$. Otherwise, go back to step 2.

In this work, we use the algorithm developed by Renka (1997) to construct Delaunay Triangulations on the sphere and build the Voronoi Diagrams from the Delaunay triangulations.

The convergence of Lloyd's method is related with an energy functional. Given $x = \{x_i\}_{i=1}^n$ points on the sphere and $\Omega = \{\Omega_i\}_{i=1}^n$ subsets of the sphere satisfying:

1. $\Omega_i \cap \Omega_j \neq \emptyset$, for $i \neq j$,

2. $\bigcup_{i=1}^n \overline{\Omega_i} = \mathcal{S}^2$,

we define the energy functional by:

$$\mathcal{K}(x, \Omega) = \sum_{i=1}^n \mathcal{K}_i(x_i, \Omega_i),$$

where

$$\mathcal{K}_i(x_i, \Omega_i) = \int_{\Omega_i} \rho(y) \|y - x_i\|^2 d\Omega(y).$$

This energy functional decreases for each Lloyd's method iteration. Furthermore, $(\{x_i\}_{i=1}^n, \{\Omega_i\}_{i=1}^n)$ is a local minimum of $\mathcal{K}$ if only if $(\{x_i\}_{i=1}^n, \{\Omega_i\}_{i=1}^n)$ is a SCVT with respect to ρ. Analysing the energy functional, it is also possible to conclude that (Du *et al.*, 2003; Ju *et al.*, 2011),

$$\frac{h_i}{h_j} \approx \left(\frac{\rho(x_j)}{\rho(x_i)} \right)^{\frac{1}{4}}, \tag{2.2}$$

where h_i and h_j denotes the diameters of Ω_i and Ω_j, respectively. This approximation plays a key role in our work. It allows us to build grid with local refinement, as we shall see.

2.3   Example of local refinements in SCVT grids

First, let's define a density function based on Ju *et al.* (2011), that allows us to build a grid that captures the South America continent.

We represent a point $x \in \mathcal{S}^2 \subset \mathbb{R}^3$ in spherical coordinates as,

$$x = (\sin\varphi \cos\theta, \sin\phi \sin\theta, \cos\varphi) \in \mathbb{R}^3, \quad \varphi \in \left[-\frac{\pi}{2}, \frac{\pi}{2} \right], \theta \in [-\pi, \pi], \tag{2.3}$$

and set the parameters $(\varphi_c, \theta_c) = \left(-\frac{\pi}{9}, -\frac{\pi}{3} \right)$, $x_c = (\sin\varphi_c \cos\theta_c, \sin\phi_c \sin\theta_c, \cos\varphi_c)$ and consider the parameters γ, α and ε that will be set later. Then we define:

$$d(x, x_c) = \|x - x_c\|, \quad x \in \mathcal{S}^2, \tag{2.4}$$

where $\| \cdot \|$ denote the Euclidean norm. We define the following auxiliary function:

$$s(x) = \begin{cases} 1, & \text{if } d(x, x_c) \leq \alpha, \\ \frac{\alpha + \varepsilon - d(x, x_c)}{\varepsilon}, & \text{if } \alpha \leq d(x, x_c) \leq \alpha + \varepsilon, \\ 0, & \text{otherwise.} \end{cases} \tag{2.5}$$

Finally, the density function is given by:

$$\rho_1(x) = \frac{1}{\gamma^4} + \left(1 - \frac{1}{\gamma^4} \right) s(x). \tag{2.6}$$

The parameter α represents the radius of the high-resolution grid region. The parameter ε represents the width of the transition zone between coarse and fine grid resolution. The parameter γ represents the ratio between the diameter of a cell in the high-resolution region and a cell in the low-resolution region. This parameter γ is introduced based on Equation (2.2).

Aiming for grids with smooth transition between higher and lower resolution zones, we applied a smoothing filter in the function defined in Equation 2.5 as follows. Firstly, we consider a latitude-longitude grid with 720×1440 points. For each point P on this grid, we consider the value of the function $s(P)$ at this point. This value is then replaced by an average of the values of s at the points of a box centered in P. We considered a box with centered at P with 55^2 points, for each P in the latitude-longitude grid. Bilinear interpolation was employed to compute the values of s at points that are not grid points of the latitude-longitude grid that we defined. We choose the size of the box empirically. Our assessment criteria was so that the generated primal grid has only triangles with circumcenters inside of the corresponding triangles, because this property is desirable in order to guarantee a well staggered grid where the primal and dual edges intersect (Engwirda, 2018).

We set the parameters $\gamma = 3$, $\alpha = \frac{7\pi}{45}$ and $\varepsilon = \frac{\pi}{12}$. Then, for the density function given in Equation (2.6) with smoothing filter we obtain the following grid illustrated in Figure 2.3 after
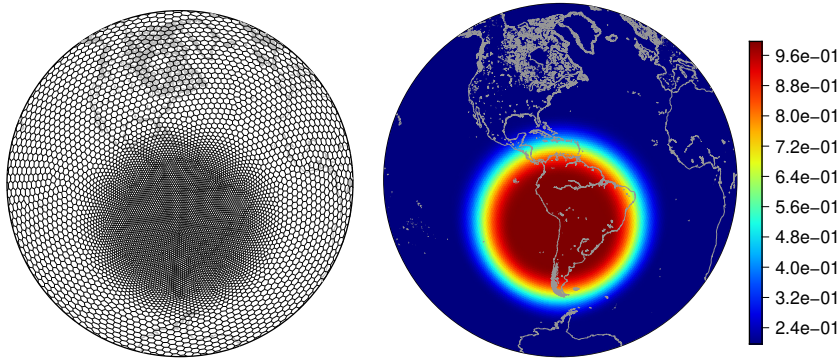
applying Lloyd's algorithm.

Figure 2.3: *Grid generated by Lloyd's algorithm with density function defined by Equation (2.6) considering 10424 generators (left) and the density function defined by Equation (2.6) (right). A smoothing filter was employed.*

An important property of computational grids is the cell distortions. Given a Voronoi cell Ω with edges with lengths $l_1, \cdots, l_n$, the distortion may be given by:

$$S = \frac{\sqrt{\frac{1}{n}\sum_{i=1}^{n}\left(l_i - \bar{l}\right)^2}}{\bar{l}},$$

where

$$\bar{l} = \sqrt{\frac{1}{n}\sum_{i=1}^{n}l_i{}^2}.$$

Note that a cell has zero distortion if, and only if, it has equal edge lengths. In Figures 2.4, 2.5 and 2.6 we show the diameters and distortion properties, respectively, of the grid showed in Figure 2.3. Also, note that the cells within the South America region have diameter approximately 3 times smaller than in most of the globe.
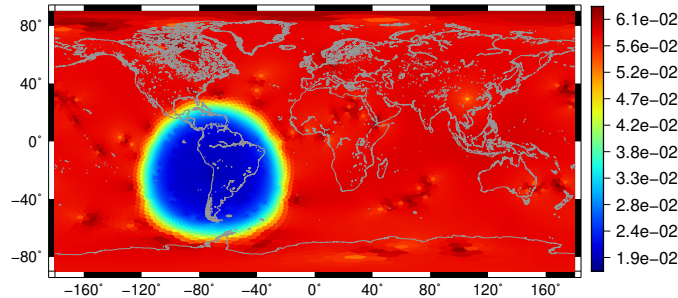
Figure 2.4: *Diameters (radians) of the cells considering the grid showed in Figure 2.3.*
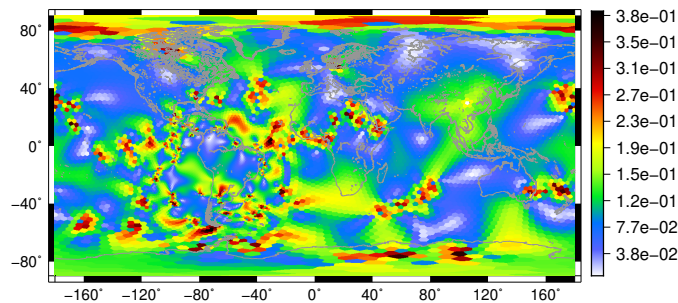

Figure 2.5: *Distortion of the cells considering the grid showed in Figure 2.3.*
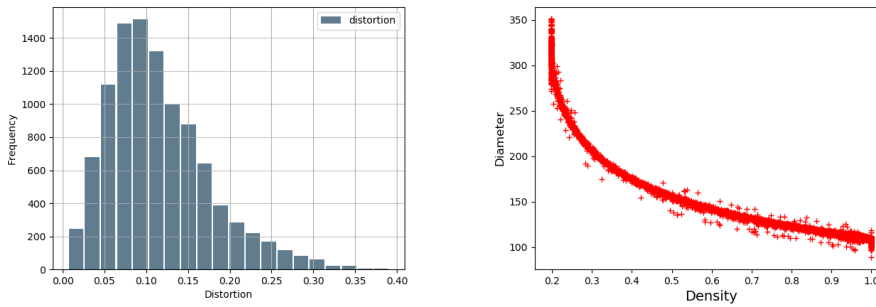
Figure 2.6: *Distortion histogram (left) and diameters of cells (km) vs density function values (right) considering the grid and density function showed in Figure 2.3.*

Aiming to build grids that represent well the Andes mountain, we can define a density function based on topography. Indeed, the data from ETOPO (Amante e Eakins, 2009) has the Earth topography defined in a latitude-longitude grid. In order to build a grid that captures the Andes, we removed all the data from ETOPO except the Andes. Even though the ETOPO data is given for a high resolution, we used in this work the ETOPO data in a latitude-longitude grid with 720×1440 points since this number of points showed to represent well the Andes' topography in our simulations. We also applied a smoothing technique on ETOPO data to produce a smooth density function and therefore a grid with smooth transitions between coarser and finer regions. The employed smoothing technique was based on Jacobi method for the Poisson equation on a rectangular domain. For each index (i,j) representing a point on the latitude-longitude grid, $0 \leq i \leq 720$, $0 \leq j \leq 1440$, we consider the following iterative process:

$$b_{ij}^{k+1} = \frac{1}{4}(b_{i-1,j}^k + b_{i+1,j}^k + b_{i,j-1}^k + b_{i,j+1}^k),$$

where $k \geq 0$ and b_{ij}^0 is the initial Andes data from ETOPO on the latitude-longitude grid.

The maximum number of iterations used was 500 iterations and it was chosen empirically. We used again as an assessment criteria that the generated primal grids have all circumcenters inside the triangles. The resulting data is normalized to enforce values in $[0,1]$. Applying bilinear interpolation on this latitude-longitude grid data, we have a function $b(\phi, \lambda)$ that represents a smooth Andes topography. Thus, the proposed density function may be built as:

$$\rho_2(\phi, \lambda) = \frac{1}{\gamma^4} + \left(1 - \frac{1}{\gamma^4}\right)b(\phi, \lambda). \tag{2.7}$$

The resulting grids and its properties after applying Lloyd's method for the the density function ρ_2 are illustrated in Figures 2.7, 2.8, 2.9 and 2.10 for $\gamma = 3$.
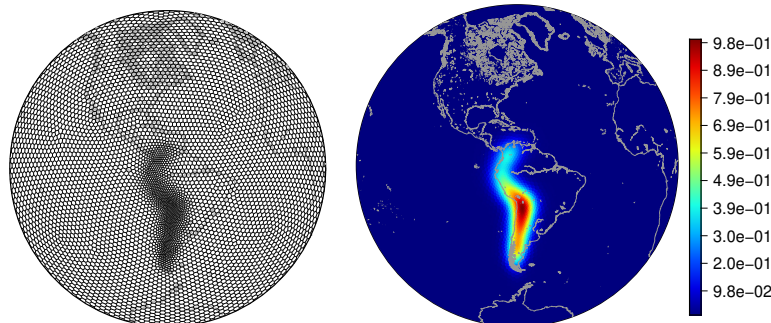

Figure 2.7: *Grid generated by Lloyd's algorithm with density function defined by Equation (2.7) considering 10424 generators (left) and the density function defined by Equation (2.7) (right). A smoothing filter was employed.*
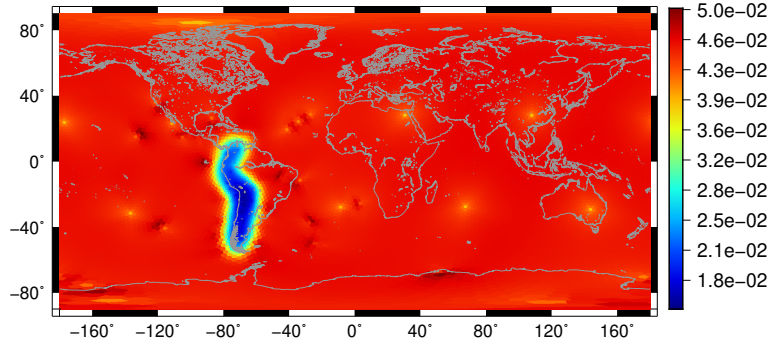
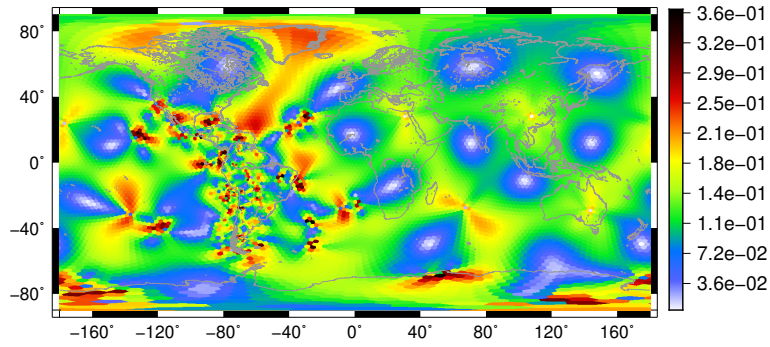**Figure 2.8:** *Diameters (radians) of the cells considering the grid showed in Figure 2.7.*

Figure 2.9: *Distortion of the cells considering the grid showed in Figure 2.7.*
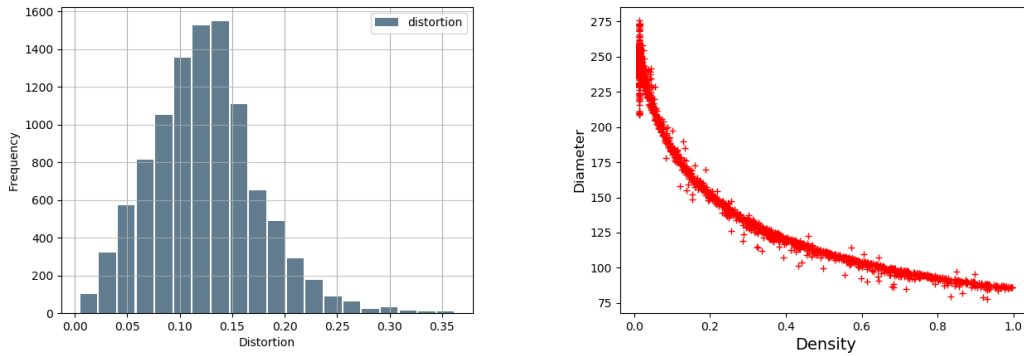

Figure 2.10: *Distortion histogram (left) and diameters of cells (km) vs density function values (right) considering the grid and density function showed in Figure 2.7.*

Finally, we can build a grid that represents well the Andes, has a refinement over South America and has a smooth transition to global grid. Such a grid can be built by setting the following density function based on the auxiliary function s defined in Equation (2.5) and the smoothed Andes topography b used in Equation (2.7):

$$\rho_3(x) = \frac{1}{\gamma^4} + \left(1 - \frac{1}{\gamma^4}\right)(\lambda s(x) + (1 - \lambda)b(x)), \quad x \in \mathcal{S}^2 \tag{2.8}$$

where we are assuming that the respective smoothing was applied for each function and $\lambda \in [0, 1]$.

We illustrate the generated grids using ρ_3 with $\gamma = 3$ and $\lambda = 0.6$ on Figures 2.11, 2.12, 2.13 and 2.14. For this value of γ, we expect a resolution 3 times higher on the Andes mountain from Equation (2.2) and it is illustrated in Figure 2.12.
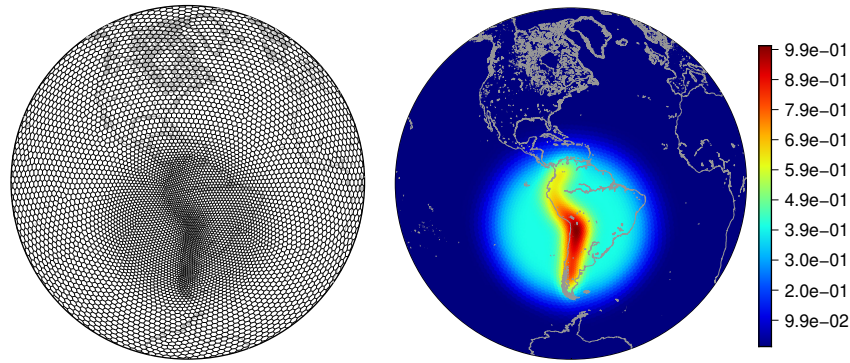
Figure 2.11: *Grid generated by Lloyd's algorithm with density function defined by Equation* (2.8) *considering 10424 generators (left) and the density function defined by Equation* (2.8) *(right).*
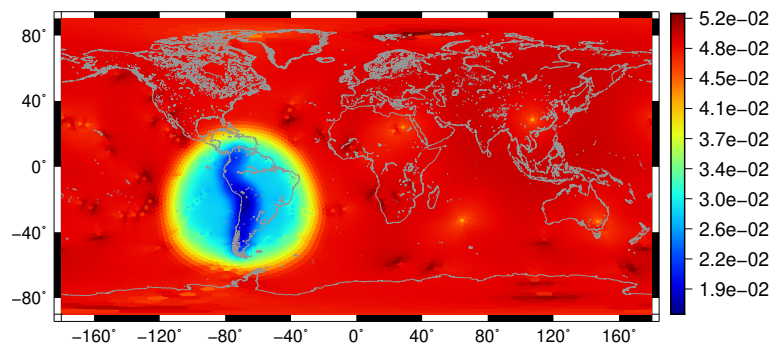

Figure 2.12: *Diameters (radians) of the cells considering the grid showed in Figure* 2.11.
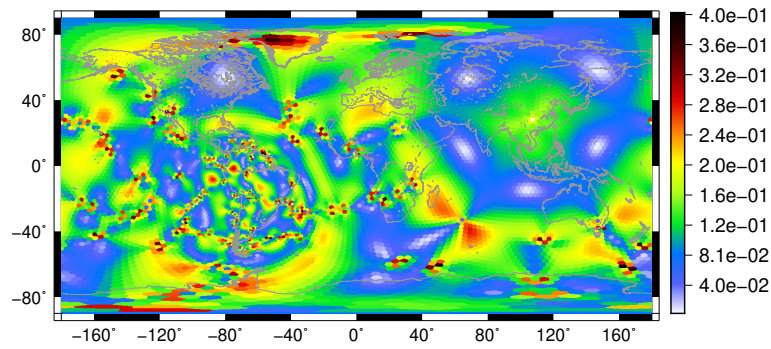

Figure 2.13: *Distortion of the cells considering the grid showed in Figure* 2.11.
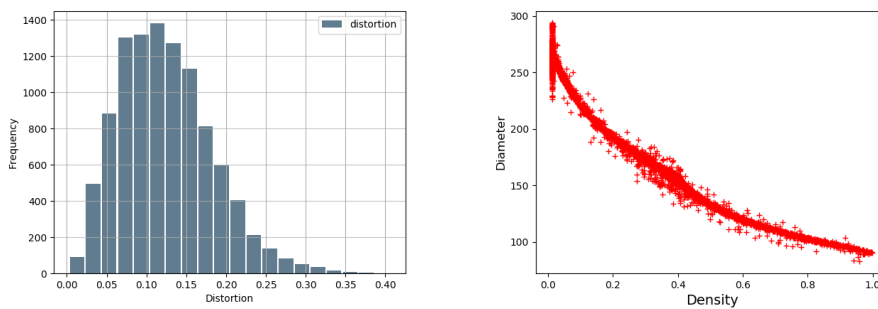

Figure 2.14: *Distortion histogram (left) and diameters of cells (km) vs density function values (right) considering the grid and density function showed in Figure* 2.11.

Let x_i be a Voronoi generator in South America continent such that the generator is not on Andes mountain (*i.e.*, $b(x_i) = 0$ and $s(x_i) = 1$) and x_j be a Voronoi generator on the coarse grid region (*i.e.*, $b(x_j) = s(x_j) = 0$). Denoting the diameters of the Voronoi cells by h_i and h_j, respectively, from Equation (2.2) we have the following approximation:

$$\frac{h_i}{h_j} \approx \left(\frac{\rho(x_j)}{\rho(x_i)}\right)^{\frac{1}{4}} = \frac{\left(\frac{1}{\gamma^4}\right)^{\frac{1}{4}}}{\left[\frac{1}{\gamma^4} + \left(1 - \frac{1}{\gamma^4}\right)\lambda\right]^{\frac{1}{4}}} = \frac{1}{\left[(1 - \lambda) + \lambda\gamma^4\right]^{\frac{1}{4}}}. \tag{2.9}$$

For the values $\gamma = 3$ and $\lambda = 0.6$, we have:

$$\frac{h_i}{h_j} \approx 0.3779645\cdots. \tag{2.10}$$

Therefore, for these parameters, the diameter of a cell in the South American continent that does not lie on Andes mountain is almost 38% the diameter of a cell in the coarse grid region.

This grid generated by ρ_3 is more distorted than the grids generated by ρ_1 and ρ_2. As we can see, distortion is not related with the diameter of a cell. It is not related either with the transition zone between lower and higher resolution refinement.

Another important geometric feature of spherical grids is the concept of alignment of grid cells. This concept was first introduced in Peixoto e Barros (2013), where the authors prove that the alignment of cells is related to the order of accuracy of the usual finite volume discretization of the divergence. We start with the following definition for planar polygons.

Definition 2.8. (Planar aligned polygon) Given a polygon Ω in the plane with even number of edges, we say that Ω is aligned if any two opposite edges are parallel and have the same length.

This concept may be extended to spherical polygons as follows.

Definition 2.9. (Spherical aligned polygon) Given a spherical polygon Ω with even number of edges, denote P_0 the center of mass of Ω with respect to a constant density function. Let Ω' be the planar polygon obtained by radial projection of the edges of Ω onto tangent plane at P_0. We say that Ω is aligned if the planar polygon Ω' is aligned.

Finally, Peixoto e Barros (2013) defines a quantity known as alignment index denoted by Θ that gives a measurement of a cell alignment.

Definition 2.10. (Alignment index) Given a spherical polygon Ω with even number of edges n, denote its vertices by P_i, $i = 1, \cdots, n$ and consider $P_{n+1} = P_1$. The alignment index is defined by:

$$\Theta(\Omega) = \frac{1}{n\bar{d}} \sum_{i=1}^{\frac{n}{2}} |d_{i+1+n/2,i} - d_{i+n/2,i+1}| + |d_{i+1,i} - d_{i+n/2+1,i+n/2}|,$$

where $\bar{d} = \frac{1}{n} \sum_{i=1}^{n} d_{i,i+1}$ and $d_{i,j}$ is the geodesic distance between P_i and P_j.

It can be proven that a spherical polygon Ω is aligned if and only if $\Theta(\Omega) = 0$. In Figure 2.15 we show the alignment index for the grid showed in Figure 2.11. It is worth noticing that there are distorted cells (Figure 2.13) that are not ill aligned.
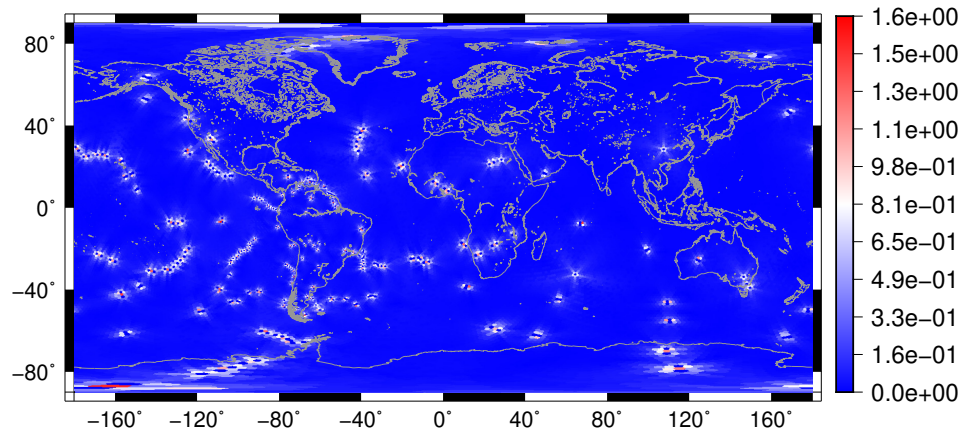
Figure 2.15: *Alignment index distribution considering the grid showed in Figure 2.11.*

From our simulations we can conclude that SCVT and Lloyd's method are a very flexible tool to build grids with local refinement. The key idea is to define an adequate density function for our purposes. We will investigate the numerical methods for the grids generated by the density function ρ_3 defined in Equation (2.8) in Chapters 4 and 5.

Chapter 3

Shallow water model and finite volume scheme

Aiming to solve numerically the shallow water equations on the sphere, there are at least two crucial choices to make. We must choose how we formulate the continuous equations and how we discretize it. This chapter aims to explain how we made the above choices. We describe the shallow water equations on the sphere and some of its properties in Section 3.1. We also present these equations in the vector-invariant form, which will be adequate for our purposes. At last, in Section 3.2, we describe the finite volume discretization presented in Thuburn *et al.* (2009) and Ringler *et al.* (2010).

3.1 Shallow water equations

The shallow water equations can de be thought as a model for horizontal motions of a fluid in a rotating frame where the vertical scale is negligible when compared to the horizontal scale. They can be deduced from the primitive equations for both planar and spherical geometry. Their deduction may be found in Haltiner e Williams (1980); Holton (2004). We will consider only the spherical case in this work.

There are many ways to formulate the shallow water equations. A review for some of these formulations may be found in Williamson *et al.* (1992). The shallow water equations on the rotating sphere can be written in spherical coordinates as:

$$\frac{\partial u}{\partial t} + \frac{u}{a\cos\phi}\frac{\partial u}{\partial \lambda} + \frac{v}{a}\frac{\partial u}{\partial \phi} - fv - \frac{uv}{a}\tan\phi + \frac{g}{a\cos\phi}\frac{\partial(h+b)}{\partial \lambda} = 0, \tag{3.1}$$

$$\frac{\partial v}{\partial t} + \frac{u}{a\cos\phi}\frac{\partial v}{\partial \lambda} + \frac{v}{a}\frac{\partial v}{\partial \phi} + fu + \frac{u^2}{a}\tan\phi + \frac{g}{a}\frac{\partial(h+b)}{\partial \phi} = 0, \tag{3.2}$$

$$\frac{\partial h}{\partial t} + \frac{1}{a\cos\phi}\left(\frac{\partial}{\partial \lambda}(hu) + \frac{\partial}{\partial \phi}(hv\cos\phi)\right) = 0. \tag{3.3}$$

Here (λ, ϕ) are the latitude-longitude coordinate system on the sphere, with $-\pi < \lambda \leq \pi$ and $-\frac{\pi}{2} \leq \phi < \frac{\pi}{2}$. The prognostic variables are the fluid depth $h = h(\lambda, \phi, t)$, the longitudinal component of the velocity $u = u(\lambda, \phi, t)$ and the latitudinal component of the velocity $v = v(\lambda, \phi, t)$.

The parameters are the bottom topography, $b = b(\lambda, \phi)$, the gravity acceleration constant, g, the earth radius, a, and the Coriolis term, $f = 2\Omega\sin\phi$, where $\Omega = \frac{2\pi a}{86400}$ is the earth angular velocity. Equations (3.1) and (3.2) are the momentum equations and equation (3.3) is the continuity equation.

We define a local coordinates system $\{\mathbf{i}, \mathbf{j}, \mathbf{k}\}$ at each point of the sphere where $\mathbf{i}, \mathbf{j}$ and $\mathbf{k}$ are the longitudinal, latitudinal and upward direction unit vectors. In this model, the velocity vector $\mathbf{v} = u\mathbf{i} + v\mathbf{j}$ is tangent to the sphere.

Since the fluid is considered to lay on the sphere surface, the boundary conditions are periodic in λ and ϕ. Finally, we are interested in the initial value problem related with the shallow water equations, i.e., we consider the initial conditions $h_0(\lambda, \phi) = h(\lambda, \phi, 0)$, $u_0(\lambda, \phi) = u(\lambda, \phi, 0)$ and $v_0(\lambda, \phi) = v(\lambda, \phi, 0)$ to be given.

3.1.1 Vector-invariant formulation

With the aid of the following identities for the gradient and divergence operators on spherical coordinates:

$$\nabla(\cdot) = \frac{1}{\cos \phi} \frac{\partial}{\partial \lambda}(\cdot)\mathbf{i} + \frac{\partial}{\partial \phi}(\cdot)\mathbf{j}, \tag{3.4}$$

$$\nabla \cdot \mathbf{v} = \frac{1}{a \cos \phi} \left(\frac{\partial u}{\partial \lambda} + \frac{\partial}{\partial \phi}(v \cos \phi) \right), \tag{3.5}$$

we can write the shallow water equations in a vector form:

$$\frac{d\mathbf{v}}{dt} = -f\mathbf{k} \times \mathbf{v} - g\nabla(h + b), \tag{3.6}$$

$$\frac{dh}{dt} + h\nabla \cdot \mathbf{v} = 0, \tag{3.7}$$

where

$$\frac{d}{dt}(\cdot) = \frac{\partial}{\partial t}(\cdot) + (\mathbf{v} \cdot \nabla)(\cdot) \tag{3.8}$$

denotes the material derivative. This formulation is known as advective form (Williamson *et al.*, 1992). As we pointed out, this formulation uses local coordinates systems on the sphere. However, it is possible to write these equations in a cartesian form.

In Cote (1988) it has been shown that the shallow water equations can be expressed using three-dimensional cartesian coordinates as:

$$\frac{d\mathbf{V}}{dt} = -f\mathbf{k} \times \mathbf{V} - g\nabla(h + b) + \mu k, \tag{3.9}$$

$$\frac{dh}{dt} + h\nabla \cdot \mathbf{V} = 0. \tag{3.10}$$

Here $\mathbf{V} = (u, v, w) \in \mathbb{R}^3$, $\mathbf{k}$ is an unit vector in radial direction. The parameter $\mu = -\frac{\mathbf{V} \cdot \mathbf{V}}{a}$ is a Lagrange multiplier and it is included to guarantee that $\mathbf{V}$ stays constrained to be tangent to sphere ($\mathbf{k} \cdot \mathbf{V} = 0$). Notice that equations (3.9) and (3.10) are similar to equations (3.6) and (3.7), the only difference is the Lagrange multiplier term and the number of components of the velocity vector.

Defining the relative vorticity $\xi = \mathbf{k} \cdot \nabla \times \mathbf{V}$, we have the following relation (Satoh, 2004),

$$\nabla \times \mathbf{V} = \xi\mathbf{k} + \mathbf{k} \times \frac{\mathbf{V}}{a}. \tag{3.11}$$

Taking the cross product with $\mathbf{V}$ in (3.11) yields:

$$(\nabla \times \mathbf{V}) \times \mathbf{V} = \xi\mathbf{k} \times \mathbf{V} + \left(\mathbf{k} \times \frac{\mathbf{V}}{a} \right) \times \mathbf{V} = \xi\mathbf{k} \times \mathbf{V} - \frac{\mathbf{V} \cdot \mathbf{V}}{a}\mathbf{k} \quad . \tag{3.12}$$

Considering the identity:

$$(\mathbf{V} \cdot \nabla)\mathbf{V} = (\nabla \times \mathbf{V}) \times \mathbf{V} + \nabla\left(\frac{|\mathbf{V}|^2}{2} \right), \tag{3.13}$$

and combining (3.12) and (3.13), we get:

$$(\mathbf{V} \cdot \nabla)\mathbf{V} = \xi \mathbf{k} \times \mathbf{V} - \frac{\mathbf{V} \cdot \mathbf{V}}{a}\mathbf{k} + \nabla\left(\frac{|\mathbf{V}|^2}{2}\right). \tag{3.14}$$

Finally, we substitute (3.8) and (3.14) in (3.9) and eliminate the Lagrange multiplier to get:

$$\frac{\partial \mathbf{V}}{\partial t} = -(f + \xi)\mathbf{k} \times \mathbf{V} - g\nabla(h + b) - \nabla\left(\frac{|\mathbf{V}|^2}{2}\right), \tag{3.15}$$

$$\frac{\partial h}{\partial t} + \nabla \cdot (h\mathbf{V}) = 0. \tag{3.16}$$

Equation (3.15) is called the vector-invariant form of the momentum equations. This is why we say that equations (3.15) and (3.16) are the shallow water equations in the vector-invariant form. We can express these equations in vector-invariant form in terms of kinectic energy $K = \frac{|\mathbf{V}|^2}{2}$, potential vorticity $q = \frac{f+\xi}{h}$, Bernoulli potential $B = \Phi + K$, where $\Phi = g(h+b)$ is the geopotential, and the perpendicular velocity term $\mathbf{V}^\perp = \mathbf{k} \times \mathbf{V}$ as follows:

$$\frac{\partial \mathbf{V}}{\partial t} = -qh\mathbf{V}^\perp - \nabla B, \tag{3.17}$$

$$\frac{\partial h}{\partial t} = -\nabla \cdot (h\mathbf{V}). \tag{3.18}$$

The vector-invariant formulation is also valid for planar geometry and does not depend on the coordinate system. In this formulation we don't have to deal with the non-linear advection, which is a problematic term for conservation of potential vorticity and energy (Ringler *et al.*, 2010). Therefore, this formulation will be used in our discretization.

Proceeding as in Ringler *et al.* (2010), we can derive the energy budget. Multiplying equation (3.17) by $h\mathbf{V}$ and using that $\mathbf{V}^\perp \cdot \mathbf{V} = 0$ we obtain:

$$(h\mathbf{V}) \cdot \frac{\partial \mathbf{V}}{\partial t} = -\nabla B \cdot (h\mathbf{V}) \Rightarrow h\frac{\partial K}{\partial t} = -\nabla B \cdot (h\mathbf{V}). \tag{3.19}$$

Multiplying equation (3.18) by K, we get:

$$K \cdot \frac{\partial h}{\partial t} = -K(\nabla \cdot (h\mathbf{V})). \tag{3.20}$$

Combining (3.19) and (3.20) yields the kinetic energy evolution equation:

$$\begin{aligned}
\frac{\partial (hK)}{\partial t} &= -K(\nabla \cdot (h\mathbf{V})) - \nabla B \cdot (h\mathbf{V}) \\
&= -K(\nabla \cdot (h\mathbf{V})) - \nabla K \cdot (h\mathbf{V}) - \nabla\Phi \cdot (h\mathbf{V}) \\
&= -\nabla \cdot (hK\mathbf{V}) - \nabla\Phi \cdot (h\mathbf{V})
\end{aligned} \tag{3.21}$$

Multiplying the equation (3.18) by Φ, we get the potential energy equation:

$$\frac{\partial (g\frac{h^2}{2} + ghb)}{\partial t} = -\Phi\nabla \cdot (h\mathbf{V}) \quad . \tag{3.22}$$

The energy is given by:

$$E = g\frac{h^2}{2} + ghb + hK \quad , \tag{3.23}$$

and its equation can be obtained by combining (3.21) and (3.22)

$$\frac{\partial E}{\partial t} + \nabla \cdot (hK\mathbf{V}) = -\nabla \cdot (\Phi(h\mathbf{V})) \quad . \tag{3.24}$$

Therefore, we can write the time derivative of energy as the divergence of a function. Integrating Equation (3.24) on the sphere using differentiation under the integral sign, divergence theorem and noticing that the sphere does not have boundary, we can conclude the total energy is conserved. Notice that the Coriolis term does not contribute in the energy bugdet because of $\mathbf{V}^{\perp} \cdot \mathbf{V} = 0$. This property is highly desirable for a numerical scheme and much attention will be given to this property.

It is also worth to write the linearised shallow water equations about a rest state with depth h_0:

$$\frac{\partial \mathbf{V}}{\partial t} = -f\mathbf{V}^{\perp} - \nabla(h + b) \quad , \tag{3.25}$$

$$\frac{\partial h}{\partial t} = -h_0\nabla \cdot \mathbf{V} \quad . \tag{3.26}$$

We also consider the linear vorticity equation:

$$\frac{\partial \xi}{\partial t} + f\delta = 0 \quad . \tag{3.27}$$

This equation can be obtained applying the operator $\mathbf{k} \cdot \nabla \times (\cdot)$ in the linearised momentum equation (3.25). The linearised equations will be useful to motivate some discretization aspects.

3.2   TRSK

This subsection is dedicated to present TRSK, a C-staggering finite volume/difference method developed for the shallow water equations. TRSK was first presented for the linear shallow water equations on a f-sphere, i.e., the Coriolis parameter is constant in the whole sphere (Thuburn *et al.*, 2009). The goal was to develop a numerical scheme that preserves stationary geostrophic modes. Then, this work was extended to the non-linear shallow water equations with f variable (Ringler *et al.*, 2010). In these works, they use grids with orthogonal dual grids, such as the latitude-longitude grid, icosahedral and pentagonal/hexagonal grid. Later, TRSK was extended to grids with a nonortho-gonal dual grid, such as the conformal cubed sphere (Thuburn e Cotter, 2012) and other grids (Weller, 2014). TRSK has become popular for its conservative and mimetic properties and became adopted in the atmospheric model MPAS (Skamarock *et al.*, 2012), as well as in the DYNAMICO model (Dubos *et al.*, 2015).

In this subsection, we shall describe TRSK for the non-linear shallow water equations. The grids are supposed to have an orthogonal dual grid, which is the case that we are interested in this work.

3.2.1   Definitions

We start with a primal grid that has an orthogonal dual grid. For instance, the grid generated by a Voronoi diagram on the sphere and its Delaunay triangulation. There are three types of grid locations that are necessary for a C-grid staggering: primal cell centers (or dual vertices), the primal cell vertices (or dual cell centers) and the point where the primal edges and dual edges intersect each other (Figure 3.1). The indexes i, e and v stand for primal centers, intersecting edges points and vertices. The length of an edge of a primal cell and a dual cell is denoted as d_e and l_e, respectively.
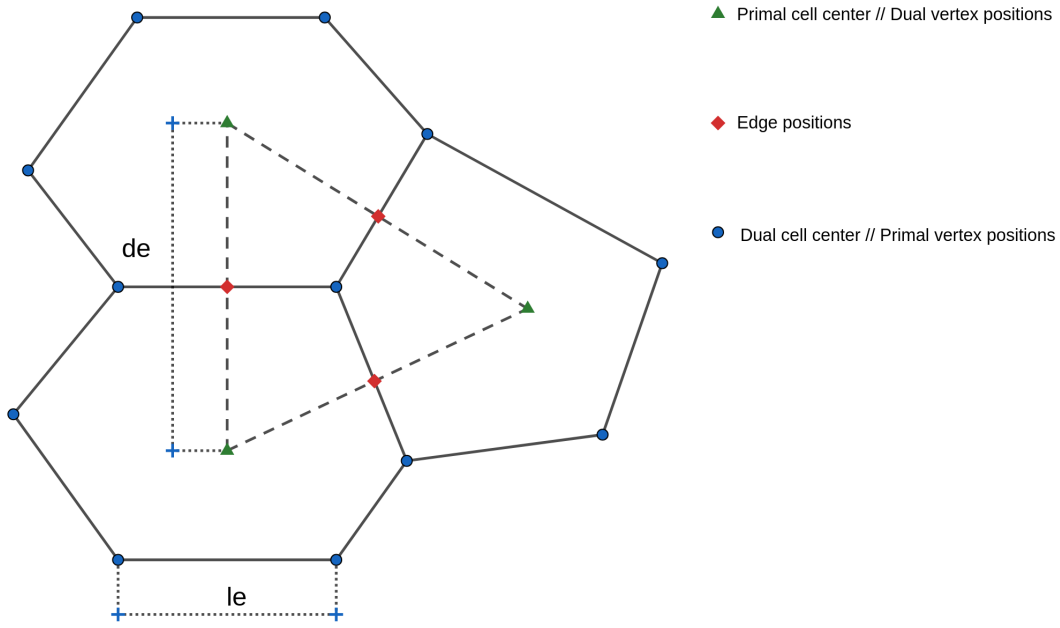
Figure 3.1: *Geometric definitions in primal and dual cells.*

We will denote the velocity field $\mathbf{V}$ in equation (3.17) by $\mathbf{u}$. The prognostic variables h and $\mathbf{u}$ are stored in primal cell center and edges points, respectively. The divergence $\delta = \nabla \cdot \mathbf{u}$ is stored in primal cell center and the relative vorticity $\xi = \mathbf{k} \cdot \nabla \times \mathbf{u}$ is stored at the primal vertices, as it is shown in Figure 3.2. Only the normal component of the velocity field is stored. Therefore, at each edge point we define a normal vector $\mathbf{n}_e$ to the edge pointing to the direction such that the normal component of the velocity given by $\mathbf{u} \cdot \mathbf{n}_e$ is positive. Given a primal cell i and an edge e, n_{ei} is an indicator function such that $n_{ei} = 1$ if $\mathbf{n}_e$ points out of cell i and $n_{ei} = -1$ if $\mathbf{n}_e$ points into cell i. Finally, given a vertex v, we define $\mathbf{t}_e = \mathbf{k} \times \mathbf{n}_e$ and an indicator function t_{ev} such that $t_{ev} = 1$ if $\mathbf{t}_e$ points towards v and $t_{ev} = -1$ otherwise.
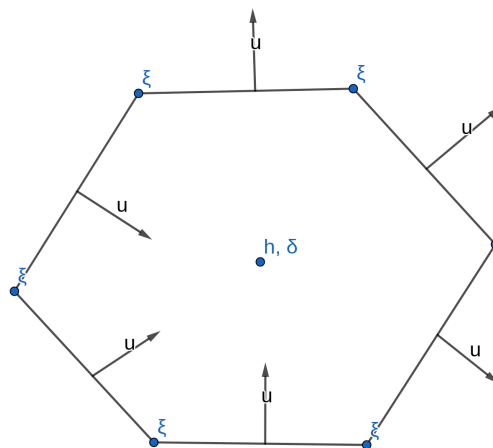

Figure 3.2: *Variable positions for a C-grid staggering.*

We also define useful indexes and notations for grid connectivity in Table 3.1.

Description	Simbol
Edges of a cell i	$EC(i)$
Vertices of a cell i	$VC(i)$
Vertices at end of edge e	$VE(e)$
Cells that share edge e	$CE(e)$
Edges that has v at its extreme point i	$EV(v)$
Cells with v as a vertex	$CV(v)$
Pair of cells sharing en edge e	$ECP(e)$
Edges with vertex v where each edge share a cell with e	$EVE(v, e)$
Pair of edges that meet at a vertex v of cell i e	$EVC(v, i)$
Area of a primal cell i	A_i
Area of a dual cell v	A_v
Center of a primal cell i	x_i
Edge point	x_e
Primal cell vertex point	x_v

Table 3.1: *Grid notation following Ringler et al. (2010).*

3.2.2   Discretized equations

Given an edge e, a cell i and taking the dot product of (3.17) with $\mathbf{n}_e$, we get:

$$\frac{\partial u_e}{\partial t} = -[qh\mathbf{u}^\perp]_e - [\nabla B]_e, \tag{3.28}$$

$$\frac{\partial h_i}{\partial t} = -[\nabla \cdot (h\mathbf{u})]_i, \tag{3.29}$$

where h_i denotes the height field in a primal cell center i, u_e is the normal component of the velocity at edge e, i.e., $u_e = \mathbf{u}(x_e, t) \cdot \mathbf{n_e}$ and

$$[qh\mathbf{u}^\perp]_e = q(x_e, t)h(x_e, t)\mathbf{u}^\perp(x_e, t) \cdot \mathbf{n_e},$$
$$[\nabla B]_e = \nabla B(x_e, t) \cdot \mathbf{n_e},$$
$$[\nabla \cdot (h\mathbf{u})]_i = \nabla \cdot (h\mathbf{u})(x_i, t).$$

Notice that $\mathbf{u}^\perp(x_e, t) \cdot \mathbf{n_e}$ gives the tangential component of the velocity. Our task now is to discretize te operators $[\nabla \cdot (h\mathbf{u})]_i, [qh\mathbf{u}^\perp]_e$ and $[\nabla B]_e$.

Divergence

We start with the continuity equation (3.29). Denoting a primal cell by Ω_i and its boundary by $\partial\Omega_i$, our approximation is based on the mean of $\nabla \cdot (h\mathbf{u})$ over a cell Ω_i, as it is usual in a finite volume approach. The proposed approximation reads:

$$[\nabla \cdot (h\mathbf{u})]_i = \frac{1}{|A_i|} \int_{\Omega_i} \nabla \cdot (h\mathbf{u}) d\Omega_i. \tag{3.30}$$

This integral can be computed using the divergence theorem. Therefore:

$$[\nabla \cdot (h\mathbf{u})]_i = \frac{1}{|A_i|} \int_{\partial\Omega_i} h\mathbf{u} \cdot \mathbf{n} d(\partial\Omega_i) = \frac{1}{A_i} \sum_{e \in EC(i)} \int_e h\mathbf{u} \cdot \mathbf{n} dl, \tag{3.31}$$

where in the last equality we used that Ω_i is a polygonal with edges e. Since we are using a C staggered grid, the line integral over primal edges above can be estimated as:

$$\int_e h\mathbf{u} \cdot \mathbf{n}dl \approx h_e u_e n_{ei} l_e. \tag{3.32}$$

In the expression above, we need to interpolate the values of h from cell centers positions to edges positions. This can be done as:

$$h_e = \frac{1}{2} \sum_{i \in CE(e)} h_i. \tag{3.33}$$

In other words, the estimated value at an edge point is the average of values in cells either side of e. Thus, we have the following approximation for each cell i:

$$[\nabla \cdot (h\mathbf{u})]_i \approx \frac{1}{A_i} \sum_{e \in EC(i)} h_e u_e n_{ei} l_e. \tag{3.34}$$

The interpolation (3.33) is second-order accurate, since the edge point and either side primal cell center lie on the same geodesic. However, as pointed by Peixoto (2016), the integral approximation (3.32) is only first-order accurate on SCVT grids, since the edge point lying on the dual edge is not the midpoint of the corresponding primal edge.

The discretization of the divergence used above has been investigated in Peixoto e Barros (2013). They analyze the grid imprinting caused by this discretization and concludes that this pattern is related to a concept of aligned cells. They prove that this discretization is second-order only for aligned cells and similar results hold for the curl discretization that we shall present in this work.

Gradient of $h + b$

In the Bernoulli potential gradient discretization, we need to discretize the total fluid depth $h + b$ gradient. Since we need only the normal component value at edges points and $h + b$ is stored at primal cell centers, we can use a centered second-order finite difference scheme:

$$[\nabla(h + b)]_e = -\frac{1}{d_e} \sum_{i \in CE(e)} (h_i + b_i)n_{e,i}. \tag{3.35}$$

Curl

In order to evaluate the perpendicular term $[qh\mathbf{u}^\perp]_e$, we need to estimate the potential vorticity q at the edges. For this reason, we must discretize the relative vorticity (curl).

We start estimating the curl at vertices positions using again a finite volume approach. Given a vertex v, let Δ_v be the corresponding dual cell and

$$\xi_v = \frac{1}{A_v} \int_{\Delta_v} (\mathbf{k} \cdot \nabla \times \mathbf{u}) \cdot \mathbf{n}d\Delta. \tag{3.36}$$

At vertice positions, the vorticity can be calculated by applying Stoke's theorem. Therefore,

$$\xi_v = \frac{1}{A_v} \int_{\partial\Delta_v} \mathbf{u} \cdot \mathbf{t}d\partial\Delta = \sum_{e \in EV(v)} \int_e \mathbf{u} \cdot \mathbf{t}dl. \tag{3.37}$$

These line integrals over dual edges can be estimated with:

$$\int_e \mathbf{u} \cdot \mathbf{t}_e dl \approx d_e u_e t_{ev}, \tag{3.38}$$

and the curl discretization may be given by:

$$\xi_v = \frac{1}{A_v} \sum_{e \in EC(i)} u_e t_{ev} d_e. \tag{3.39}$$

In the case of SCVT grids, the discretization (3.38) is the midpoint rule, since the point of dual edge the intersects a primal edge is the midpoint of the dual edge. This follows from the definition of Voronoi diagram. Hence, this discretization is second-order accurate.

Finally, the curl at an edge e is an average of the curl at vertices at the ends of e.

$$\xi_e = \frac{1}{2} \sum_{v \in VE(e)} \xi_v. \tag{3.40}$$

This interpolation is only first-order accurate on SCVT grids. The reason is again related to the fact of the edge point does not coincide with the edge midpoint.

Perpendicular term

Since now we know how to evaluate the relative vorticity and the height at edge positions, we need to estimate the tangential component of the velocity $u^\perp$ at the edges to compute the complete perpendicular term $[qh\mathbf{u}^\perp]_e$. This discretization will be constructed aiming to guarantee the preservation of stationary geostrophic modes on the f-sphere. The construction builds up from the linearised vorticity equation (3.27) assuming f constant (Thuburn *et al.*, 2009),. Note that the discretization of the linear momentum equation (3.25) on the f-sphere reads:

$$\frac{\partial u_e}{\partial t} = -f[\mathbf{u}^\perp]_e - [\nabla(h+b)]_e. \tag{3.41}$$

Let the tangential velocity be given by:

$$u_e^\perp = \frac{1}{d_e} \sum_{e' \in ECP(e)} w_{ee'} l_{e'} u_e. \tag{3.42}$$

Our task is to find the weights $w_{ee'}$. Differentiating Equation (3.39) with respect to t, we get:

$$A_v \frac{\partial \xi_v}{\partial t} = \sum_{e \in EC(i)} \frac{\partial u_e}{\partial t} t_{ev} d_e = -f \sum_{v \in EV(v)} u_e^\perp t_{ev} d_e - \sum_{e \in EV(v} [\nabla(h+b)]_e t_{ev} d_e. \tag{3.43}$$

Using Equation (3.35), we have:

$$\begin{aligned} \sum_{e \in EC(i)} [\nabla(h+b)]_e t_{ev} d_e &= - \sum_{e \in EV(v)} \frac{1}{d_e} \sum_{i \in CE(e)} (h_i + b_i) t_{ev} d_e n_{e,i} \\ &= - \sum_{e \in EV(v)} \sum_{i \in CE(e)} (h_i + b_i) t_{ev} n_{e,i} \\ &= 0. \end{aligned} \tag{3.44}$$

This sum vanishes since $(h_i + b_i)$ appears twice with different signs. This property is a discrete version that mimics the property $\nabla \times \nabla F = 0$ for a scalar field F. Thus, using Equation (3.42) we conclude that:

$$A_v \frac{\partial \xi_v}{\partial t} = -f \sum_{e \in EV(v)} \sum_{e' \in ECP(e)} w_{ee'} l_{e'} u_{e'} t_{ev}. \tag{3.45}$$

In order to mimic the vorticity equation (3.27), we should have:

$$A_v \frac{\partial \xi_v}{\partial t} = -f A_v \delta_v. \tag{3.46}$$

Where δ_v denotes a discretization of divergence of velocity at edges. We can compute the divergence of velocity in cell centers (denoted by δ_i) in a similar fashion as we did in (3.34). The values at a vertex v may be interpolated from the centers using:

$$\delta_v = \frac{1}{A_v} \sum_{i \in CV(v)} R_{iv} A_i \delta_i = \frac{1}{A_v} \sum_{i \in CV(v)} R_{iv} \sum_{e \in EC(i)} n_{ei} l_e u_e. \tag{3.47}$$

The weights R_{iv} satisfies $\sum_{v \in VC(i)} R_{iv} = 1$ in order to guarantee that the global integrals of divergence ($\sum_i A_i \delta_i$ and $\sum_v A_v \delta_v$) are the same.

Combining (3.45),(3.46) and (3.47) we have:

$$\sum_{e \in EV(v)} \sum_{e' \in ECP(e)} w_{ee'} l_{e'} u_{e'} t_{ev} = \sum_{i \in CV(v)} R_{iv} \sum_{e \in EC(i)} n_{ei} l_e u_e \tag{3.48}$$

In Thuburn *et al.* (2009) they show that this system can be uniquely solved and the weights are given by:

$$w_{ee'} t_{ev_2} = \left(\sum_v R_{iv} - \frac{1}{2} \right) n_{e',i}. \tag{3.49}$$

Where the sum varies on vertices over a walk from edge e' to e. The last vertex encountered in this walk is denoted by v_2.

We concluded that this discretization of the tangential velocity ensures a mimetic discrete equation of (3.27). As shown in Thuburn *et al.* (2009), this property guarantees that stationary geostrophic modes are preserved on the f-sphere. This discretization also satisfies the property:

$$\sum_e A_e u_e^{\perp} u_e = 0, \tag{3.50}$$

which is an analogous of $\mathbf{u_e^{\perp}} \cdot \mathbf{u_e} = 0$. The term A_e in Equation (3.50) is the area of the polygon defined by the ends points of e and the centers of cell either side of e.

Kinetic Energy

The kinetic energy is discretized by:

$$K_i = \frac{1}{A_i} \sum_{e \in EC(i)} \frac{A_e}{4} u_e^2; \tag{3.51}$$

As it is shown in Thuburn *et al.* (2009), this discretization ensures a discrete kinetic energy equation consistent with the continuous kinetic energy equation (3.21). The gradient of the Kinetic Energy may be estimated as in (3.35):

$$[\nabla K]_e = -\frac{1}{d_e} \sum_{i \in CE(e)} K_i n_{e,i}; \tag{3.52}$$

The property (3.50) in continuous equations is important to guarantee that the Coriolis term does not contribute to the energy budget, as we saw in Equation (3.19). For the discrete energy, this property also ensures that the discrete Coriolis term does not contribute to the total energy. Indeed, the discrete total energy is given by:

$$E = \sum_e A_e \frac{h_e u_e^2}{2} + \sum_i A_i \left[g h_i \left(\frac{h_i}{2} + b_i \right) \right]. \tag{3.53}$$

This quantity is conserved (within time error truncation). The proof is similar to what we did for the continuous equations since the necessary vector identities hold for this discretization. Property (3.50) is essential to ensure energy conservation.

Laplacian at edges

The shallow water equations do not contain any diffusive term. However, diffusion is employed very often in atmospheric models in order to ensure numerical stability, remove numerical noises and etc. There are other feasible ways mechanisms of dissipation, such as divergence damping, hyperdiffusion and many others (Jablonowski e Williamson, 2011). We choose to work with diffusion as a mechanism of dissipation in this text and we will make it clear when we are using diffusion in the numerical experiment. Notice that diffusion is not part of TRSK, therefore some of its properties may be violated by adding diffusion.

In order to add diffusion in the momentum equation, we introduce the concept of vector Laplacian. Given a vector field $\mathbf{u} = (u, v, w)$, the vector Laplacian is defined by $\Delta\mathbf{u} = (\Delta u, \Delta v, \Delta w)$. The following identity holds:

$$\Delta\mathbf{u} = \nabla(\nabla \cdot \mathbf{u}) - \nabla \times (\nabla \times \mathbf{u}). \tag{3.54}$$

Since we are working with the normal component of velocity at the edges as one of our prognostic variables, we take the dot product of (3.54) with $\mathbf{n_e}$ for each edge e and get:

$$\Delta\mathbf{u}(x_e) \cdot \mathbf{n_e} = \nabla(\nabla \cdot \mathbf{u})(x_e) \cdot \mathbf{n_e} - \nabla \times (\nabla \times \mathbf{u})(x_e) \cdot \mathbf{n_e}. \tag{3.55}$$

The first term on the right-hand side of equation (3.55) is estimated using the divergence theorem and the midpoint rule as we did in equations (3.30) and (3.31) at the Voronoi centers of cells on either side of e. The divergence of $\mathbf{u}$ estimates are stored at Voronoi centers, therefore we can apply finite differences as in (3.35) to estimate the normal component of the divergence gradient.

The second term on the left-hand side of equation (3.55) is estimated as:

$$(\nabla \times (\nabla \times \mathbf{u}))(x_e) \cdot \mathbf{n_e} \approx \nabla\xi(x_e) \cdot \mathbf{t_e}. \tag{3.56}$$

Therefore, this term can be estimated computing the relative vorticity at the endpoints of edge e using (3.39) and the tangential component of relative vorticity gradient may be calculated using a finite difference scheme:

$$\nabla\xi(x_e) = -\frac{1}{l_e} \sum_{v \in VE(e)} \xi_v t_{ev}.$$

The approach for the Laplacian using the identity (3.54) is used in MPAS (Skamarock *et al.*, 2012) and ICON (Wan *et al.*, 2013). In the next chapter, we shall include the vector Laplacian in the momentum equation for some simulations. The vector Laplacian is multiplied by a diffusion coefficient and added to the momentum equation (3.28). Notice that we can define the second-order vector Laplacian $\Delta^2\mathbf{u} = \Delta(\Delta\mathbf{u})$. The second-order vector Laplacian may be calculated applying the scheme described here twice. The second-order Laplacian has been widely used in atmospheric models and it is known as hyperdiffusion (Jablonowski e Williamson, 2011).

Time discretization

We concluded the spatial discretization of the right hand side of equations (3.28) and (3.29). The process presented in this work leads to an ordinary differential equation in the time variable after the spatial variables are discretized, as it is usual in numerical modelling of geophysical fluids. In this work, we use an explicit fourth-order Runge-Kutta scheme, even though other schemes may be used (Durran, 2011).

3.2.3   Mimetic properties

The discrete operators presented here satisfies the following properties:

1. Mass conservation;

2. Coriolis term is not a source/sink of energy ($u_e u_e^\perp = 0$);

3. Total energy is conserved;

4. The stationary geostrophic modes on the f-sphere are preserved;

5. The vector identities $\nabla \times \nabla \mathbf{u} = 0$ and $\nabla \cdot (\mathbf{u}h) = h\nabla \cdot \mathbf{u} + \mathbf{u} \cdot \nabla h$ holds for the discrete operators.

Property 1 is straightforward from the definition of finite volume discretization. Properties 2 and 4 are proved in Thuburn *et al.* (2009). The proof of properties 3 and 5 may be found in Ringler *et al.* (2010). The above properties are known in the literature as mimetic properties. In Staniforth e Thuburn (2012), a list of desirable properties for a dynamical core is made and the properties listed above are included in their list.

Chapter 4

Numerical experiments for shallow water model

This section presents numerical experiments for the shallow water equations on the sphere using the TRSK scheme described in Chapter 3 when applied to grids with local refinement based on topography that capture well the Andes mountain and the South American continent developed in Section 2.3 of Chapter 2. Some of the presented experiments will add the diffusion operator in the momentum equation and we will compare the impact of the diffusion.

The set of test cases for the shallow water equations that will be analysed in our work are the standard tests proposed in the literature provided by Williamson *et al.* (1992) (hereafter Will92) and Galewsky *et al.* (2004). We will make small changes on these tests since our grids are refined in South Hemisphere and we wish to investigate the impact of the refined region. Recently, a new test has been proposed by Shamir *et al.* (2019) and this test will also be included in our tests. Summarizing, our test set consist of:

1. Global steady geostrophic flow (test case 2 from Will92);

2. Flow over a mountain (test case 5 from Will92);

3. Rossby-Haurwitz wave (test case 6 from Will92);

4. Matsuno baroclinic wave (Shamir *et al.*, 2019);

5. Barotropic unstable zonal jet with perturbation (Galewsky *et al.*, 2004).

We also will analyse the discrete operator's convergence in a similar way as Peixoto (2016). We change test case 5 from Will92 by replacing the mountain by a smooth Andes topography. The barotropic unstable jet is changed by defining the jet on the Southern Hemisphere rather than the Northern Hemisphere, as it is originally proposed in Galewsky *et al.* (2004) and usually presented in the literature.

There are only a few papers on literature that have investigated the solution of the shallow water equations using TRSK on SCVT grids with local refinement. For instance, Ringler *et al.* (2011) analyses TRSK on a SCVT grids with local refinement similar to the grid presented in Figure 2.3. The only difference is that their grids refines North America instead of South America. This work analyses grids with ×2, ×4, ×8 and ×16 higher resolution in North America. They conclude that all conservation properties are maintained for all grids. Also, geostrophic balance is maintained for all grids. For test case 2 (Will92) and unstable zonal jet, the error is dominated by the coarser grid resolution region. They run these tests for 12 and 6 days, respectively. They also find that for test case 5, the method converges with order 1.5, with respect to the coarser region resolution. In Liu e Yang (2017), they run test case 2 for 365 days using the MPAS model on similar grids to the ones shown in Ringler *et al.* (2011). They concluded that the geostrophic balance is maintained for this period. Also, this work concludes that the impact of the width of the transition

zone between coarse and fine resolution regions is negligible. The analysis of Ringler *et al.* (2011) were extended a full 3D model in Skamarock *et al.* (2012). Their results also show no problem with the transition zone.

Our analysis will contemplate more tests and propose grids with refinement based on topography, aiming to better represent the Andes mountain and the South American continent, instead of the grids presented in works mentioned in the previous paragraph.

4.1   Global steady geostrophic flow

This is test case 2 from Will92. Initial conditions are defined as:

$$h = h_0 - \frac{1}{g}\left(a\Omega u_0 + \frac{u_0^2}{2}\right)\sin^2\phi, \tag{4.1}$$

$$u = u_0\cos\phi, \tag{4.2}$$

$$v = 0. \tag{4.3}$$

The functions defined above satisfy the non-linear shallow water equations. Therefore, the initial condition is a solution that does not depend on time. Hence, the solution should remain constant for all time. We set the parameters $h_0 = 3 \times 10^3$ and $u_0 = \frac{2\pi a}{12\text{days}}$.

As suggested in Will92, in order to asses our results we consider the following operator I:

$$I(h) = \int_0^{2\pi}\int_{-\frac{\pi}{2}}^{\frac{\pi}{2}} h(\lambda,\phi)\cos\phi d\phi d\lambda. \tag{4.4}$$

$$\tag{4.5}$$

Then, we define the relative errors in norm 2 and maximum norm, respectively:

$$l_2(h) = \sqrt{\frac{I((h - h_{ref})^2)}{I(h_{ref}^2)}} \;, \tag{4.6}$$

$$l_\infty(h) = \frac{\max_i |h - h_{ref}|}{\max_i |h_{ref}|} \;, \tag{4.7}$$

$$\tag{4.8}$$

where h is thought as an estimated field and h_{ref} is the analytical solution. The definition of these errors for the normal component of velocity $\mathbf{u}$ is straightforward.

We ran this test for 30 days for a uniform resolution SCVT grid and on a grid with $3\times$ higher resolution on the Andes mountain (Figure 2.11). The grid level was set equal to 6 in both cases. We included the uniform grid in our analysis in order to investigate the impact of the refinement in the solution behaviour. In Figure 4.1, we show the error evolution for the field h and in Figure 4.2, we show the error evolution for the normal velocity $\mathbf{u}$. The error for h remains oscillating up to day 20, then it grows. The error for $\mathbf{u}$ starts to increase after day 5. In Figures 4.3 and 4.4 we show the errors for each cell at days 1 and 28, respectively. At day one the error is more concentrated over some cells. Actually, as we shall see later, these cells are the most unaligned cells (Figure 4.10). After 23 days, the error seems to be concentrated in one cell near to Andes region. After that, this cell error triggers gravity waves, as we can see on day 28.
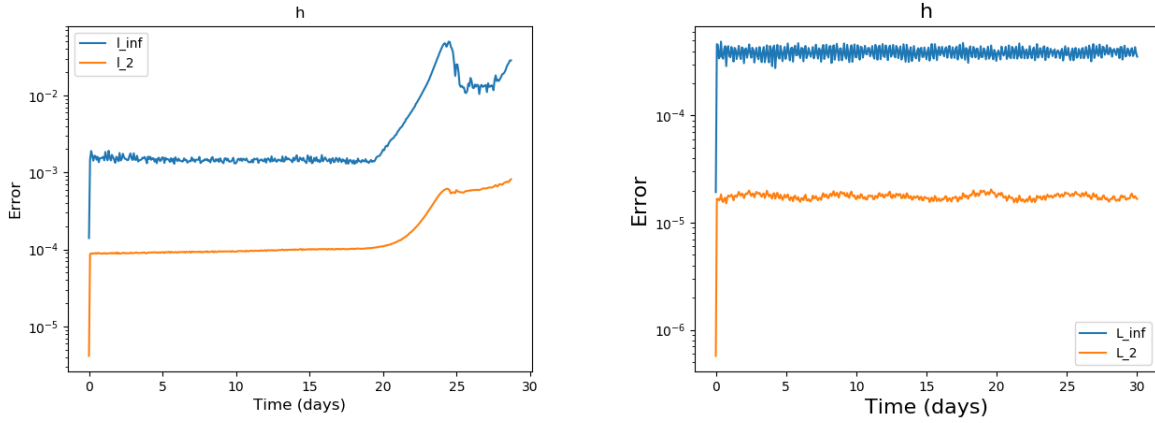
Figure 4.1: *Test case 2: Height field relative errors time evolution for refined SCVT (left) and uniform SCVT (right).*
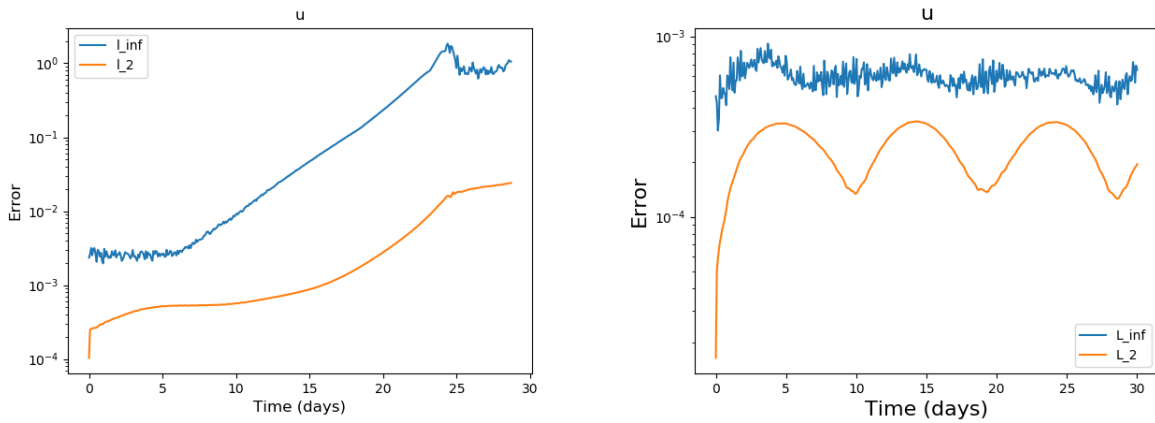

Figure 4.2: *Test case 2: Velocity normal component relative errors time evolution for refined SCVT(left) and uniform SCVT (right).*
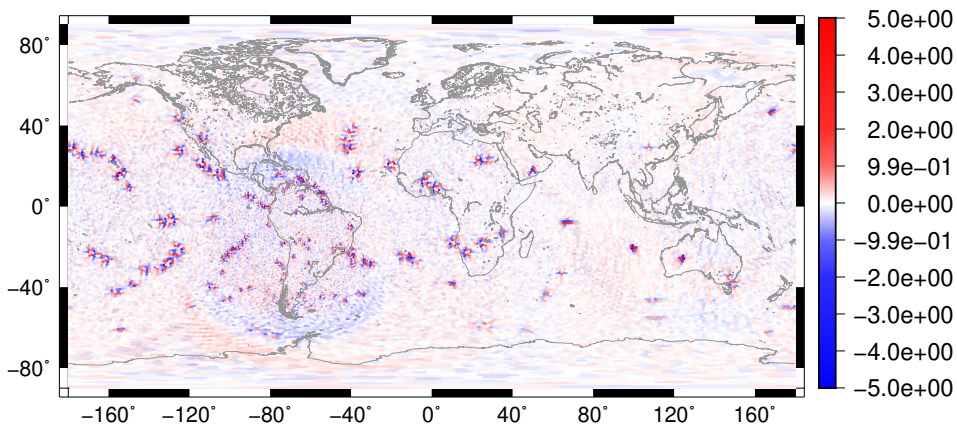

Figure 4.3: *Test case 2: Height field error distribution at day 1 considering a grid with local refinement on the Andes and 40962 grid generators.*
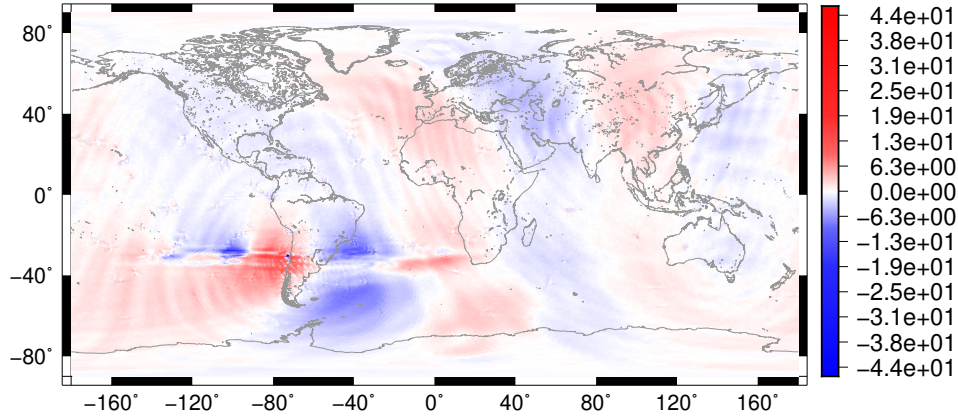
Figure 4.4: *Test case 2: Height field error distribution at day 28 considering a grid with local refinement on the Andes and 40962 grid generators.*

In order to analyze what is causing this behavior, we illustrate in Figures 4.5 and 4.6 the error evolution for each discrete operator. We notice that the discrete kinetic energy gradient starts with a large relative error in the maximum norm when compared to other operators. We observe this behavior in both uniform and refined grid. However, in the uniform grid, this large relative error does not impact in convergence, as we can see in Figure 4.1 and 4.2. The operator's errors in the uniform grid oscillate; in the refined grid, they increase. Both discrete gradients of kinetic energy and total fluid depth increase only after approximately 14 days on the refined grid. The discrete perpendicular term increases since day 0.
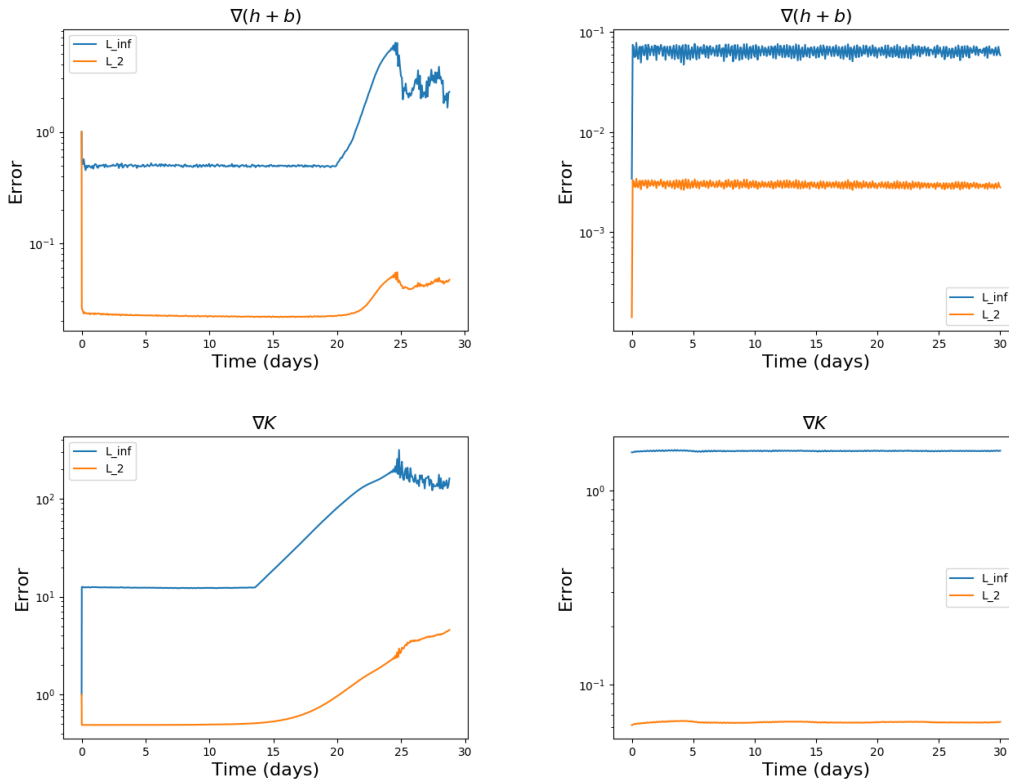
Figure 4.5: *Test case 2: Relative error time evolution for discrete version of the operators $\nabla(h + b)$ and ∇K in refined (left) and uniform (right) SCVT grids. The grid has 40962 grid generators.*
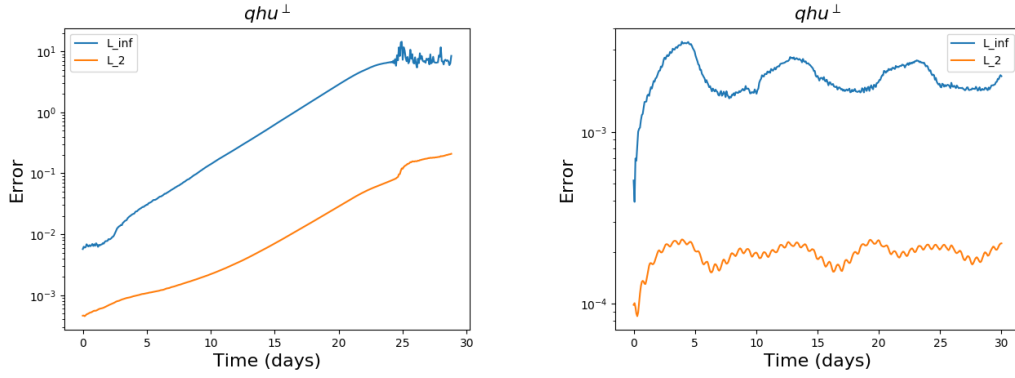
Figure 4.6: *Test case 2: Relative error evolution for discrete version of the operator qhu$^\perp$ in refined (left) and uniform (right) SCVT grids. The grid has 40962 grid generators.*

In Figure 4.7 we show the gradient of the Bernoulli potential and the perpendicular term error at day 26. From Figure 4.5 it is clear that the gradient term is being dominated by numerical noise in the Andes region, which is clearly a nonphysical behaviour. This leads to a very inaccurate representation of the Bernoulli potential gradient. The perpendicular term is less affected by the refined region, which is expected by the error evolution of perpendicular term showed in Figure 4.6.

Although the errors for the height field showed in Figure 4.3 are not too large, other diagnostic variables might be affected by the errors in the refined region that we showed here. For instance, in Figure 4.8 we show the potential vorticity at day 23. The pattern showed is the same as the ones showed in the discrete operators.
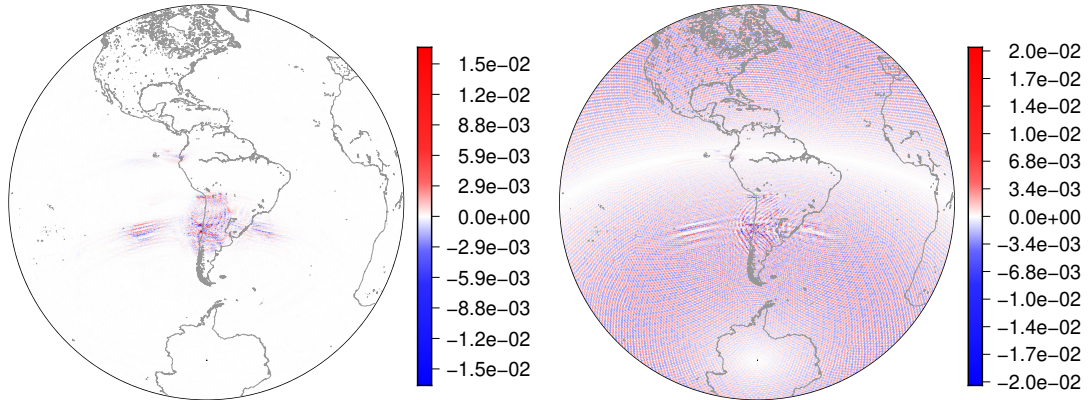
Figure 4.7: *Test case 2: Discrete Bernoulli potential gradient (left) and the perpendicular term (right) in the refined SCVT grids at day 26.*
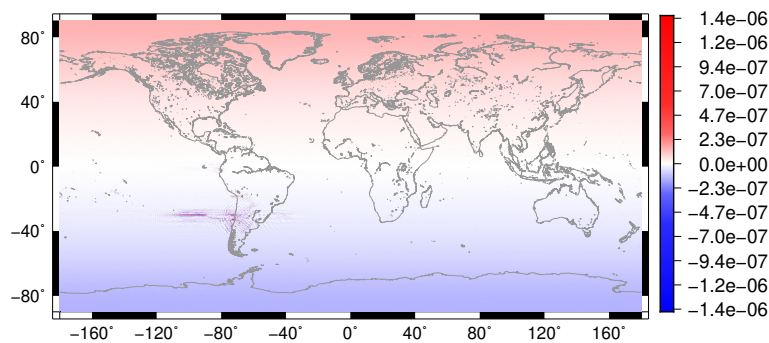
Figure 4.8: *Test case 2: Potential vorticity in the refined SCVT grid at day 23.*

Similarly to Peixoto (2016), we analyze the truncation error of divergence, perpendicular term,

kinetic energy and its gradient. The results for the grids with local refinement are shown in Figure 4.9.

The gradient of $h + b$ reaches second order of converge and the relative vorticity and potential vorticity has first-order of convergence (not shown) as we pointed out in Section 3.2 of Chapter 3. The full perpendicular term also reaches first order convergence (Figure 4.9).

The Kinetic energy truncation error does not converge to zero and its gradient truncation error diverges. In Figure 4.10 we show the error of kinetic energy error for each cell. A similar graph may be obtained for the kinetic gradient error. Figure 4.10 also shows the alignment index for each cell and we can observe that exists a high correlation between the truncation error of the kinetic energy and its gradient. The divergence's lack of consistency is analyzed in Peixoto e Barros (2013). They show that the inconsistency is due to bad aligned grid cells. In aligned cells, the finite volume discretization of divergence reaches second-order convergence. Since there are only a few badly aligned cells (Figure 4.10), first-order convergence is attained in l_2 norm.

Similar results can be obtained for a uniform SCVT grid (not shown, see Peixoto (2016)). Therefore, the inconsistency is not the reason for lack of convergence for test case 2 in our Andes refined grid, since this test is convergent in a uniform SCVT grid even though there are inconsistent operators. However, we notice that the discrete kinetic gradient is more inaccurate in the refined grid than in the uniform grid. We also analyzed the test case 2 for a grid with $2\times$ refinement over Andes mountain and we obtained similar results. Finally, we state that mass is conserved with precision 10^{-14} and the energy is conserved with precision 10^{-9} for the simulations presented so far.
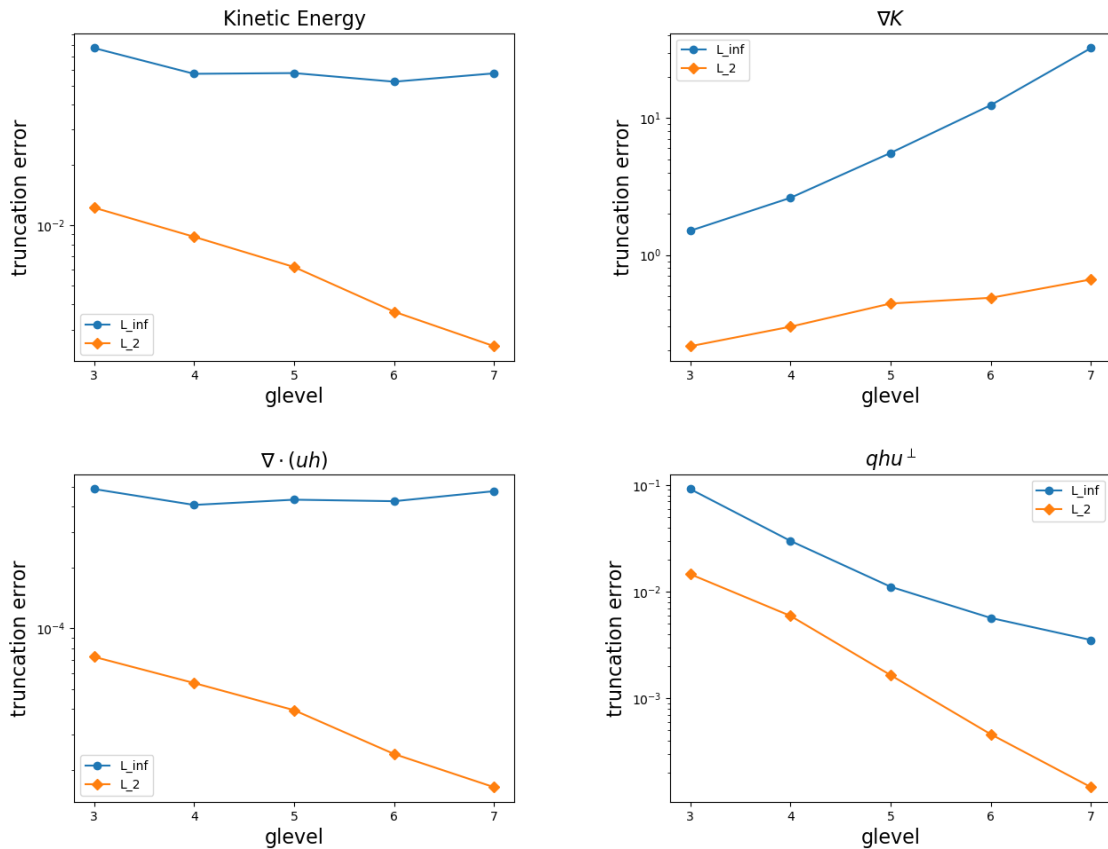
Figure 4.9: *Test case 2: Truncation error for discrete operators of K, ∇K, $\nabla \cdot (uh)$ and $qhu^{\perp}$ in refined grids for each grid level.*
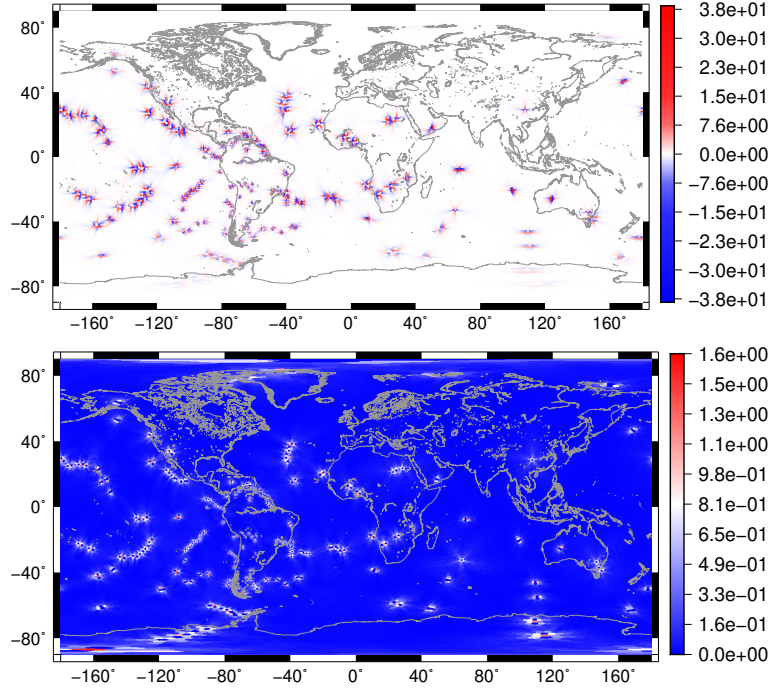
Figure 4.10: *Test case 2: Kinetic Energy truncation error (top) and alignment index (bottom) for Andes refined grid considering grid level equal to 6.*

Adding diffusion

In order to reduce the numerical noise from our simulations, we ran the same test case on the refined grid as before but adding a numerical diffusion in the discrete equations. We employed the following diffusion coefficient:

$$K = \frac{1}{\tau}\left(\frac{r^2}{n_0(n_0+1)}\right)^q,$$

where r denotes Earth radius, $n_0 = 85$, $\tau = 8$ hours and $q = 1$. For these parameters, we have $K \approx 8225.13$. This coefficient is used in spectral models (Jablonowski e Williamson, 2011) and will be used in our simulations. Figure 4.11 shows the error evolution for the height field and normal component of the velocity field. In contrast with Figures 4.1 and 4.2, we can notice that the error does not grow in any field. Figure 4.12 shows how the height field error is distributed. We can notice that the error is larger in bad aligned cells, similar to Figure 4.10. At last, from Figure 4.13 we can notice that the mass is conserved with precision 10^{-14}. However, the total energy is no longer conserved with machine precision as we obtained before in the simulation without diffusion.
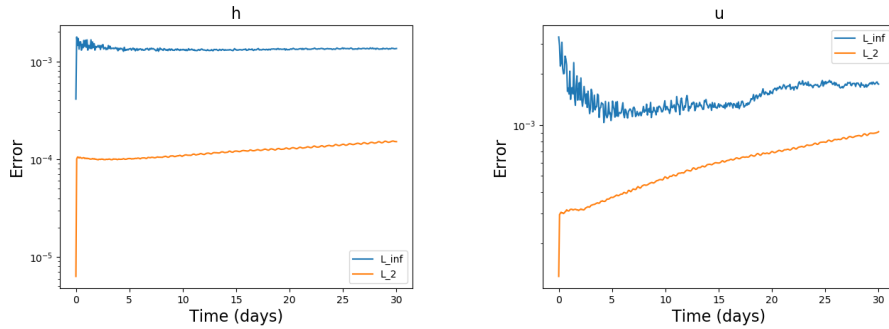
Figure 4.11: *Relative errors for height field (left) and velocity (right) evolution with time for test case 2 using numerical diffusion.*
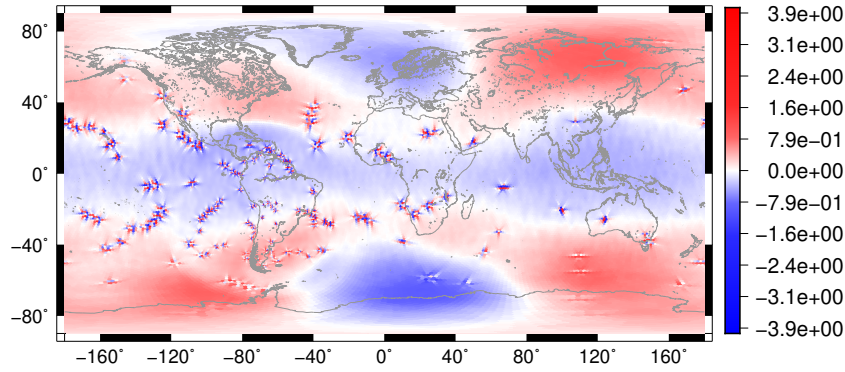
Figure 4.12: *Test case 2: Error distribution at day 30 for height field on grid with local refinement in Andes mountain and South American continent using numerical diffusion. We used a grid with 40962 generators.*
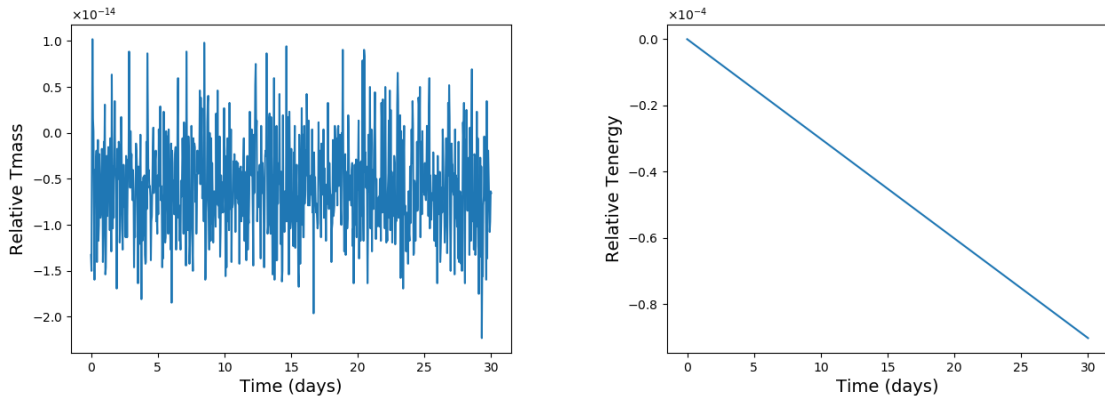

Figure 4.13: *Test case 2: Time evolution of relative change of total mass (left) and total energy (right). Diffusion was employed. We used a grid with 40962 generators.*

At last, we analyse the converge of the error when we increase the grid level. We compute the errors at day 10. The results are shown in Figure 4.14. For the height field, in both norms, the error decreases with order close second-order, then it gets close to first order and becomes stagnated for the l_∞ norm. For the velocity field, in both norms, the error converges to zero with almost second order from grid level 1 up to 6. From level 6 to 7 the errors decay with first-order. These results are in agreement with Ringler *et al.* (2010) and Peixoto (2016).
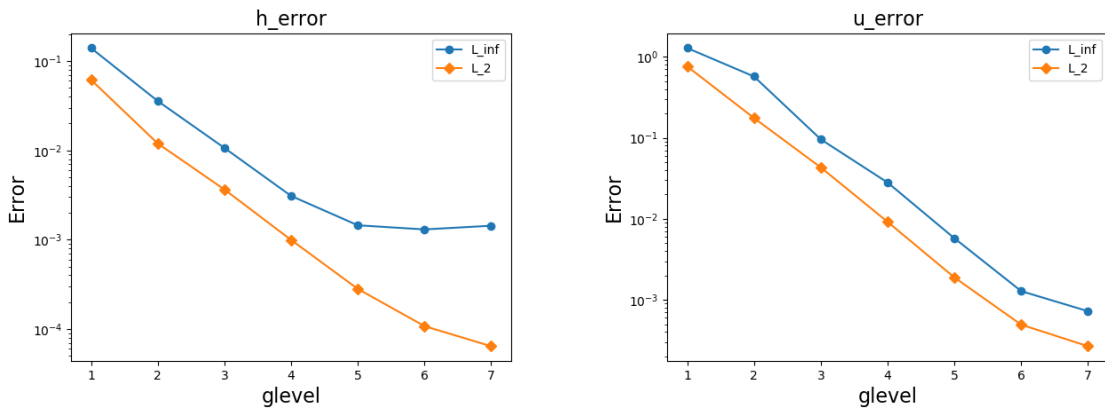
Figure 4.14: *Test case 2: Grid convergence analysis of h (left) and u (right) using numerical diffusion.*

4.2 Flow over Andes mountain

This test is proposed by Will92 by adding a mountain with a cosine shape in test case 2. We changed this test replacing the mountain by a smooth Andes topography in order to analyze the flow behaviour in the refined region. We ran this test for 30 days with the $3\times$ Andes refined grid with grid level equal to 7 (163842 nodes). We used the same topography data that we showed in Subsection 2.3. The mean height is set to $h_0 = 5400$ and the height field is given by:

$$h = h_0 - \frac{1}{g}\left(a\Omega u_0 + \frac{u_0^2}{2}\right)\sin^2\phi - b(\lambda, \phi), \tag{4.9}$$

where b is the smooth Andes topography data. Again, we apply linear interpolation in our topography data. The velocity field is the same given in test case 2.

This test case does not have an available analytical solution. As a reference solution, we use ENDGame (Thuburn *et al.*, 2010), a semi-Lagrangian shallow water model on a latitude-longitude C grid. We ran the test with a resolution of 720×1440 and applied cubic interpolation to estimate the velocity and height field at edges and Voronoi centers, respectively, using the latitude-longitude data from ENDGame.

In Figure 4.15 we show the solutions for the height field and its errors.
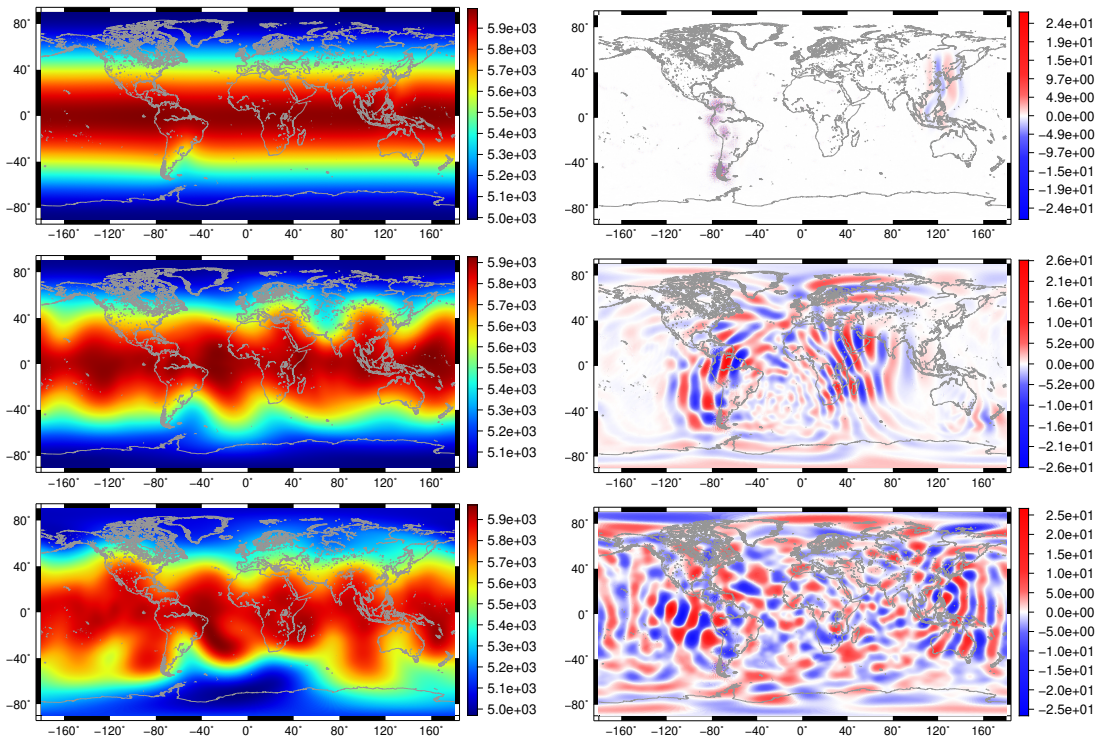
Figure 4.15: *Flow over Andes test case: Height field h (left) and height error (right) at days 1 (top), 15 (middle) and 30 (bottom) considering a grid with local refinement on Andes mountain and 163842 nodes.*

The initial error concentrates on Andes mountain and it is transported on the the grid. The height error behaviour is satisfactory as we can see in Figure 4.16, where we compare our solution with ENDGame's solution. The velocity field error grows after 23 days. At day 26, we can observe a numerical noise in potential vorticty in Africa, as it is show in Figure 4.17. This contrasts with test case 2, where numerical errors arose on refined region and not in the coarse region. The mass is conserved with precision 10^{-14} and the energy is conserved with precision 10^{-9}.
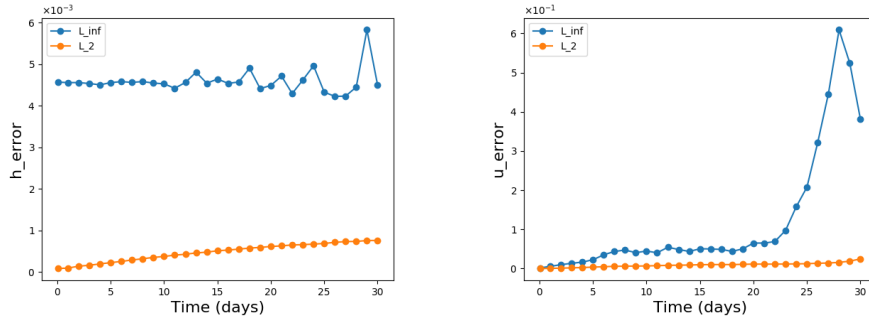
Figure 4.16: *Flow over Andes test case: Evolution of errors for h and u considering a grid with local refinement on Andes mountain and 163842 nodes - Reference solution is yielded by ENDGame*
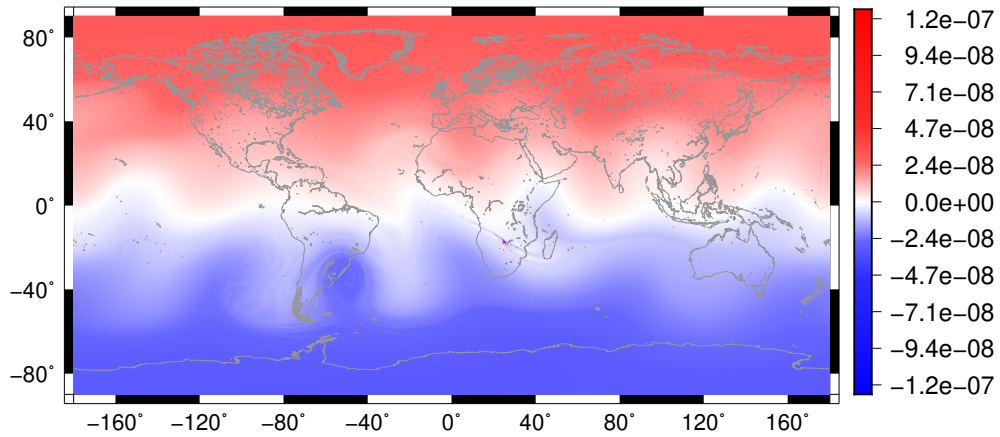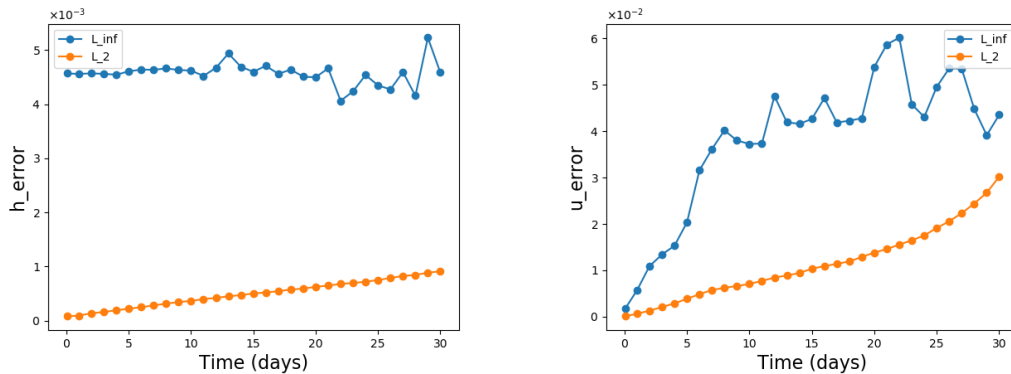

Figure 4.17: *Flow over Andes test case: Potential vorticity at day 26 considering a grid with local refinement on Andes mountain and 163842 nodes. Numerical noise appears in Africa.*

As we did in test case 2, we shall consider including a numerical diffusion in the momentum equation. In Figure 4.18 we show the results obtained. The error for the height field is lower than in the simulation without numerical diffusion. For the velocity field, we can notice an improvement in the error behaviour by adding diffusion. The velocity error does not increase as in Figure 4.16 and it is almost ten times lower at day 30. No numerical noise in the potential vorticity was observed (not shown). At last, the mass was conserved with precision 10^{-14} and the energy is conserved with precision 10^{-5} (Figure 4.19), which is worse than in the simulation without diffusion, as expected.

Figure 4.18: *Flow over Andes test case: Evolution of errors for h and u considering a grid with local refinement on Andes mountain and 163842 nodes. Numerical diffusion is employed in this simulation - Reference solution is yielded by ENDGame*
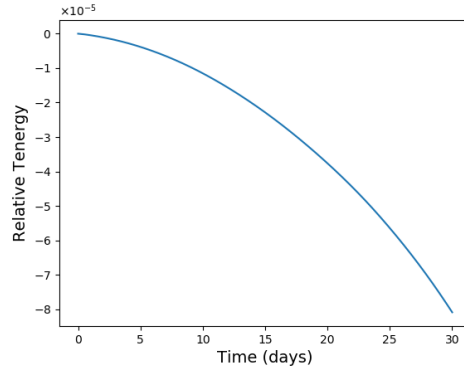
Figure 4.19: *Time evolution of relative change in total energy for Flow over Andes test case. Numerical diffusion is employed.*

4.3   Rossby-Haurwitz wave

This is the test case proposed in Will92. The height and velocity fields define an analytical solution of the nonlinear vorticity barotropic equation. It is recommended to set only the wave number 4 as an initial condition. The solution is expected to zonally propagate and keep its shape. However, Thuburn e Li (2000) has shown that the wave number 4 is unstable and even numerical errors can trigger the instability.

We ran the test for 30 days in the grid with $3\times$ higher resolution on Andes. The grid level was set equal to 6 (40962 nodes). After approximately 21 days, the wave starts to lose its shape.

In Figure 4.20 we show the errors evolution. The results show that the error is well behaved until the wave started to lose its shape. The loss of shape is not caused by the refined grid, since in uniform resolution the wave also loses its shape.

In Figure 4.21 we plot the error after 1 day. We can notice again that the error is dominated by the bad aligned cells showed in Figure 4.10. After the shape of the wave is lost, the solution won't make sense. However, after 30 days we can notice that a numerical noise appears near to Andes mountain, in both height field and vorticity field (Figure 4.22). Finally, mass and energy are conserved with precision 10^{-14} and 10^{-9} respectively (not shown).
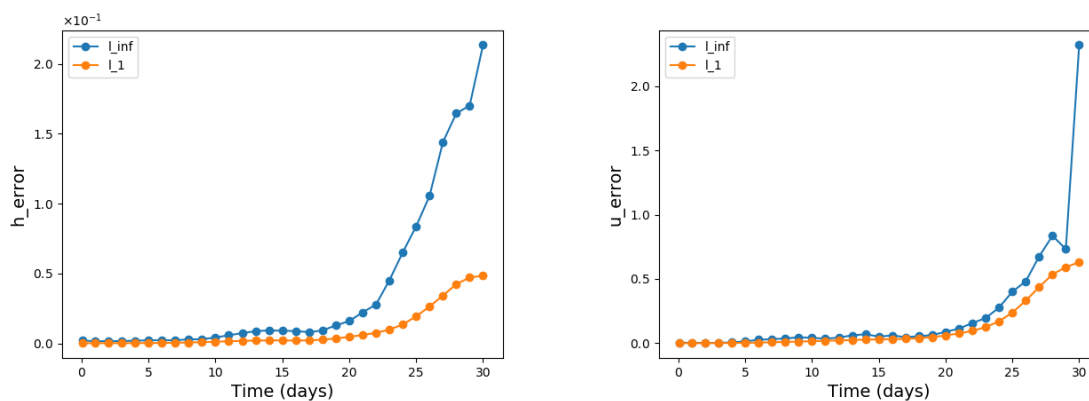

Figure 4.20: *Rossby-Haurwitz wave test case: Evolution of errors for h and u considering a grid with local refinement on Andes mountain and 40962 nodes - Reference solution is yielded by ENDGame.*
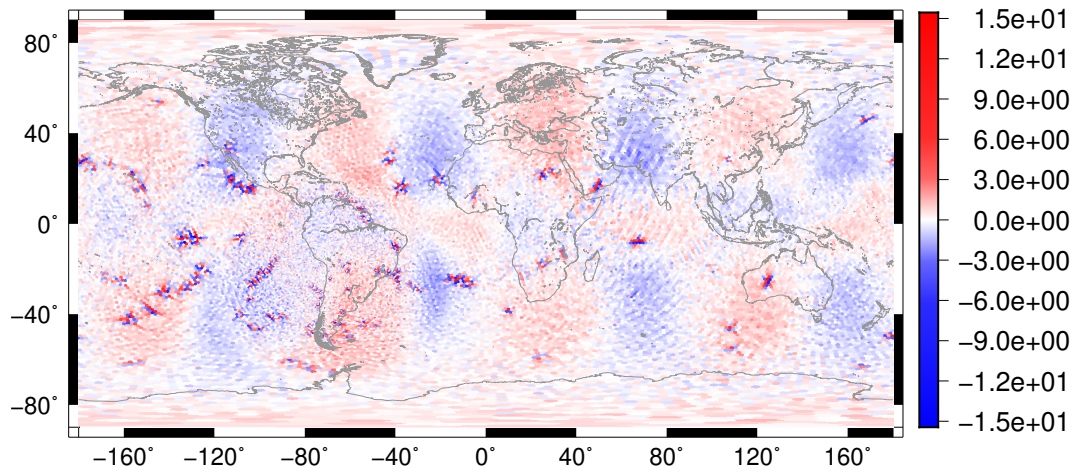
Figure 4.21: *Rossby-Haurwitz wave test case: Distribution of the errors for h after 1 day considering a grid with local refinement on Andes mountain and 40962 nodes.*
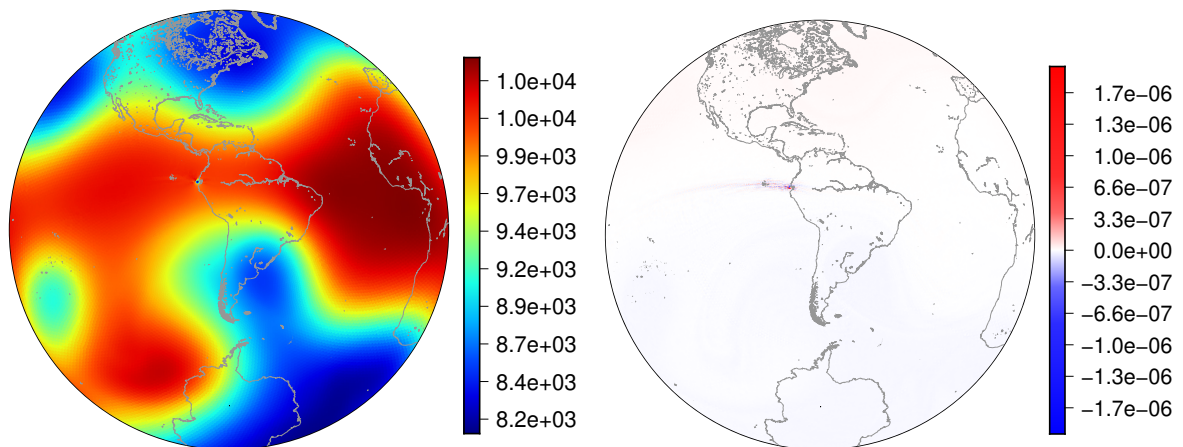

Figure 4.22: *Rossby-Haurwitz wave test case: Height field and potential vorticity at day 30.*

4.4   Matsuno baroclinic wave

The instability of Rossby-Haurwitz is undesirable since we cannot run this test for more than 20 days, because after that the wave loses the shape. A new test case has been recently proposed by Shamir et al. (2019), which is known as Matsuno baroclinic wave test case. In contrast with the Rossby-Haurwitz test case that uses analytical solutions of the nonlinear barotropic vorticity equation as initial conditions, this test case uses as initial conditions the analytic solution for the shallow water equations linearised on beta plane obtained by Matsuno (1966). The solution has the following form in planar geometry:

$$u(x, y, t) = \Re\big(\hat{u}(y)e^{i(kx - \omega t)}\big), \tag{4.10}$$

$$v(x, y, t) = \Re\big(\hat{v}(y)e^{i(kx - \omega t)}\big), \tag{4.11}$$

$$h(x, y, t) = \Re\big(\hat{h}(y)e^{i(kx - \omega t)}\big), \tag{4.12}$$

$$\tag{4.13}$$

where $\Re$ denotes the real part, k is the wavenumber and ω is the time-frequency. Therefore, the solutions are zonally propagating waves. Replacing this *ansatz* in the shallow water equations linearised on beta plane, we get a Schrodinger quantum harmonic equation that leads us to the following dispersion relation:

$$\omega_{n,k}^3 - \left(gHk^2 + \frac{2\Omega\sqrt{gH}(2n + 1)}{a}\right)\omega_{n,k} - \frac{2\Omega gHk}{a} = 0, \tag{4.14}$$

where $n = -1, 0, 1, \cdots$ and H is the mean fluid depth. As pointed out in Shamir et al. (2019), $n = -1$ gives one real root $\omega = k\sqrt{gH}$, which corresponds to a Kelvin wave. Setting $n = 0$ leads to a mixed Rossby-gravity wave, one eastward inertial gravity wave (hereafter EIGW) and one westward inertial gravity wave (hereafter WIGW). This last wave is nonphysical since it leads to infinite wind speed. Finally, $n \geq 1$ gives us three distinct real roots that correspond to a Rossby wave (hereafter RW), a EIGW and a WIGW. The solutions of Equation (4.14) are given by:

$$\omega_{n,k,j} = -\frac{1}{3}\Re\left(\Delta_j + \frac{\Delta_0}{\Delta_j}\right), \tag{4.15}$$

for $j = 1, 2$ and 3. The Δ_j can be computed as:

$$\Delta_0 = 3\left[gHk^2 + \frac{2\Omega\sqrt{gH}}{a}(2n + 1)\right], \tag{4.16}$$

$$\Delta_j = \left[\frac{\Delta_4 + \sqrt{\Delta_4^2 - 4\Delta_0^3}}{2}\right]^{\frac{1}{3}}\exp\left(\frac{2\pi j}{3}i\right), \tag{4.17}$$

$$\Delta_4 = -\frac{54\Omega gHk}{a}. \tag{4.18}$$

We have the following correspondence between the waves and frequency:

$$\text{RW} \iff \omega_{n,k} = -\min_{j=1,2,3}|\omega_{n,k,j}| \tag{4.19}$$

$$\text{WIGW} \iff \omega_{n,k} = \min_{j=1,2,3}\omega_{n,k,j} \tag{4.20}$$

$$\text{EIGW} \iff \omega_{n,k} = \max_{j=1,2,3}\omega_{n,k,j} \tag{4.21}$$

Finally, for given n and k, we can write the time frequency $\omega_{n,k}$ for each wave and get the amplitudes:

$$\hat{v}_n = A\hat{H}_n\left(\varepsilon^{\frac{1}{4}}\frac{y}{a}\right)\exp\left(-\frac{1}{2}\left(\varepsilon^{\frac{1}{4}}\frac{y}{a}\right)^2\right), \tag{4.22}$$

$$\hat{u}_{n,k} = \frac{gH\varepsilon^{\frac{1}{4}}}{ia(\omega_{n,k}^2 - gHk^2)}\left[-\sqrt{\frac{n+1}{2}}\left(\frac{\omega_{n,k}}{\sqrt{gH}}+k\right)\hat{v}_{n+1} - \sqrt{\frac{n}{2}}\left(\frac{\omega_{n,k}}{\sqrt{gH}}-k\right)\hat{v}_{n-1}\right], \tag{4.23}$$

$$\hat{h}_{n,k} = \frac{gH\varepsilon^{\frac{1}{4}}}{ia(\omega_{n,k}^2 - gHk^2)}\left[-\sqrt{\frac{n+1}{2}}\left(\omega_{n,k}+k\sqrt{gH}\right)\hat{v}_{n+1} + \sqrt{\frac{n}{2}}\left(\omega_{n,k}-k\sqrt{gH}\right)\hat{v}_{n-1}\right], \tag{4.24}$$

where $\hat{H}_n$ denotes the n-th normalized Hermite polynomial, A is the wave amplitude and $\varepsilon = \frac{(2\Omega a)^2}{gH}$ is the Lamb parameter.

These expressions describe the solution on Cartesian coordinates for the linearized shallow water equation on the equatorial beta plane. These solutions approach solutions for the shallow water equations on the sphere in the limit $\varepsilon \to \infty$. Hence since the earth radius a and the angular velocity Ω are fixed values, the Matsuno wave solutions are accurate on the sphere only for small values of gravity-wave velocity $\sqrt{gH}$. In order to write the solution in spherical coordinates, we replace x by $a\lambda$ and y by $a\phi$; the wavenumber k is replaced by the spherical wave number $\frac{k_s}{a}$.

The test case proposed by Shamir *et al.* (2019) is applicable for both planar and spherical shallow water equations. It is recommend to use the values $n = 1$, $k_s = 5$, $A = 10^{-5}$. As we mentioned before, for $n \geq 1$ we have three types of waves. It is suggested to test only the RW and EIGW in order to cover both longitude directions. The wave period is defined by $T = \frac{2\pi}{\omega}$ and it is given by $T = 18.5$ days for the RW is and $T = 1.9$ days for the EIGW. The time integration recommended is $100T$ for each wave.

Once we described the Matsuno baroclinic wave test case, let's present results obtained in the $3\times$ higher resolution on the Andes grid. In order to ensure that the whole wave will pass through the Andes region, we rotate our grid in 21 degrees in x-z plane. We ran the test using the parameters described before. We used a grid with 10242 nodes (glevel= 5) and 40962 (glevel= 6) for the RW and EIGW, respectively. In Figure 4.23, we show the initial condition and the diameters distribution of the rotated grid.
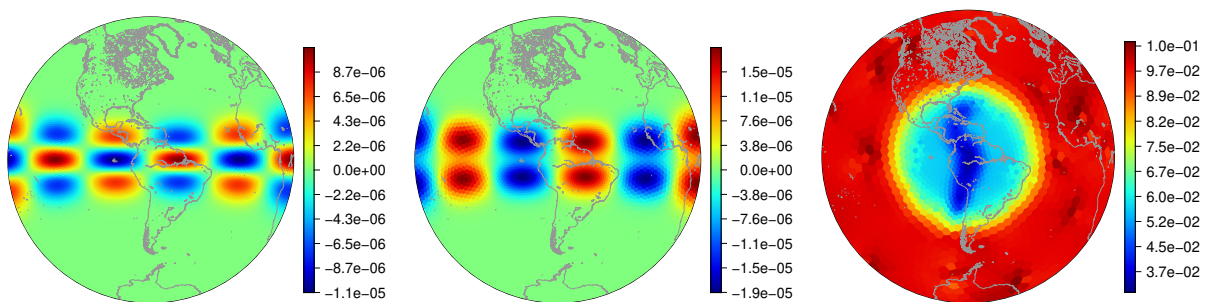

Figure 4.23: *Initial conditions for the RW and EIG (left and center) and diameters of the rotated grid (right).*

In Figures 4.24 and 4.25, we show our simulation results. A phase error is evident, which is not caused by the local refinement. Mass and energy are conserved with precision 10^{-14} (not shown). In contrast with the Rossby-Haurwitz wave, we can see that both RW and EIGW preserves its shape after 100 wave periods. In Shamir *et al.* (2019), a similar stability analysis as in Thuburn e Li (2000) is made in order to investigate wave stability. Both RW and EIGW shows to be stable.

An assessment criteria for the Matsuno baroclinic wave test case suggested by Shamir *et al.* (2019) is the Hovmoller diagram. We analyse one time-longitude diagram and one time-latitude diagram. The time-longitude diagram is obtained by writing the values of the field that we wish

to plot for a fixed latitude for each time. Since the wave propagates only in the zonal direction, we expect that the time-longitude diagram consists of straight lines with slope $\frac{k}{\omega}$. Similarly, the time-latitude diagram of a field is obtained by writing its values for a fixed longitude. Similarly, the time-latitude diagram of a field is obtained by writing its values for a fixed longitude. In Figures 4.26 - 4.31 we show the diagrams for the EIGW and the RW, respectively. The time interval is the last wave period, i.e., we consider only $99T \le t \le 100T$.
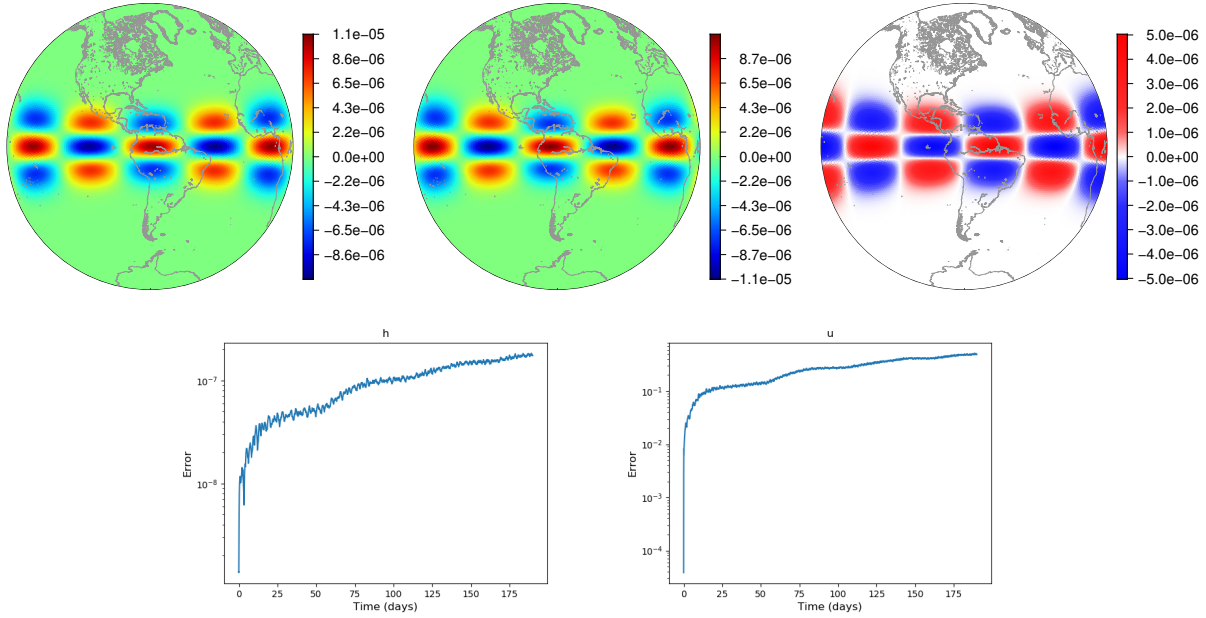
Figure 4.24: *EIGW: Height field (left, top), exact solution (center, top) and error (right, top) after 100 wave periods. Error time evolution for h (left, bottom) and u (right, bottom) in maximum norm.*
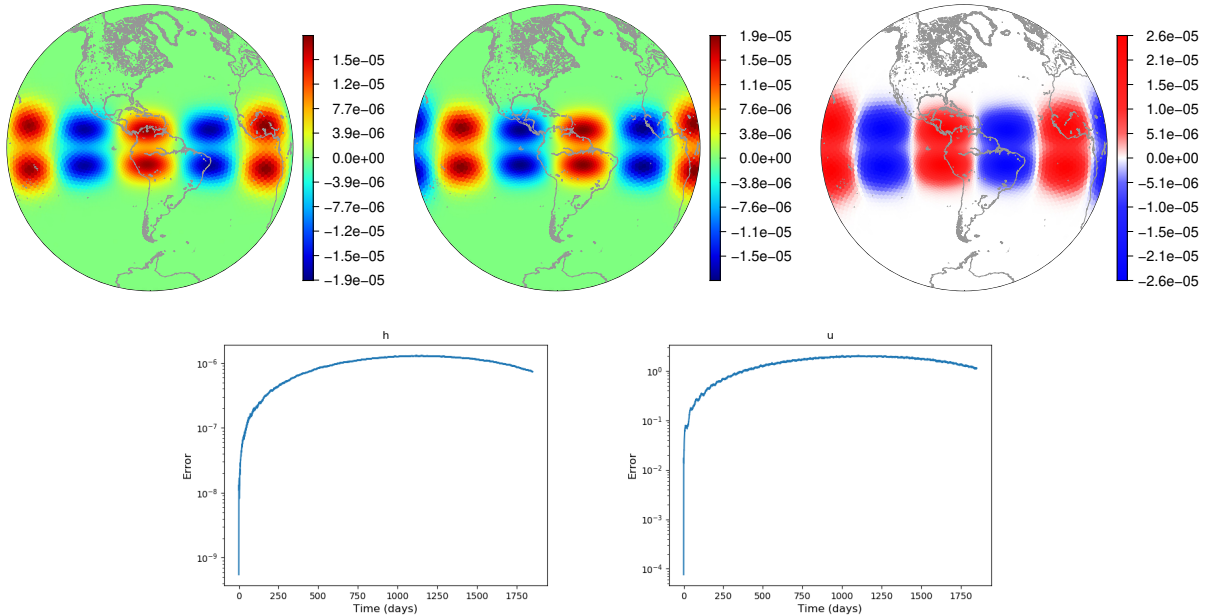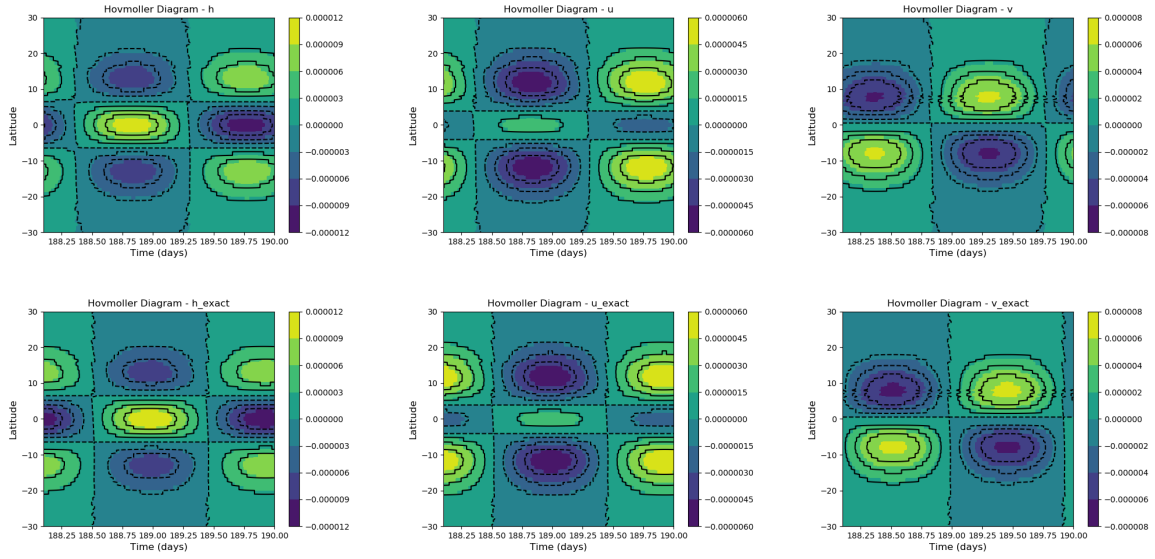

Figure 4.25: *RW: Height field (left, top), exact solution (center, top) and error (right, top) after 100 wave periods. Error time evolution for h (left, bottom) and u (right, bottom) in maximum norm.*

Figure 4.26: *EIGW: Time-latitude Hovmoller diagrams for EIG for h, u and v (top) and for analytic solutions of h, u and v (bottom). The longitude is fixed at $\lambda = -18$ degrees. The time values showed is the interval $99T \leq t \leq 100T$.*
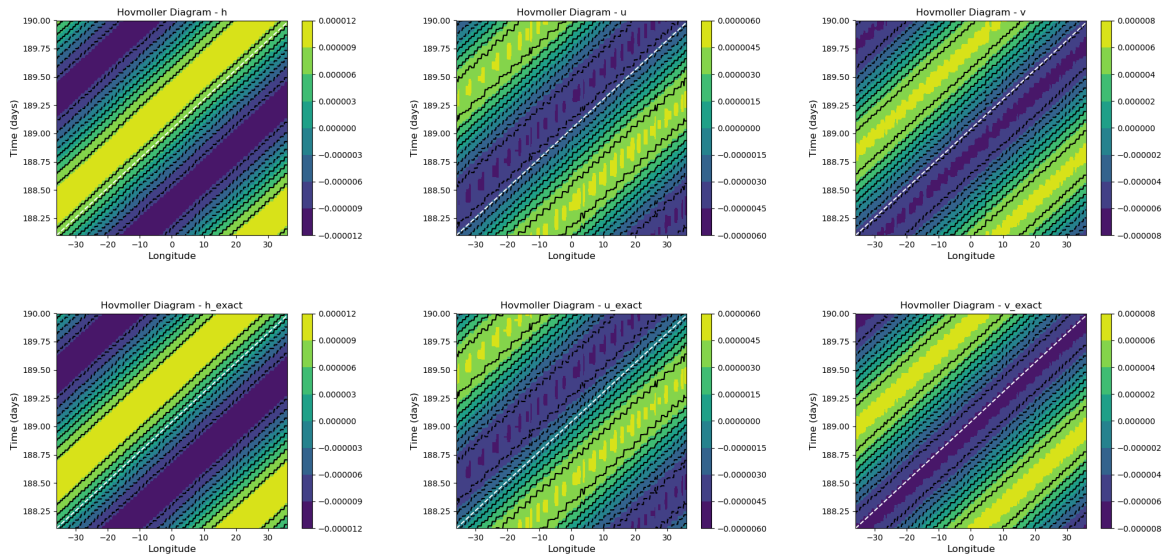

Figure 4.27: *EIGW: Time-longitude Hovmoller diagrams for EIG for h, u and v (top) and for analytical solutions of h, u and v (bottom). The latitude is fixed at $\phi = 9$ degrees except for u where we use $\phi = 0$ degrees. The time values showed is the interval $99T \leq t \leq 100T$. White dashed line is a line with slope $\frac{k}{\omega}$.*
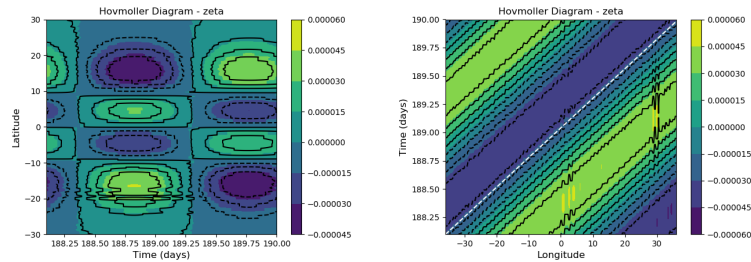

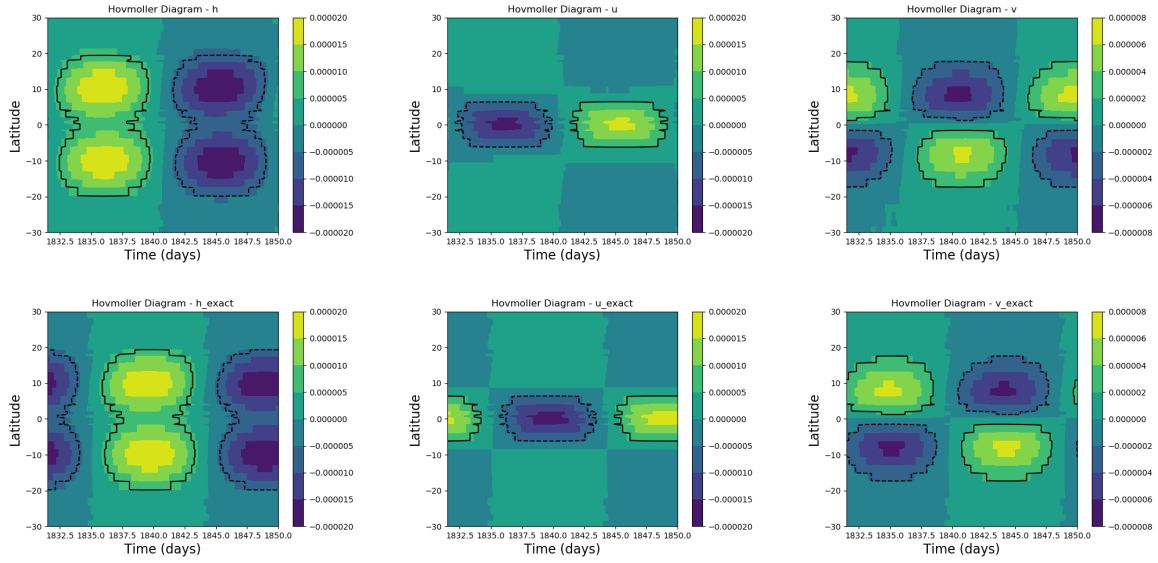**Figure 4.28:** *EIGW: Relative vorticity latitude and longitude Hovmoller diagrams.*

Figure 4.29: *RW: Time-latitude Hovmoller diagrams for EIG for h, u and v (top) and for analytical solutions of h, u and v (bottom). The longitude is fixed at $\lambda = -18$ degrees. The time values showed is the interval $99T \le t \le 100T$.*
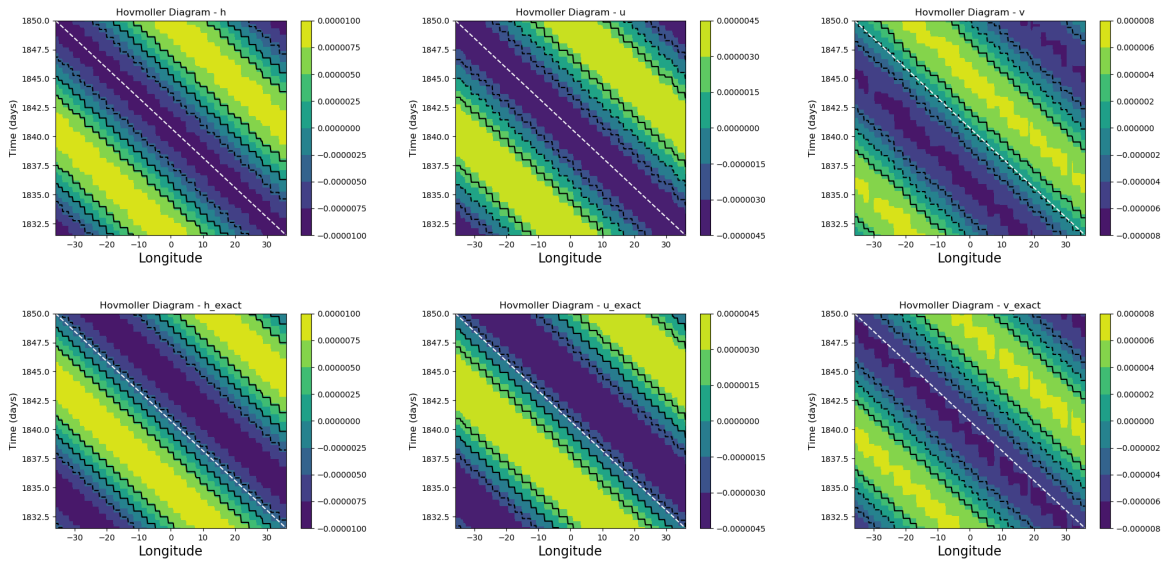

Figure 4.30: *RW: Time-longitude Hovmoller diagrams for EIG for h, u and v (top) and for analytical solutions of h, u and v (bottom). he latitude is fixed at $\phi = 9$ degrees except for u where we use $\phi = 0$ degrees. The time values showed is the interval $99T \le t \le 100T$. White dashed line is a line with slope $\frac{k}{\omega}$.*
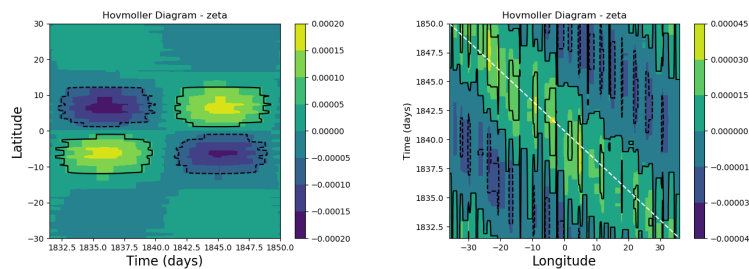

Figure 4.31: *RW: Relative vorticity latitude and longitude Hovmoller diagrams.*

The time-latitude Hovmoller diagrams 4.26 and 4.29 for the velocities and height show the phase error as we mentioned before. From the longitude-time Hovmoller diagrams 4.27 and 4.30, we can conclude that the fields are propagating with the correct speed. This is clear when we compare the black lines with the dashed white line in Figures 4.27 and 4.30. The results for the velocity field and height field show the same behaviour of the same analytic solution. However, the relative vorticity diagrams 4.28 and 4.31 shows some numerical noise, which is more evident in the RW diagram. This numerical noise does not appear in relative vorticity graphs, it is only present in Hovmoller diagrams.

4.5   Barotropically unstable jet with perturbation

This test case proposed by Galewsky *et al.* (2004) defines a zonal velocity field and with a height field such that they are in balance. The velocity and the height fields are given by, respectively:

$$u(\phi) = \begin{cases} 0, & \text{if } \phi \leq \phi_0, \\ \frac{u_{max}}{e_n} \exp\left[\frac{1}{(\phi-\phi_0)(\phi-\phi_1)}\right], & \text{if } \phi_0 < \phi < \phi_1, \\ 0, & \text{if } \phi \geq \phi_1, \end{cases} \tag{4.25}$$

$$h(\phi) = h_0 - \frac{1}{g}\int^{\phi} au(\phi')\left[f + \frac{\tan(\phi')}{a}u(\phi')\right]d\phi', \tag{4.26}$$

We define the parameters $\phi_0 = -5°$, $\phi_1 = -45°$, $u_{max} = 80$ and $e_n = \exp\left[-\frac{4}{(\phi_1-\phi_0)^2}\right]$. In the literature the jet is usually defined in the Northern Hemisphere, however, the parameters ϕ_0 and ϕ_1 that we choose define the jet in the Southern Hemisphere so that we will analyse the jet on Andes.

We add the following perturbation in the height field:

$$\hat{h}(\lambda, \phi) = \hat{h}\cos(\phi)e^{-\left(\frac{\lambda}{\alpha}\right)^2}e^{-\left(\frac{\phi_2-\phi}{\beta}\right)^2}, \tag{4.27}$$

where $\hat{h} = 120\ m$, $\alpha = \frac{1}{3}$ $\beta = \frac{1}{15}$, $\phi_2 = -25°$. This perturbation triggers the barotropic instability. Actually, even numerical errors can trigger the instability because this test is unstable.

We ran this test in the $3\times$ higher Andes resolution grid with glevel = 7 for 15 days. We used again ENDGame as a reference solution. Mass and energy are conserved with precision 10^{-9} and 10^{-14}, respectively.

In Figure 4.32 we show the error evolution for the height and velocity field. In Figure 4.33 we illustrate the potential vorticity field for the refined and uniform grid. At day 6 we can see a numerical noise in the same region of Figures 4.7 and 4.8, which is transported with the flow, as it is shown in days 7 and 8. Again, we cannot notice any numerical noise in the height field.
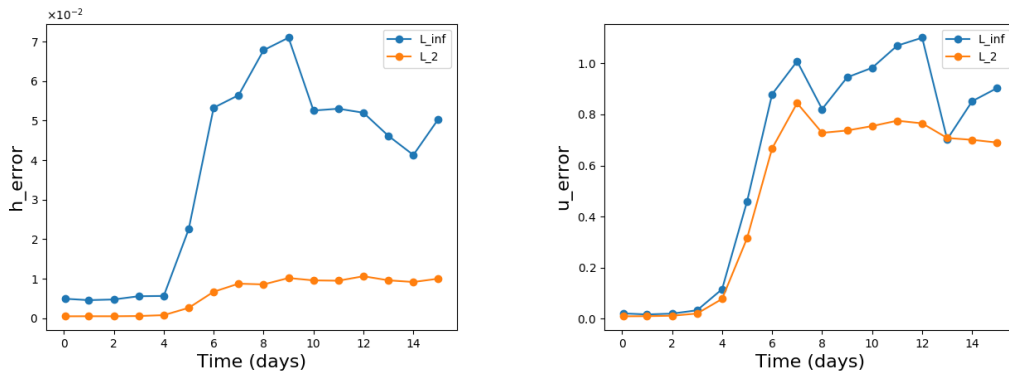

Figure 4.32: *Barotropically unstable jet test case: Error evolution for the height and normal velocity using a grid locally refined on Andes mountain and on South America continent with 163842 nodes.*
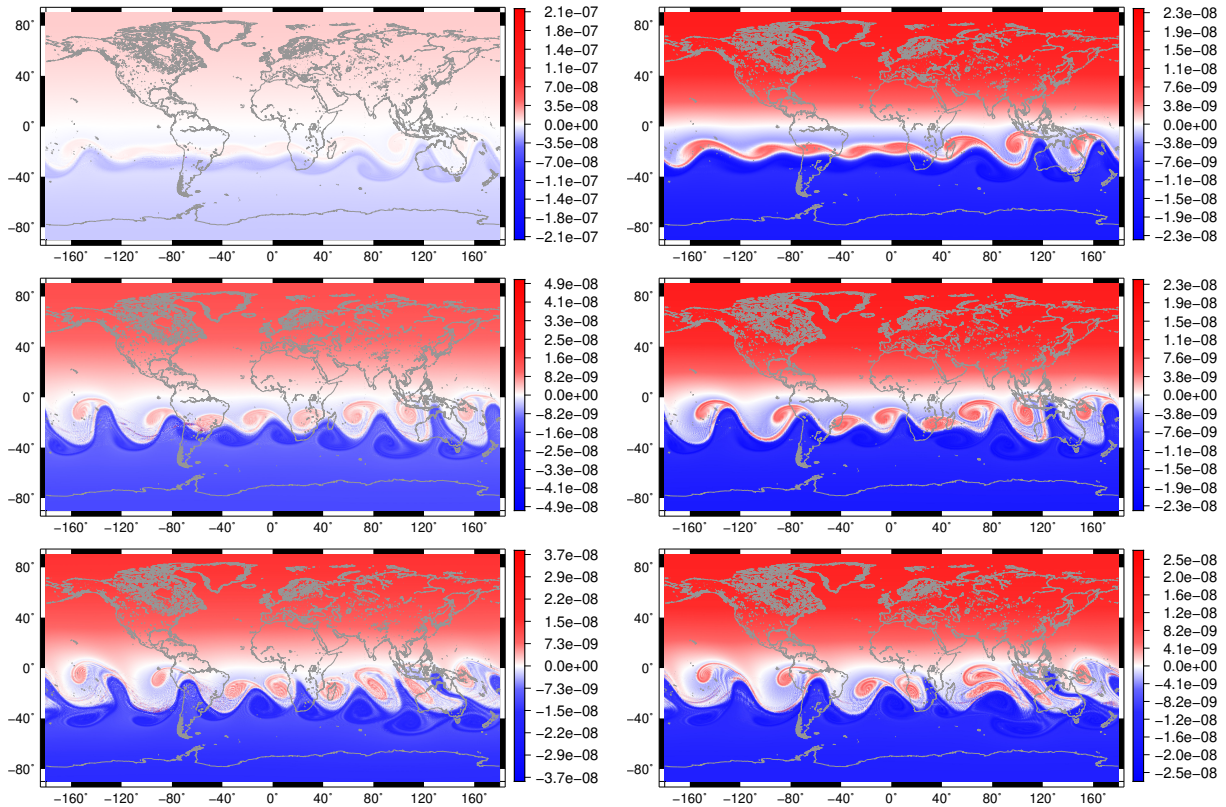
Figure 4.33: *Barotropically unstable jet test case: Potential vorticity at days 6 (top), 7 (middle) and 8 (bottom). The graphs on the left represent the results in the refined grid; the graphs on the right shows the results in the uniform resolution grid.*

In the same way as we did before in tests 2 and 5, we added a numerical diffusion in the momentum equation aiming to remove the numerical noises that we observed in the previous simulation. From Figure 4.34 we can notice that the diffusion performance is capable to remove the numerical noises from the potential vorticity. However, the errors obtained without diffusion (Figure 4.32) are similar to the errors obtained with diffusion (Figure 4.35). Similarly to the other simulations with numerical diffusion that we showed in this work, the total energy is no longer conserved (Figure 4.36).
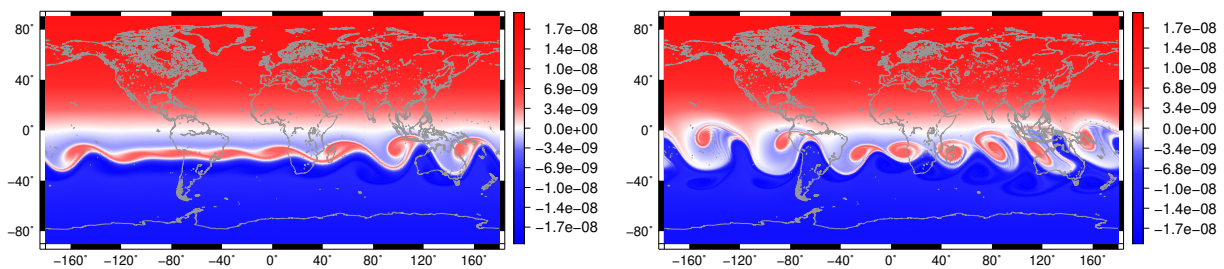

Figure 4.34: *Potential vorticity at days 6 (left) and 8 (right) for the barotropically unstable jet test case using the refined grid. Numerical diffusion was employed.*
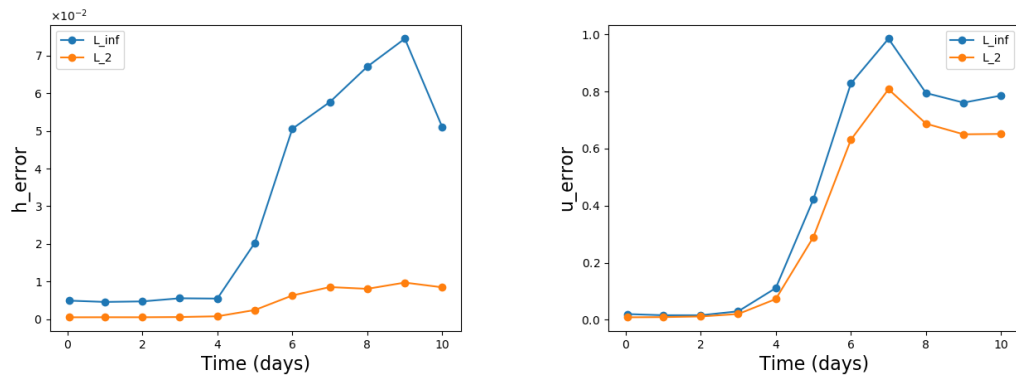
Figure 4.35: *Barotropically unstable jet test case: Error evolution for the height and normal velocity - with numerical diffusion.*
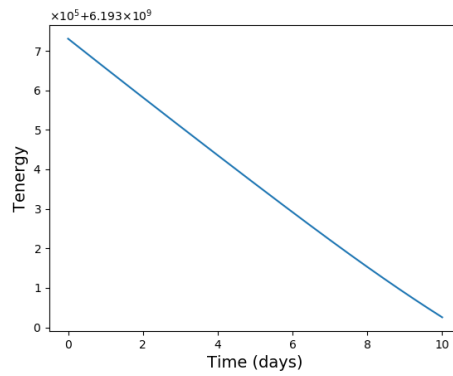

Figure 4.36: *Total energy evolution with time for the barotropically unstable jet test case with numerical diffusion.*

Chapter 5

Moist shallow water model

The shallow water equations have the advantage of representing key processes of the atmosphere and being less computationally expensive than the full 3D equations. Therefore they are usually used as an initial model in developing and assessing numerical methods for geophysical fluids. However, the shallow water equations lack of representing physical processes such as clouds, rain, convection, among others.

Some models have been developed using the shallow water model in order to study atmospheric processes. Wuersch e Craig (2014) has developed a model for cumulus convection and precipitation formation by modifying the one dimensional shallow water equations. This model has rain as one of its prognostic variables and the geopotential is modified when it exceeds a threshold in order to represent cumulus convection. Lahaye e Zeitlin (2016) has investigated the formation of hurricanes-like vortices using a model based on the rotating shallow water equations. Their model includes equations for humidity, condensation sink and evaporation source.

In this work, we implemented and analyze the moist Boussinesq shallow water model developed by Zerroukat e Allen (2015). This model is derived from the traditional Boussinesq approximation to the 3D Euler equations and allows the density to vary with temperature. The moisture variables are rain, vapour and clouds and these variables are advected as tracers. In Zerroukat e Allen (2015) they asses a semi-implicit semi-Lagrangian in this moist shallow water model. Ferguson *et al.* (2019) asses a high order finite volume method with adaptive moving mesh exploring the moist shallow water model developed by Zerroukat e Allen (2015). They showed that local refinement was able to solve local features.

In this chapter we will introduce the model developed by Zerroukat e Allen (2015) and discretizate the equations using TRSK on the grids with local refinement on Andes mountain developed in Section 2.3.

5.1 Description

The model developed by Zerroukat e Allen (2015) can be summarized in the following equations using the flux form for the advection equations:

$$\frac{\partial \mathbf{u}}{\partial t} + qh\mathbf{u}^{\perp} + \nabla B = S_u, \tag{5.1}$$

$$\frac{\partial h}{\partial t} + \nabla \cdot (h\mathbf{u}) = 0, \tag{5.2}$$

$$\frac{\partial h\theta}{\partial t} + \nabla \cdot (h\theta\mathbf{u}) = hS_\theta, \tag{5.3}$$

$$\frac{\partial hq^k}{\partial t} + \nabla \cdot (hq^k\mathbf{u}) = hS_q^k, \tag{5.4}$$

$$\tag{5.5}$$

where θ is the temperature, $k = 1, 2, 3$, $q^1 = q_v$ is the water vapour state, $q^2 = q_c$ is the cloud state, $q^3 = q_r$ is the rain state and finally $\mathbf{u}$ is the wind speed and h is the fluid depth, as in the standard shallow water model. The source for the momentum equation is given by:

$$S_u = g\theta\nabla b + \frac{1}{h}\nabla\Pi, \tag{5.6}$$

where b is the bottom topography and $\Pi = \frac{1}{2}h^2\theta$. The source of the advection equations defines a three-state moist physics.

The saturation function is given by:

$$q_{sat}(\theta) = \frac{q_0}{g(h+b)}\exp(20\theta). \tag{5.7}$$

The initial vapour state is given by:

$$q_{sat}(\lambda, \phi, 0) = G(\lambda, \phi)q_{sat}(\theta), \tag{5.8}$$

where q_0 is a constant chosen so that the initial maximum value of q_v is 0.02 and G is a function between 0 and 1 that defines how close q_v is from the saturation. After that, whenever $q_v > q_{sat}$ the excess value $q_v - q_{sat}$ is converted into cloud after being multiplied by a conversion rate $\gamma_v = \gamma_v(\theta)$ and the temperature is modified due to local heating effect. Summarizing, if $q_v > q_{sat}$, then:

$$
\begin{aligned}
C &= \gamma_v(q_v - q_{sat}), \\
q_v &\leftarrow q_v - C, \\
q_c &\leftarrow q_c + C, \\
\theta &\leftarrow \theta + LC,
\end{aligned}
$$

where $\gamma_v = (1 + L\frac{\partial q_{sat}}{\partial\theta})^{-1}$ and $L = 10$.

Whenever $q_v < q_{sat}$, a fraction of $q_{sat} - q_v$ is evaporated and the temperature is modified due to a cooling process. This phenomenon can be summarized as:

$$
\begin{aligned}
C &= \min\{q_c, \gamma_v(q_v - q_{sat})\}, \\
q_v &\leftarrow q_v - C, \\
q_c &\leftarrow q_c + C, \\
\theta &\leftarrow \theta + LC.
\end{aligned}
$$

Clouds are converted into rain whenever the q_c exceeds a threshold value of q_{precip}. In this case, a fraction of the excess value $q_c - q_{precip}$ is converted:

$$
\begin{aligned}
C &= \max\{0, \gamma_r(q_c - q_{precip})\}, \\
q_v &\leftarrow q_v - C, \\
q_c &\leftarrow q_c + C,
\end{aligned}
$$

where $\gamma_r = 10^{-3}$.

The processes described here can be summarized in the following equations (Zerroukat e Allen,

2015):

$$\Delta q_v = \max\{0, \gamma_v(q_v - q_{sat})\}/\Delta t,$$
$$\Delta q_c = \min\{q_c, \max\{0, \gamma_v(q_v - q_{sat})\}\}/\Delta t,$$
$$\Delta q_r = \max\{(0, \gamma_r(q_c - q_{precip})\}/\Delta t,$$
$$S_{q_v} = \Delta q_c - \Delta q_v,$$
$$S_{q_c} = \Delta q_v - \Delta q_c - \Delta q_r,$$
$$S_{q_r} = \Delta q_r,$$
$$S_\theta = L(\Delta q_v - \Delta q_c),$$

where Δt is the time step used in the numerical model. Notice that $S_{q_v} + S_{q_c} + S_{q_r} = 0$, therefore we can conclude that the integral of $h(q_v + q_c + q_r)$ is conserved in this model.

5.2   Discretization

Our variables are $\mathbf{u}$, h, $h\theta$ and hq^k. As in the shallow water model, we store h at Voronoi centers and the normal component of $\mathbf{u}$ is stored at the edges. The temperature and moisture variables $h\theta$ and hq^k are stored at Voronoi centers. Therefore, the terms in the advection equations for $h\theta$ and hq^k need to be computed at Voronoi centers. The divergence term may be calculated in the same manner as we did for the continuity equation (Equation (3.34)). The source terms for $h\theta$ and hq^k are straightforward to be computed since they depend only of θ and q^k, therefore we only need to divide these terms by h, which is easy to achieve since these variables are stored at the same position, so no interpolation is needed here.

The momentum equation in the moist shallow water model has a source term given by Equation (5.6) and this term needs to be evaluated at edges points. For the term $\theta \nabla b$, we first interpolate θ to the edges as follow:

$$\theta_e = \frac{1}{2} \sum_{i \in CE(e)} \theta_i \tag{5.9}$$

This interpolation is second order accurate. The gradient term ∇b is computed using second order finite differences as in (3.35),

$$[\nabla b]_e = -\frac{1}{d_e} \sum_{i \in CE(e)} b_i n_{e,i} \tag{5.10}$$

The term $\frac{1}{h}\nabla(h^2\theta)$ requires the value of h at the edges to compute $\frac{1}{h}$. This can be done through interpolation as in (5.9). The gradient $\nabla(h^2\theta)$ is computed as in (5.10) and no interpolation is required here since h and $h\theta$ are stored at Voronoi centers.

5.3   Test problems

This section is dedicated to present results of the moist shallow water model using TRSK on the grids with local refinement grid. We will present two test cases. These tests are similar to test cases 2 and 5 from Will92 and they are suggested in Zerroukat e Allen (2015). We will use a smooth Andes topography as a mountain in the second simulation.

5.3.1   Global steady geostrophic flow

This test initializes the fields with a time-independent analytical solution of the moist shallow water equations. As suggested in Zerroukat e Allen (2015), we computed the fields in a coordinate

system (λ', ϕ') which is obtained rotating 45 degrees the coordinate system (λ, ϕ). The initial fields are given by:

$$u(\lambda', \phi') = u_0 \cos \phi', \tag{5.11}$$

$$v(\lambda', \phi') = 0, \tag{5.12}$$

$$h(\lambda', \phi') = h_0 - \frac{1}{g}(\omega + \sigma) \sin^2 \phi', \tag{5.13}$$

$$b(\lambda', \phi') = 0, \tag{5.14}$$

$$\theta(\lambda', \phi') = \frac{\theta_0 + \sigma \cos^2 \phi'[(\omega + \sigma) \cos^2 \phi' + 2(\Phi_0 - \omega - \sigma)]}{\Phi_0^2 + (\omega + \sigma)^2 \sin^4 \phi' - 2\Phi_0(\omega + \sigma) \sin^2 \phi'}, \tag{5.15}$$

$$q_v(\lambda', \phi') = q_{sat}(b, h_0, \theta_0), \tag{5.16}$$

$$q_c(\lambda', \phi') = 0, \tag{5.17}$$

$$q_r(\lambda', \phi') = 0, \tag{5.18}$$

$$\tag{5.19}$$

where the parameters are set as $u_0 = 20$, $\omega = \left(\Omega a u_0 + \frac{u_0^2}{2}\right)$, $\sigma = \omega/10$, $\Phi_0 = 3 \times 10^4$, $h_0 = \Phi_0/g$, $\theta_0 = \varepsilon \Phi_0^2$ and $\varepsilon = \frac{1}{300}$. In Figure 5.1 we show the initial fields.
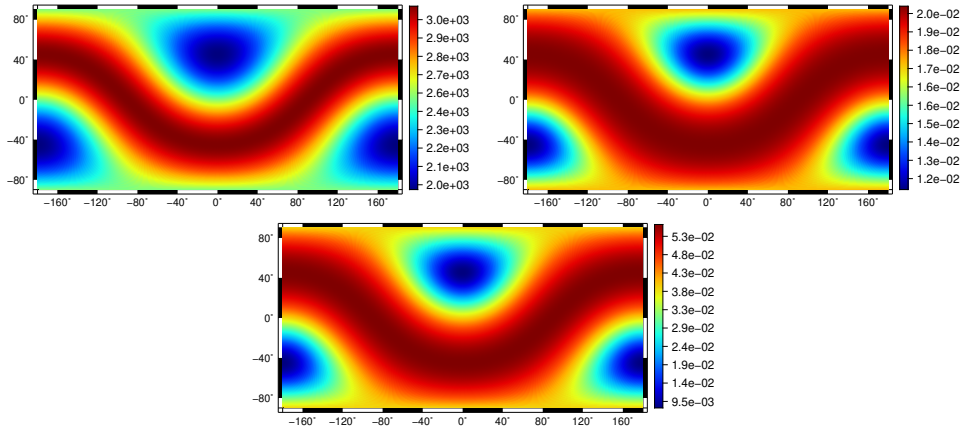

Figure 5.1: *Initial fields: height (top, left), vapour (top, right) and temperature (bottom) for the steady geostrophic flow for the moist shallow water model.*

We ran this test on a uniform SCVT grid and on the grid with resolution 3× higher on Andes mountain. The grid level was set equal to 6 and we ran the test for 30 days. In Figure 5.2 we show the error evolution for the fields. No rain is generated, which agrees with the analytical solution. However, clouds are created due to numerical errors. In Figure 5.3 we show the errors of the fields for both grids after 30 days. We can notice that the rain generated is due to grid imprinting errors. Even though clouds are being generated, they are not big enough in magnitude to generate rain. From Figure 5.2 we can notice that the errors remain stable, except the error of the velocity field that increases with time. This behaviour was observed in the shallow water model tests. However, no numerical noise was found neither in potential vorticity nor in height field, as we observed in the shallow water model tests with no diffusion. In Figure 5.4 we show how the total of water, given by the integral of $h(q_v + q_c + q_r)$, evolves with time. We can notice that this quantity is conserved as expected.
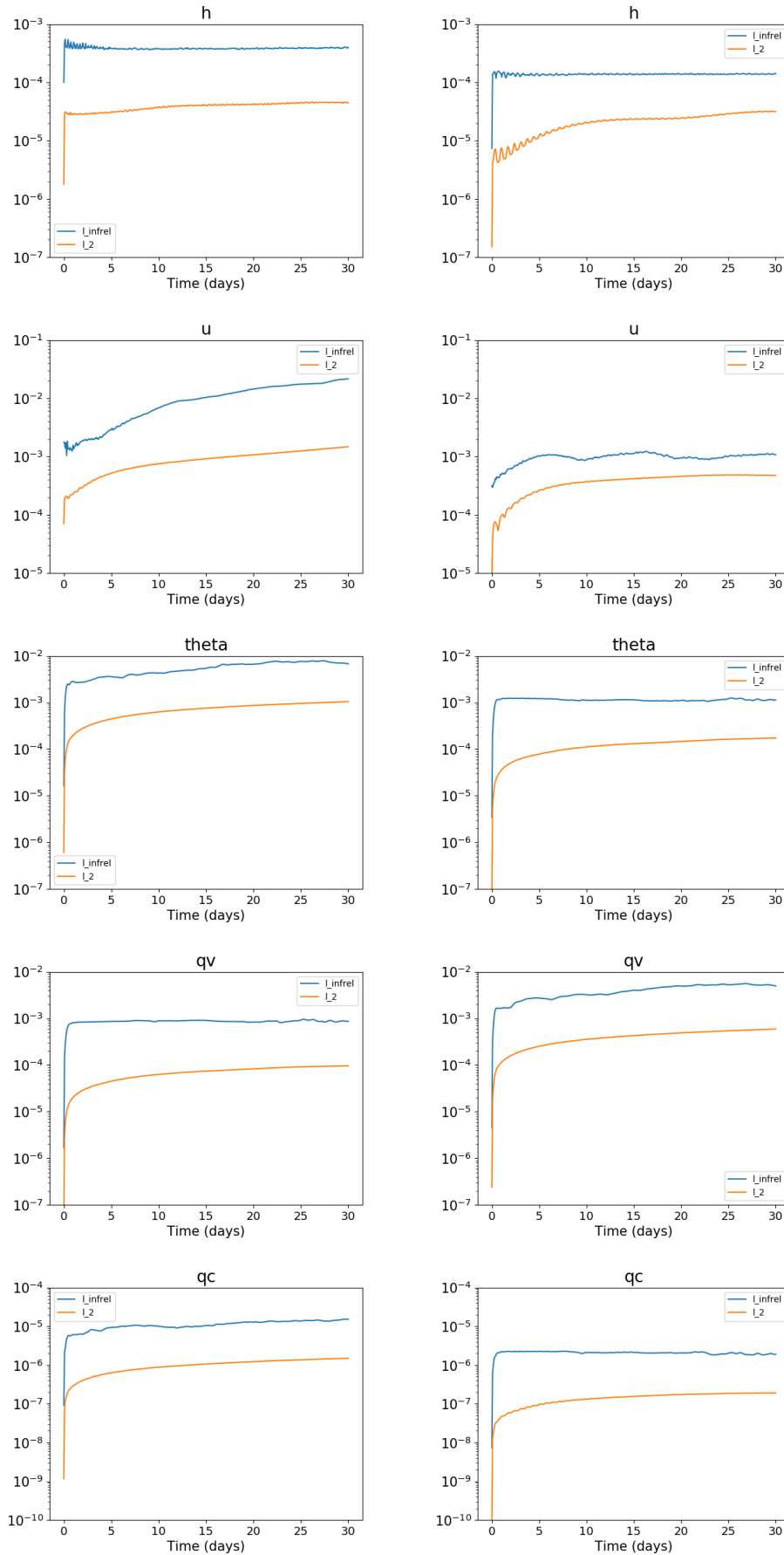
Figure 5.2: *Error evolution of height, velocity, vapour and cloud for steady geostrophic flow on refined grid (left) and uniform grid (right). Both grids are set in level 6 (40962 nodes).*
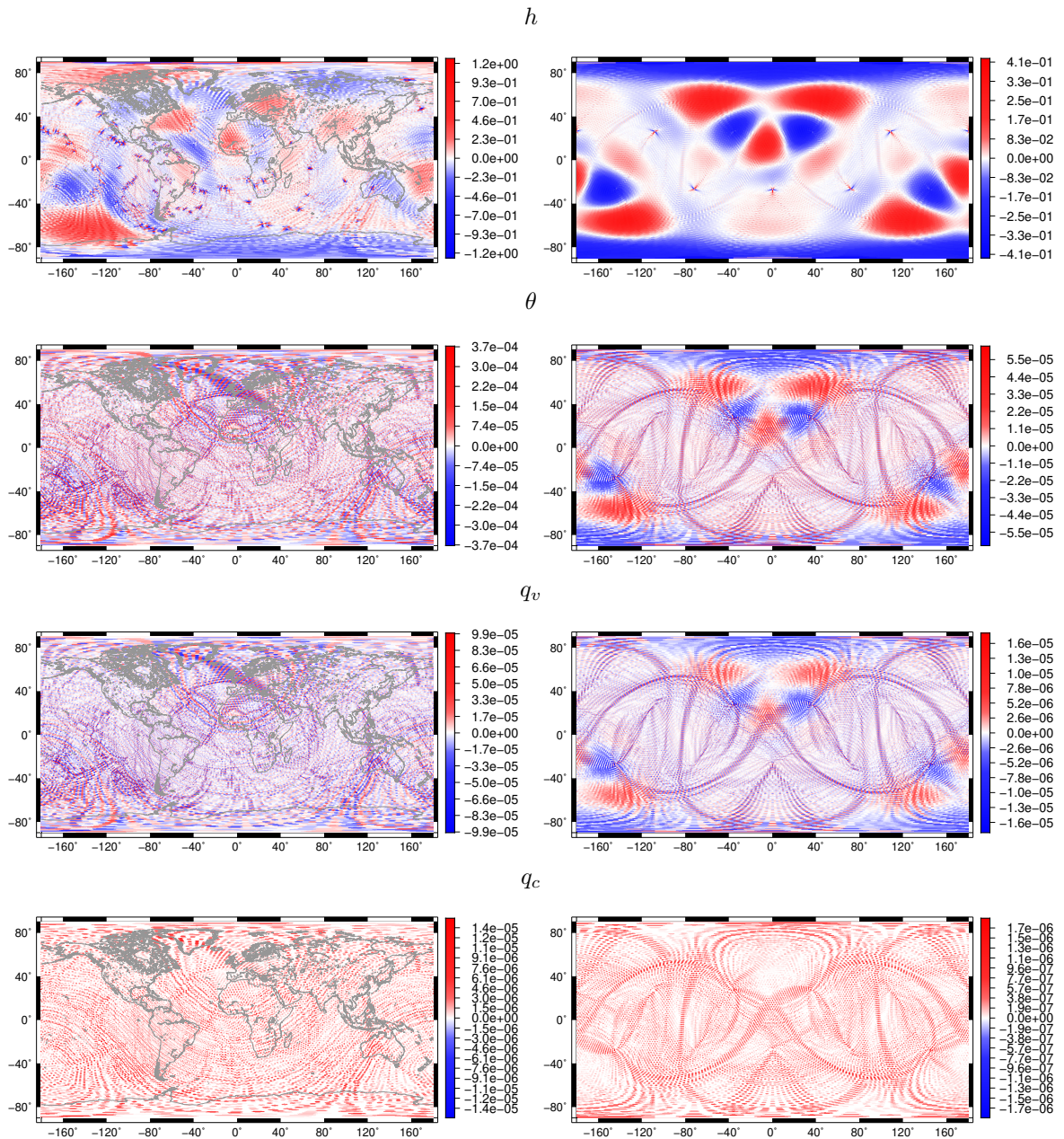
h

θ

q_v

q_c

Figure 5.3: *Field errors after 30 days: height, temperature, vapour and cloud for steady geostrophic flow on refined grid (left) and uniform grid (right).*
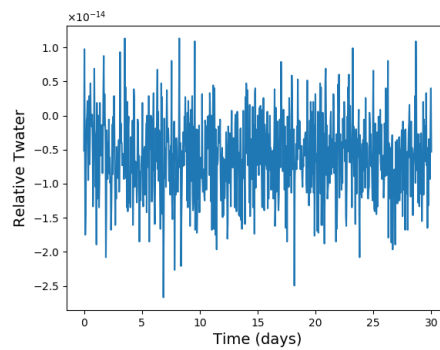

Figure 5.4: *Evolution with time of the relative change in total water for steady geostrophic flow on refined grid.*

5.3.2 Flow over Andes mountain

This test is similar to test 5 from Will92. The bottom topography is again the smooth Andes topography data (Figure 5.5). We normalized the values of Andes topography between 0 and 2000m. The initial fields are given by:

$$u^0(\lambda, \phi) = u_0 \cos \phi, \tag{5.20}$$

$$v^0(\lambda, \phi) = 0, \tag{5.21}$$

$$h^0(\lambda, \phi) = h_0 - b(\lambda, \phi) - \frac{1}{g}\omega \sin^2 \phi, \tag{5.22}$$

$$\theta^0(\lambda, \phi) = F(\theta^{SP}, (1 - \mu_1)\theta^{EQ}, \theta^{NP}, \phi) + \mu_1 \theta^{EQ} \cos \phi \sin \lambda, \tag{5.23}$$

$$q_v^0(\lambda, \phi) = \mu_2 q_{sat}(b, h_0, \theta_0), \tag{5.24}$$

$$q_c^0(\lambda, \phi) = 0, \tag{5.25}$$

$$q_r^0(\lambda, \phi) = 0, \tag{5.26}$$

$$\tag{5.27}$$

where F is the function given by:

$$F(f_1, f_2, f_3, \phi) = \frac{2}{\pi^2}\left[\phi\left(\phi - \frac{\pi}{2}\right)f_1 - 2\phi\left(\phi + \frac{\pi}{2}\right)\left(\phi - \frac{\pi}{2}\right)f_2 + \phi\left(\phi + \frac{\pi}{2}\right)f_3\right]. \tag{5.28}$$

The parameters are set as $u_0 = 20$, $\omega = \left(\Omega a u_0 + \frac{u_0^2}{2}\right)$, $\theta^{SP} = -40\varepsilon$, $\theta^{EQ} = 40\varepsilon$, $\theta^{NP} = -20\varepsilon$, $\varepsilon = \frac{1}{300}$, $\mu_1 = 0.05$, $\mu_2 = 0.98$ and $h_0 = 5960$.
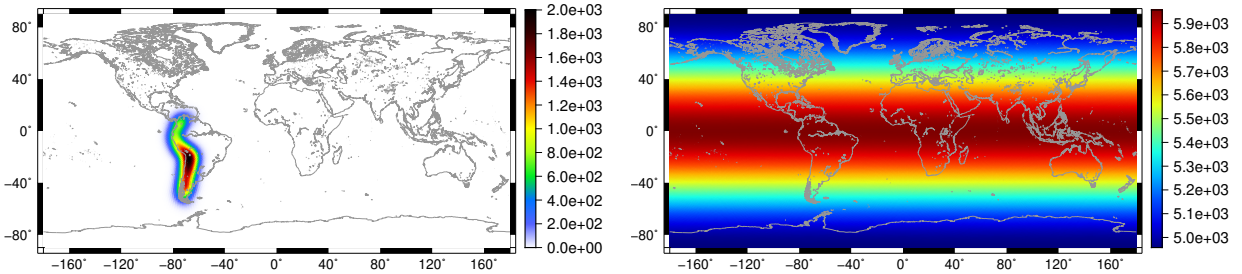

Figure 5.5: *Andes smooth topography (left) and initial total fluid depth (right) for flow over Andes test case.*

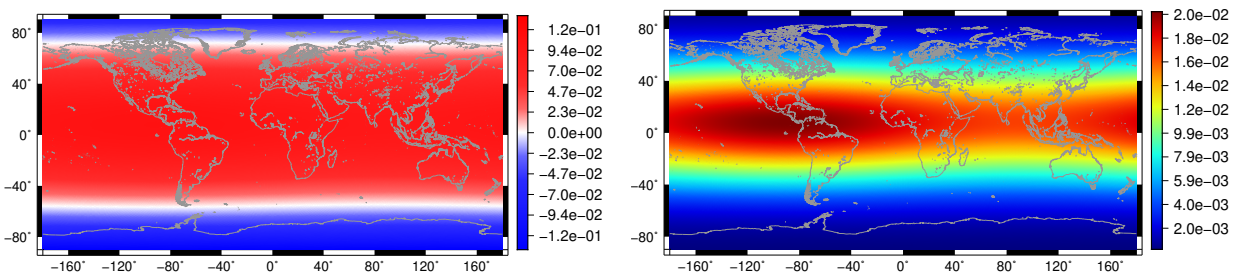**Figure 5.6:** *Initial temperature (left) and initial vapour depth (right) for flow over Andes test case.*

In Figures 5.5 and 5.6 we show the initial fields. The vapour field has a concentration near to central America. As in the previous test, we ran this model for 30 days on the grid with $3\times$ higher resolution on Andes and on the uniform SCVT grid. The grid level is equal to 6 in both cases.
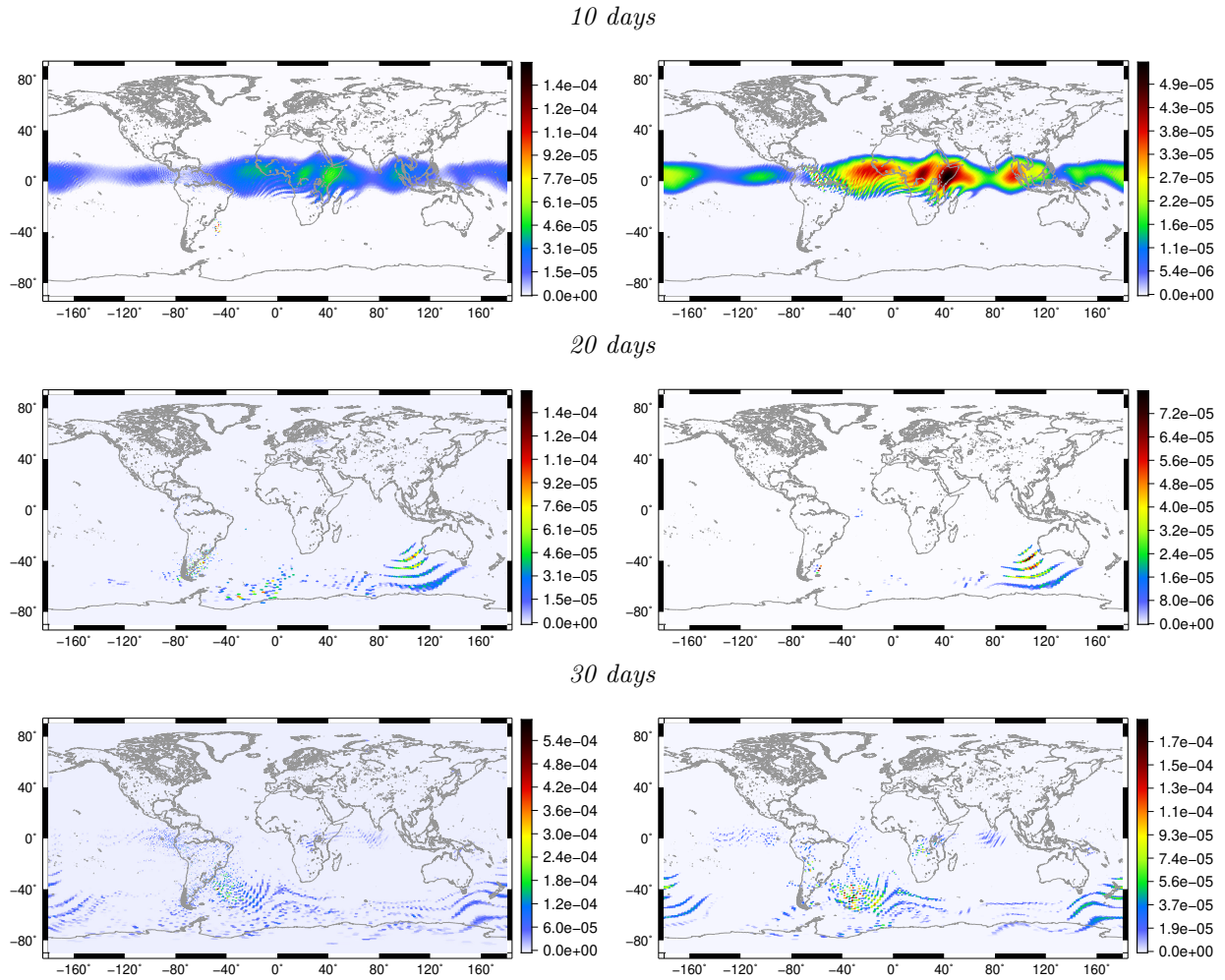
Figure 5.7: *Flow over Andes mountain test case: Cloud at days 10 (top), 20 (middle) and 30 (bottom) on refined (left) and uniform grid (right).*

In Figure 5.7 we show the cloud field at days 10, 20 and 30 in both grids. We can notice that they are similar but the absolute value is slightly different. Furthermore, there are more clouds being captured in the refined region when compared to the uniform grid. Nevertheless, the rain generated is very different in both grids. In the uniform grid, no rain is generated until day 20. In the refined grid, the rain starts at day 10. The uniform grid seems to represent better the rain than the refined grid, since the simulation on test 2 presented in Zerroukat e Allen (2015) produces rain only after 15 days. In the cloud field, we can observe negative values in both grids. This is clearly undesirable, but for the cloud field, the negative values are in magnitude much smaller than the positive values. On other hand, the rain field shows negative values that have the same magnitude of the positive values, as we can see in Figures 5.8 and 5.9. This may happen since the advection scheme employed is not a high order and monotonic method. This leads to an inaccurate representation of the rain. Even though there are negative values in rain and cloud, the total water was preserved similarly to the previous simulation (not shown).
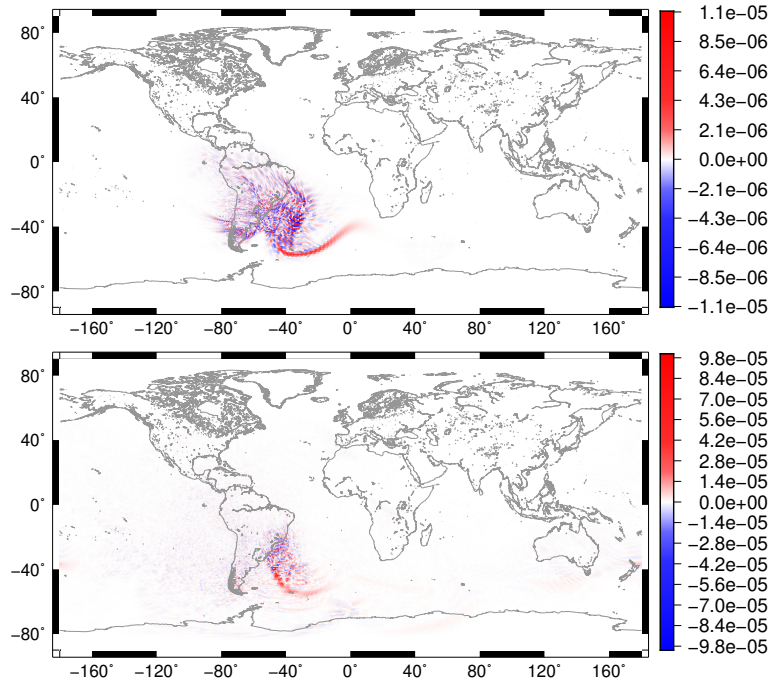
Figure 5.8: *Flow over Andes: Rain at day 15 (top) and day 30 (bottom) on the refined grid. We considered a grid with 40962 generators.*
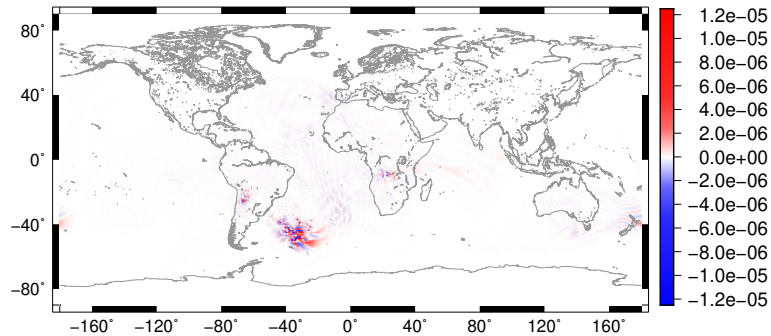

Figure 5.9: *Flow over Andes: Rain at day 30 (right) on the uniform grid. We considered a grid with 40962 generators.*

To avoid negative values in the moisture variables, we introduce a mass fixer in our model. Whenever a variable q^k is negative at some grid point, the negative value is set equal to zero. All the mass that would be lost is distributed uniformly over the cells. This procedure guarantees only nonnegative values for the moisture variables. However, the total water is no longer conserved.

In Figures 5.10 and 5.11 we show the results obtained using the mass fixer described in the previous paragraph. From Figure 5.10 we can notice at day 10 that clouds are generated in the South of Brazil on the refined grid but not on the uniform grid. Furthermore, rain is visible near to the South of Brazil only on the refined grid and no rain is formed in the uniform grid. At day 20 we can observe that clouds are formed near to the South of Brazil on the uniform grid and at day 30 rain is produced in that region. However, at day 30 in the refined grid there is much more rain and cloud next to the South of Brazil. This is evidence that these effects are caused by local grid refinement. Nevertheless, most of the rain and cloud generated are concentrated in the transition zone between higher and lower resolution grid. No rain or clouds were observed in the Andes, where we have the highest resolution. As we mentioned, the total of water is no longer conserved when we employ the mass fixer (Figure 5.12).

Figure 5.10: *Flow over Andes: cloud at days 10 (top), 20 (middle) and 30 (bottom) on refined grid (left) and uniform grid (right). Mass fixer was employed. We considered a grid with 40962 generators.*
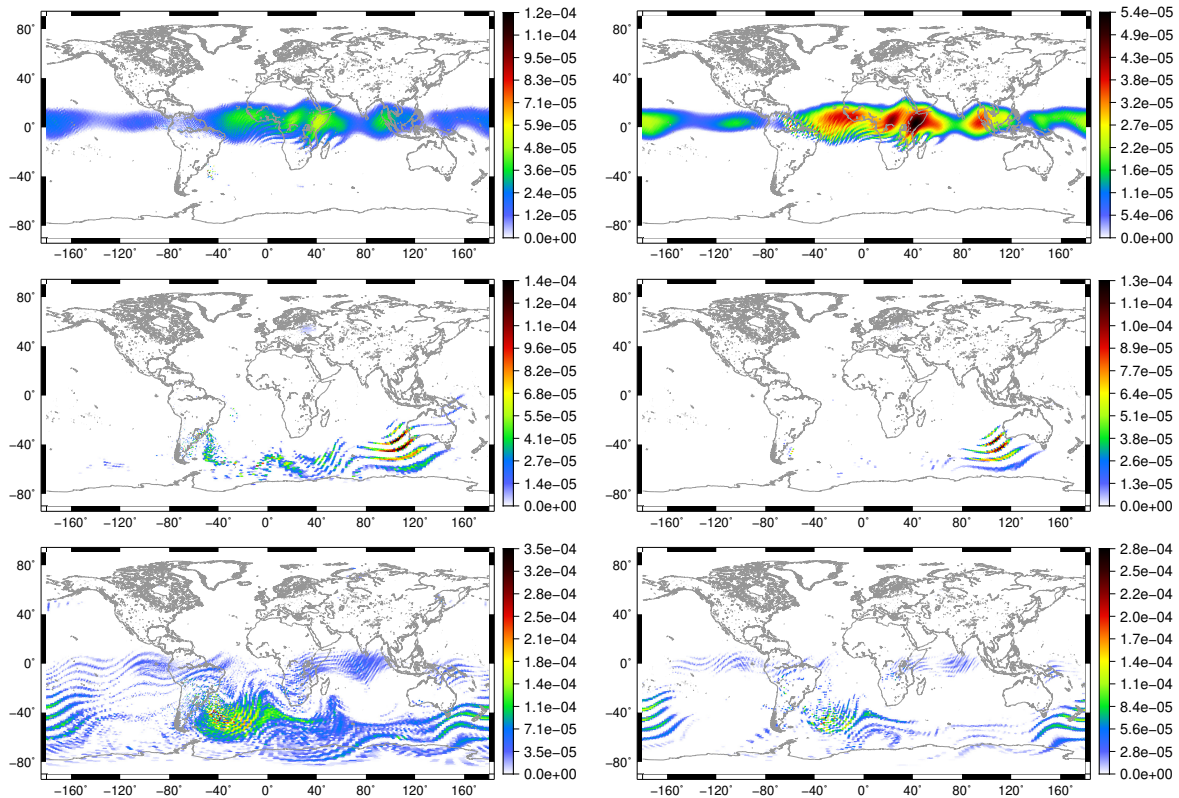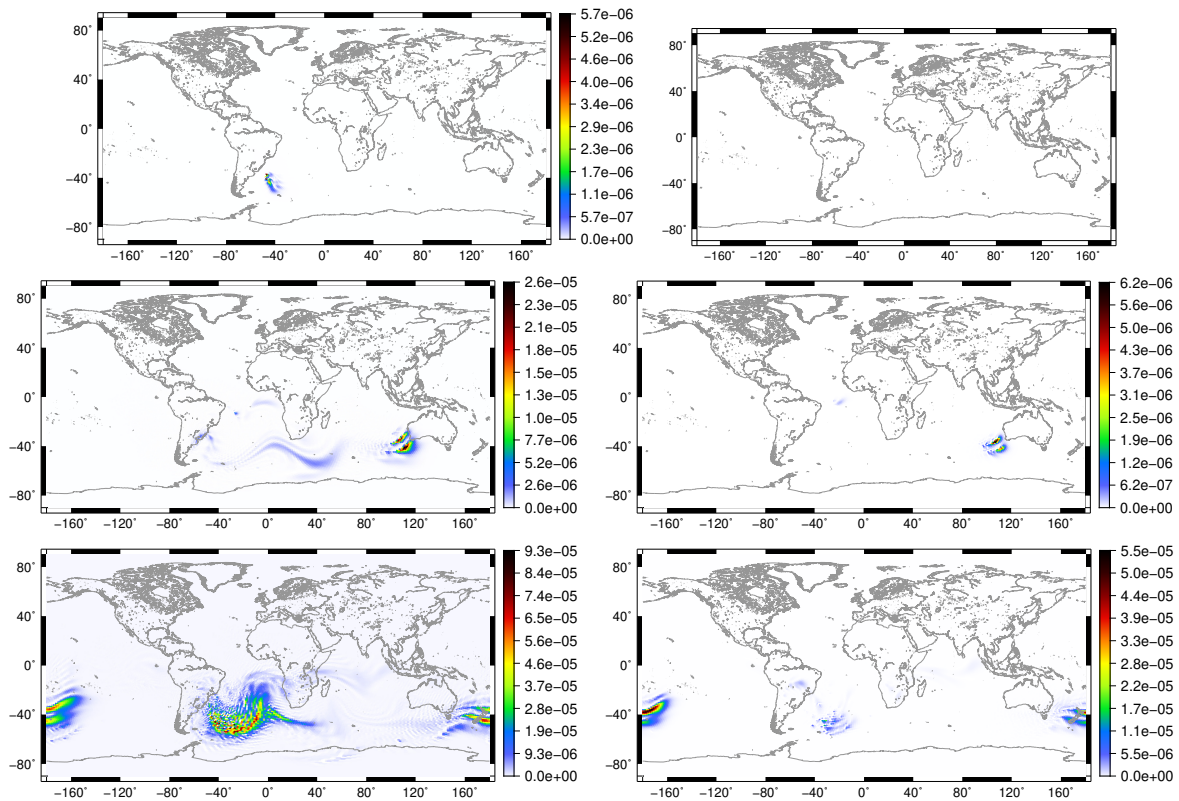

Figure 5.11: *Flow over Andes: rain at days 10 (top), 20 (middle) and 30 (bottom) on refined grid (left) and uniform grid (right). Mass fixer was employed. We considered a grid with 40962 generators.*
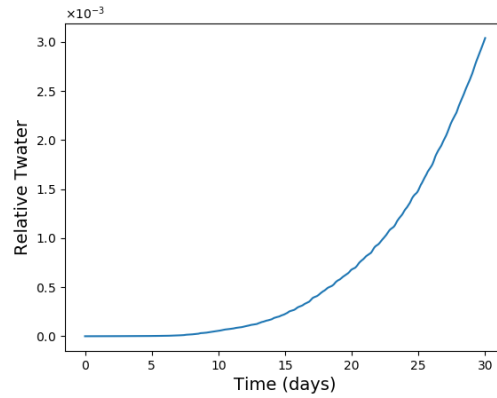
Figure 5.12: *Flow over Andes: Time evolution of the relative variation of the total water. Mass fixer was employed.*

We ran this test on the refined grid employing the mass fixer with diffusion the momentum equation. The results are shown in Figure 5.13. The results show that diffusion reduced the magnitude of the rain and clouds. Also, fewer clouds and rain are formed near to the South of Brazil. However, there is a significant quantity of rain and clouds in this region.

Figure 5.13: *Flow over Andes: cloud (left) and rain (right) at days 10 (top), 20 (middle) and 30 (bottom) on refined grid. ass fixer was employed. We considered a grid with 40962 generators.*
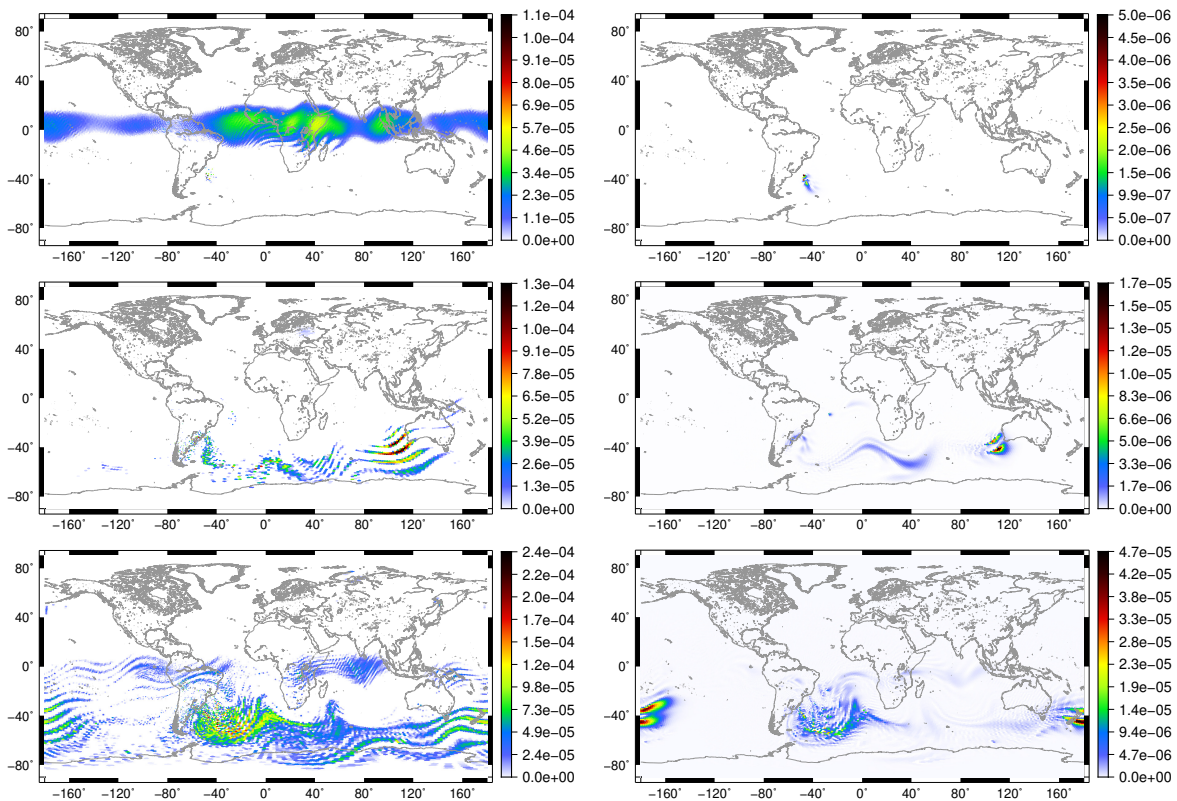
Chapter 6

Concluding remarks

In this work, we investigated the method TRSK developed by Thuburn *et al.* (2009) and Ringler *et al.* (2010) in SCVT grids with local refinement on the Andes mountain built through Lloyd's method. We showed how these grids can be built using smooth topography data.

We analysed TRSK on the refined grids in two different frameworks. In the first framework, we worked in the classical shallow water model and tested the standard tests proposed in the literature. In general, we could observe that error in the velocity field triggers numerical noise. These noises were also observed in the potential vorticity. The only exception was the Matsuno baroclinic wave proposed by Shamir *et al.* (2019), where the velocity showed to be stable even after a long period of integration. Some numerical noise was detectable in the Hovmoller diagram for the vorticity though.

The error in velocity triggered numerical noises in the height field for tests 2 and 6 of Williamson *et al.* (1992). After including diffusion in those tests, we could observe that numerical noises in the velocity were removed. The unstable barotropic jet test case showed to have less numerical noise when the diffusion is applied even when we compare it with the results on the uniform SCVT grid (Peixoto, 2016). Test case 2 seems to converge in the velocity field in both norms l_∞ and l_2 when the grid level increases after applying diffusion. The height error decreases only in the l_2 norm as with the uniform grid case. An issue with diffusion is that the total energy is no longer conserved.

We could notice that the error of height field was in general concentrated in ill aligned cells, with reason explained in Peixoto e Barros (2013). In our simulations, we couldn't notice a relation between error pattern and distortion.

The second framework investigated in this work is the moist shallow water model, which is derived using the traditional Boussinesq approximation. This model includes thermodynamic equations for the moisture and temperature variable. We showed how the equations of this model can be discretized in a C staggered grid using the operators of TRSK.

The first test analysed in the moist shallow water model is a steady-state in both refined and uniform SCVT grids. In this test, we could observe a similar behavior to test case 2 in the classical shallow water model. The error in velocity increases with time, but it does not trigger numerical noise in the height field. The second test analysed is a test that simulates a flow over the Andes including the thermodynamics profiles. In the cloud field, we could observe that they generate similar patterns with more cloud being captured in South America. However, for the rain field, we could observe that the rain field had negative values. Therefore, a monotonic filter was employed, together with a mass fixer. We ran this test again with the fixers and we could observe that rain next to the South of Brazil was generated faster on the refined grid than in the uniform grid. Also, more clouds and rain were visible at day 30 on the refined grid near to the higher resolution region. After adding diffusion, we could notice that the rain e and clouds reduce in magnitude, but they still being noticed in regions where they are not visible on the uniform grid.

An extension of this work could be an analysis of the effect of local refinement in the full 3D equations using the MPAS core. The grids developed in this work are directly applicable to MPAS structure. In the convective shallow water model, an extension could be employ a high order and monotonic method in the advection equation for the moisture variables. In general, global

atmospheric models use high order and monotonic methods for the advection of tracers. That could lead to a more accurate representation of the moisture variables.

Bibliography

Amante e Eakins(2009) Christopher Amante and B. Eakins. Etopo1 1 arc-minute global relief model: procedures, data sources and analysis. doi: 10.7289/V5C8276M. Cited in page. 10

Barros e Garcia(2004) Saulo Barros and Claudia Garcia. A global semi-implicit semi-lagrangian shallow-water model on locally refined grids. *Monthly Weather Review - MON WEATHER REV*, 132:53–65. doi: 10.1175/1520-0493(2004)132<0053:AGSSSM>2.0.CO;2. Cited in page. 2

Cote(1988) J. Cote. A Lagrange multiplier approach for the metric terms of semi - lagrangian models on the sphere. *Quarterly Journal of the Royal Meteorological Society*, 114:1347 – 1352. doi: 10.1002/qj.49711448310. Cited in page. 16

Du *et al.*(1999) Qiang Du, Vance Faber and Max Gunzburger. Centroidal Voronoi Tessellations: Applications and algorithms. *Siam Review - SIAM REV*, 41:637–676. doi: 10.1137/S0036144599352836. Cited in page. 2

Du *et al.*(2003) Qiang Du, Max Gunzburger and Lili Ju. Constrained centroidal voronoi tessellations for surfaces. *SIAM Journal on Scientific Computing*, 24:1488–1506. doi: 10.1137/S1064827501391576. Cited in page. 7, 8

Dubos *et al.*(2015) Thomas Dubos, Sarvesh Dubey, Marine Tort, Rashmi Mittal, Y. Meurdesoif and F. Hourdin. DYNAMICO-1.0, an icosahedral hydrostatic dynamical core designed for consistency and versatility. *Geoscientific Model Development*, 8. doi: 10.5194/gmd-8-3131-2015. Cited in page. 2, 18

Durran(2011) Dale Durran. *Time Discretization: Some Basic Approaches*, páginas 75–104. doi: 10.1007/978-3-642-11640-7_5. Cited in page. 24

Engwirda(2018) Darren Engwirda. Generalised primal-dual grids for unstructured co-volume schemes. *Journal of Computational Physics*, 375:155–176. Cited in page. 8

Ferguson *et al.*(2019) Jared Ferguson, Christiane Jablonowski and Hans Johansen. Assessing adaptive mesh refinement (amr) in a forced shallow-water model with moisture. *Monthly Weather Review*, 147. doi: 10.1175/MWR-D-18-0392.1. Cited in page. 47

Galewsky *et al.*(2004) J. Galewsky, Richard Scott and Lorenzo Polvani. An initial-value problem for testing numerical models of the global shallow-water equations. *Tellus A*. doi: 10.3402/tellusa.v56i5.14436. Cited in page. 3, 27, 44

Gassmann(2013) Almut Gassmann. A global hexagonal C-grid non-hydrostatic dynamical core (ICON-IAP) designed for energetic consistency. *Quarterly Journal of the Royal Meteorological Society*, 139:152–175. doi: 10.1002/qj.1960. Cited in page. 2

Haltiner e Williams(1980) George J Haltiner and Roger T Williams. *Numerical Prediction and Dynamic Meteorology*. Wiley, Second edition. Cited in page. 1, 15

Heikes e Randall(1995) Ross Heikes and David Randall. Numerical integration of the shallow-water equations on a twisted icosahedral grid. part i: Basic design and results of tests.

Monthly Weather Review - MON WEATHER REV, 123. doi: 10.1175/1520-0493(1995)123<1862: NIOTSW>2.0.CO;2. Cited in page. 2

Holton(2004) James R Holton. *An Introduction to Dynamic Meteorology*. Elsevier, Fourth edition. Cited in page. 1, 15

Jablonowski e Williamson(2011) Christiane Jablonowski and David Williamson. *The Pros and Cons of Diffusion, Filters and Fixers in Atmospheric General Circulation Models*, volume 80, páginas 381–493. doi: 10.1007/978-3-642-11640-7_13. Cited in page. 24, 33

Ju *et al.***(2011)** Lili Ju, Todd Ringler and Max Gunzburger. *Voronoi Tessellations and Their Application to Climate and Global Modeling*, volume 80, páginas 313–342. doi: 10.1007/978-3-642-11640-7_10. Cited in page. 2, 3, 5, 7, 8

Lahaye e Zeitlin(2016) Noe Lahaye and Vladimir Zeitlin. Understanding instabilities of tropical cyclones and their evolution with moist-convective rotating shallow water model. *Journal of the Atmospheric Sciences*, 73:151023111508007. doi: 10.1175/JAS-D-15-0115.1. Cited in page. 47

Liu e Yang(2017) Yudi Liu and Taojin Yang. Impact of local grid refinements of spherical centroidal voronoi tessellations for global atmospheric models. *Communications in Computational Physics*, 21:1310–1324. doi: 10.4208/cicp.050815.020916a. Cited in page. 27

Matsuno(1966) Taroh Matsuno. Quasi-geostrophic motions in the equatorial area. *Journal of the Meteorological Society of Japan*, 44:25–42. doi: 10.2151/jmsj1965.44.1_25. Cited in page. 39

Miura e Kimoto(2005) Hiroaki Miura and Masahide Kimoto. A comparison of grid quality of optimized spherical hexagonal pentagonal geodesic grids. *Monthly Weather Review - MON WEATHER REV*, 133. doi: 10.1175/MWR2991.1. Cited in page. 2, 6

Okabe *et al.***(2000)** Atsu Okabe, Barry Boots, Kokichi Sugihara and Sung Chiu. *Spatial Tessellations: Concepts and Applications of Voronoi Diagrams*, volume 43. doi: 10.2307/2687299. Cited in page. 6

Peixoto(2016) Pedro Peixoto. Accuracy analysis of mimetic finite volume operators on geodesic grids and a consistent alternative. *Journal of Computational Physics*, 310. doi: 10.1016/j.jcp.2015.12.058. Cited in page. 21, 27, 31, 32, 34, 59

Peixoto e Barros(2013) Pedro Peixoto and Saulo R. M. Barros. Analysis of grid imprinting on geodesic spherical icosahedral grids. *Journal of Computational Physics*, 237:61–78. doi: 10.1016/j.jcp.2012.11.041. Cited in page. 13, 21, 32, 59

Peixoto(2013) Pedro da S. Peixoto. *Análise de discretizacões e interpolacões em malhas icosaédricas e aplicacões em modelos de transporte semi lagrangianos*. Tese de Doutorado, Instituto de Matemática e Estatística, Universidade de São Paulo, Brasil. Cited in page. 3

Renka(1997) Robert Renka. Algorithm 772: Stripack: Delaunay triangulation and voronoi diagram on the surface of a sphere. *ACM Trans. Math. Softw.*, 23:416–434. doi: 10.1145/275323.275329. Cited in page. 7

Ringler *et al.***(2010)** Todd Ringler, John Thuburn, J. Klemp and W.C. Skamarock. A unified approach to energy conservation and potential vorticity dynamics on arbitrarily structured C-grids. *J. Comput. Physics*, 229:3065–3090. doi: 10.1016/j.jcp.2009.12.007. Cited in page. 2, 3, 15, 17, 18, 20, 25, 34, 59

Ringler *et al.***(2011)** Todd Ringler, Doug Jacobsen, Max Gunzburger, Lili Ju, Michael Duda and William Skamarock. Exploring a multiresolution modeling approach within the shallow-water equations. *Monthly Weather Review*, 139:3348–3368. doi: 10.1175/MWR-D-10-05049.1. Cited in page. 27, 28

Satoh(2004) Masaki Satoh. *Atmospheric Circulation Dynamics and General Circulation Models.* Springer. doi: 10.1007/978-3-642-13574-3. Cited in page. 16

Satoh *et al.*(2008) Masaki Satoh, T. Matsuno, H. Tomita, H. Miura, Tomoe Nasuno and Shin-ichi Iga. Nonhydrostatic Icosahedral Atmospheric Model (NICAM) for global cloud resolving simulations. *Journal of Computational Physics*, 227:3486–3514. doi: 10.1016/j.jcp.2007.02.006. Cited in page. 2

Seluchi *et al.*(1998) Marcelo Seluchi, YV Serafini and H. Treut. The impact of the Andes on transient atmospheric systems: A comparison between observations and gcm results. *Monthly Weather Review*, 126. doi: 10.1175/1520-0493(1998)126<0895:TIOTAO>2.0.CO;2. Cited in page. 3

Shamir *et al.*(2019) Ofer Shamir, Itamar Yacoby, Shlomi Ziv and Nathan Paldor. The matsuno baroclinic wave test case. *Geoscientific Model Development*, 12:2181–2193. doi: 10.5194/gmd-12-2181-2019. Cited in page. 3, 27, 39, 40, 59

Skamarock *et al.*(2012) William Skamarock, J. Klemp, Michael Duda, Laura Fowler, S.-H Park and Todd Ringler. A multiscale nonhydrostatic atmospheric model using centroidal Voronoi tesselations and C-grid staggering. *Monthly Weather Review*, 240:3090–3105. doi: 10.1175/MWR-D-11-00215.1. Cited in page. 2, 18, 24, 28

Staniforth e Thuburn(2012) Andrew Staniforth and John Thuburn. Horizontal grids for global weather and climate prediction models: A review. *Quarterly Journal of the Royal Meteorological Society*, 138:1 – 26. doi: 10.1002/qj.958. Cited in page. 2, 25

Thuburn e Cotter(2012) John Thuburn and C.J. Cotter. A framework for mimetic discretization of the rotating shallow-water equations on arbitrary polygonal grids. *SIAM Journal on Scientific Computing*, 34. doi: 10.1137/110850293. Cited in page. 3, 18

Thuburn e Li(2000) John Thuburn and Yong Li. Numerical simulation of rossby haurwitz waves. *Tellus A*, 52:181 – 189. doi: 10.1034/j.1600-0870.2000.00107.x. Cited in page. 37, 40

Thuburn *et al.*(2009) John Thuburn, Todd Ringler, W. Skamarock and J. Klemp. Numerical representation of geostrophic modes on arbitrarily structured C-grids. *J. Comput. Physics*, 228: 8321–8335. doi: 10.1016/j.jcp.2009.08.006. Cited in page. 2, 3, 15, 18, 22, 23, 25, 59

Thuburn *et al.*(2010) John Thuburn, Mohamed Zerroukat, Nigel Wood and A. Staniforth. Coupling a mass conserving semi lagrangian scheme (slice) to a semi implicit discretization of the shallow water equations: Minimizing the dependence on a reference atmosphere. *Quarterly Journal of the Royal Meteorological Society*, 136:146 – 154. doi: 10.1002/qj.517. Cited in page. 35

Tomita *et al.*(2002) Hirofumi Tomita, Masaki Satoh and Koji Goto. An optimization of the icosahedral grid modified by spring dynamics. *Journal of Computational Physics*, 183:307–331. doi: 10.1006/jcph.2002.7193. Cited in page. 2

Walsh(1994) Kelvin Walsh. On the influence of the Andes on the general circulation of the Southern Hemisphere. *Journal of climate*, 7(6):1019–1025. Cited in page. 3

Wan *et al.*(2013) Hui Wan, Marco Giorgetta, G. Zangl, M. Restelli, D. Majewski, Luca Bonaventura, Kristina Frohlich, D. Reinert, Maria Ripodas and L. Kornblueh. The icon-1.2 hydrostatic atmospheric dynamical core on triangular grids - part 1: Formulation and performance of the baseline version. *Geoscientific Model Development Discussions*, 6:59–119. doi: 10.5194/gmdd-6-59-2013. Cited in page. 24

Weller(2014) H. Weller. Non-orthogonal version of the arbitrary polygonal c-grid and a new diamond grid. *Geoscientific Model Development*, 7(3):779–797. doi: 10.5194/gmd-7-779-2014. URL https://www.geosci-model-dev.net/7/779/2014/. Cited in page. 3, 18

Williamson(2007) David Williamson. The evolution of dynamical cores for global atmospheric models. *J. Royal Met. Soc. Japan*, 85B:241–269. doi: 10.2151/jmsj.85B.241. Cited in page. 1

Williamson *et al.***(1992)** David Williamson, John Drake, James Hack, R Jakob and Paul Swarztrauber. A standard test set for numerical approximations to the shallow water equations in spherical geometry. *Journal of Computational Physics*, 102:211–224. Cited in page. 3, 15, 16, 27, 59

Wuersch e Craig(2014) Michael Wuersch and George Craig. A simple dynamical model of cumulus convection for data assimilation research. *Meteorologische Zeitschrift*, 23:483–490. doi: 10.1127/0941-2948/2014/0492. Cited in page. 47

Zerroukat e Allen(2015) Mohamed Zerroukat and T. Allen. A moist Boussinesq shallow water equations set for testing atmospheric models. *Journal of Computational Physics*, 290. doi: 10.1016/j.jcp.2015.02.011. Cited in page. 3, 47, 48, 49, 54